Lawrence Berkeley National Laboratory
Recent Work

Title

Surface structure determinations of crystalline ionic thin films grown on transition metal single crystal surfaces by low energy electron diffraction

Permalink

https://escholarship.org/uc/item/9d30h43d

Author

Roberts, Joel G.

Publication Date

2000-05-01

eScholarship.org Powered by the California Digital Library
University of California

LBNL-46000

ERNEST ORLANDO LAWRENCE
BERKELEY NATIONAL LABORATORY

Surface Structure Determinations of Crystalline Ionic Thin Films Grown on Transition Metal Single Crystal Surfaces by Low Energy Electron Diffraction

Joel G. Roberts

Materials Sciences Division

May 2000

Ph.D. Thesis

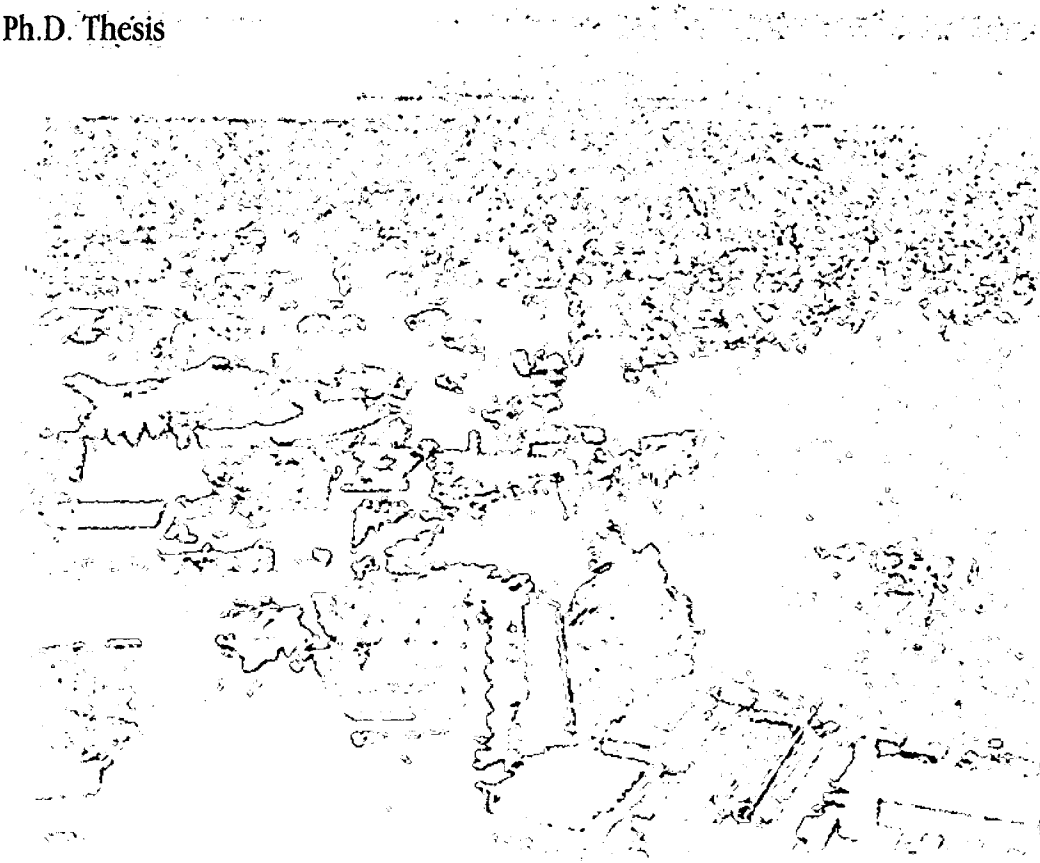

| REFERENCE COPY |
| Does Not |
| Circulate |

Bldg. 50 Library - Ref.
Lawrence Berkeley National Laboratory

Copy 1

LBNL-46000

DISCLAIMER

This document was prepared as an account of work sponsored by the United States Government. While this document is believed to contain correct information, neither the United States Government nor any agency thereof, nor The Regents of the University of California, nor any of their employees, makes any warranty, express or implied, or assumes any legal responsibility for the accuracy, completeness, or usefulness of any information, apparatus, product, or process disclosed, or represents that its use would not infringe privately owned rights. Reference herein to any specific commercial product, process, or service by its trade name, trademark, manufacturer, or otherwise, does not necessarily constitute or imply its endorsement, recommendation, or favoring by the United States Government or any agency thereof, or The Regents of the University of California. The views and opinions of authors expressed herein do not necessarily state or reflect those of the United States Government or any agency thereof, or The Regents of the University of California.

Ernest Orlando Lawrence Berkeley National Laboratory
is an equal opportunity employer.

DISCLAIMER

This document was prepared as an account of work sponsored by the United States Government. While this document is believed to contain correct information, neither the United States Government nor any agency thereof, nor the Regents of the University of California, nor any of their employees, makes any warranty, express or implied, or assumes any legal responsibility for the accuracy, completeness, or usefulness of any information, apparatus, product, or process disclosed, or represents that its use would not infringe privately owned rights. Reference herein to any specific commercial product, process, or service by its trade name, trademark, manufacturer, or otherwise, does not necessarily constitute or imply its endorsement, recommendation, or favoring by the United States Government or any agency thereof, or the Regents of the University of California. The views and opinions of authors expressed herein do not necessarily state or reflect those of the United States Government or any agency thereof or the Regents of the University of California.

LBNL-46000

Surface Structure Determinations of Crystalline Ionic Thin Films Grown on Transition Metal Single Crystal Surfaces by Low Energy Electron Diffraction

Joel Glenn Roberts
Ph.D. Thesis

Department of Chemistry
University of California, Berkeley

and

Materials Sciences Division
Ernest Orlando Lawrence Berkeley National Laboratory
University of California
Berkeley, California 94720

May 2000

This work was supported by the Director, Office of Science, Office of Basic Energy Sciences, Materials Sciences Division, of the U.S. Department of Energy under Contract No. DE-AC03-76SF00098.

Surface Structure Determinations of Crystalline Ionic Thin Films Grown on Transition Metal Single Crystal Surfaces by Low Energy Electron Diffraction

by

Joel Glenn Roberts

B.S. (University of Nebraska, Lincoln) 1995

A dissertation submitted in partial satisfaction of the
requirements for the degree of

Doctor of Philosophy

in

Chemistry

in the

GRADUATE DIVISION

of the

UNIVERSITY OF CALIFORNIA, BERKELEY

Committee in charge:

Professor Gabor A. Somorjai, Chair
Professor Norman E. Phillips
Professor Roya Maboudian

Spring 2000

Surface Structure Determinations of Crystalline Ionic Thin Films Grown on Transition Metal Single Crystal Surfaces by Low Energy Electron Diffraction

Copyright © 2000

by

Joel Glenn Roberts

The U.S. Department of Energy has the right to use this document for any purpose whatsoever including the right to reproduce all or any part thereof

Abstract

Surface Structure Determinations of Crystalline Ionic Thin Films Grown on Transition Metal Single Crystal Surfaces by Low Energy Electron Diffraction

by

Joel Glenn Roberts

Doctor of Philosophy in Chemistry

University of California, Berkeley

Professor Gabor A. Somorjai, Chair

The surface structures of NaCl(100), LiF(100) and α-$MgCl_2$(0001) adsorbed on various metal single crystals have been determined by low energy electron diffraction (LEED). Thin films of these salts were grown on metal substrates by exposing the heated metal surface to a molecular flux of salt emitted from a Knudsen cell. This method of investigating thin films of insulators (ionic salts) on a conducting substrate (metal) circumvents surface charging problems that plagued bulk studies, thereby allowing the use of electron-based techniques to characterize the surface.

The surface layer of NaCl(100) was found to have a 0.12±0.03 Å corrugation due to movement of the Na^+ ions towards the bulk. Additional deviations from the bulk structure were not seen in the deeper atomic layers. In order to determine if the metal substrate had an influence on the films' growth characteristics, multilayer films of NaCl(100) were grown on Pd(100) and Pt(111). An tensor LEED (TLEED) analysis of the diffraction beam intensities from the NaCl(100)-(1x1) on Pd(100) and NaCl(100)-(1x1) on Pt(111) LEED patterns showed that the multilayer NaCl(100) film had the same structure on both substrates to a depth sampled by the electrons in the individual experimental energy ranges. Additionally, these two films exhibited the same adsorbate-substrate interaction on Pd(100) and Pt(111) as evidenced by the lone multilayer (zero order) desorption peak observed in the temperature programmed desorption (TPD) spectra of NaCl.

The surface structure of LiF(100) was studied to correlate the surface corrugation of the alkali halide (100) surface to the ions' polarizability. The LiF surface is less polarizable than the NaCl surface. TLEED calculations determined that the LiF(100) surface had a 0.24±0.04 Å corrugation with a 0.06±0.04 Å corrugation of the second layer. Both corrugations were due to the cations moving deeper into the bulk.

Unlike NaCl and LiF, $MgCl_2$ adsorbed on Pd(111) and Pt(111) exhibited a first order desorption feature in its TPD spectra, indicating a significant adsorbate-substrate interaction. This interaction led to the formation of two distinct

monolayer LEED patterns: Pd/Pt(111)- (4×4)-$MgCl_2$ and Pd/Pt(111)- $\left(\sqrt{13}\times\sqrt{13}\right)$ R 13.9° -$MgCl_2$ (where a monolayer is defined as one Cl-Mg-Cl molecular layer). In addition to the monolayer patterns, an ordered multilayer was grown on Pd/Pt(111). For the adsorbed $MgCl_2$ multilayer on Pd(111), a fully dynamical TLEED analysis was performed. The surface structure of α-$MgCl_2$(0001) is very similar to its bulk structure with the exception of a 0.10±0.06 Å contraction of the first Cl-Cl interlayer spacing.

TPD spectra showed that the strong adsorbate-substrate interaction between $MgCl_2$ and Pd/Pt(111) disappeared when the substrate was changed to Pt(100), Pd(100) and Rh(111). Although ordered $MgCl_2$(0001) multilayers were formed on all three of these metal crystals, no monolayer patterns were formed which indicated a strong adsorbate-substrate interaction. The absence of monolayer patterns is consistent with the TPD results.

Table of Contents

List of Figures

List of Tables

Acknowledgements

Ever since I read my first thesis, I have looked forward to the day when I would be writing my acknowledgements. Writing this section not only signifies the completion of my term in Berkeley, but it gives me the opportunity to thank everyone who made my time here educational, enjoyable and profound. First and foremost, I would like to thank my advisor Professor Gabor A. Somorjai for his guidance and motivation. Gabor's intense curiosity fuels one of the most intellectually diverse groups in Berkeley. I would also like to thank Dr. Michel Van Hove for his unwavering support of my work and his careful editing of my manuscripts.

The nuts and bolts of UHV was taught to me by D. Howard Fairbrother. His expertise was essential in my early development. On the LEED theory side, Martin Gierer aided me in performing the structural studies and in understanding the science behind the FORTRAN. Saskia Hoffer needs to be thanked for struggling with me for a year and a half and for being a great friend. I am proud to have published with her. H. Alex Yoon, John Jensen and Craig Tewell were instrumental in making me feel welcomed during my first year and in acclimating me to the group and to graduate school. The knowledge gained through discussions with Enrico Magni, Paul Cremer and Michael Yang will always be valued.

The conversations about life, the universe and everything would not have been as fruitful without Kyle Kung, Peilin Chen, Keith Rider and Yong Chen.

Aric Opdahl's critical reading of my abstract was much appreciated. Thanks to Andre Ramos and Edmar Soares for introducing me to a Brazilian barbeque.

Cheryl Hawkins, Robin Fulton and Chris Caylor belong to my small cadre of trusted friends. They provided much needed support throughout graduate school, and I will always be indebted to them for that. Weekly "therapy" sessions with Robin and Cheryl at Strada have provided some very memorable moments. Additional thanks to Robin for being my sniping partner at the symphony.

I need to thank Virginia Loo for being a great roommate, friend and baker. Virginia and Kyle filled the last few years in Berkeley with interesting conversation and, particularly Virginia, cookies. Elizabeth Osterchill, John Peralta, Matt Zimmerman and Kristine Mueller brought a bit of Nebraska out by visiting me.

Finally, I have to thank my family. My parents have always supported my endeavors and filled me with the belief that I could achieve anything. My siblings, Tamela, Ed, Melvin and Rose, have taught me lessons that over twenty years of schooling could never reproduce, for that I am grateful

This work was supported by the Director, Office of Energy Research, Office of Basic Energy Sciences, Materials Science Division of the U.S. Department of Energy under contract number DE-AC03-76SF00098.

Chapter 1

Introduction

Structure represents one of the most fundamental characteristics of a compound, since a detailed structural description often serves as the starting point for theories seeking to explain other physical observations. For surfaces, the structure has an even greater significance, since previous studies have shown that it can greatly differ from the bulk structure [1]. These deviation are important to quantify because in a heterogeneous environment all the chemistry happens at the surface interface. The main technique in elucidating surface structure is low energy electron diffraction (LEED). This method exploits the electron's strong interaction with matter to obtain its surface sensitivity and the electron's wave nature to provide diffraction data [2].

The strength of LEED is its ability to determine atomic positions within ≈0.05 Å due to the strict geometric condition for diffraction. Similar to all diffraction techniques, LEED is insensitive to the disordered defect structure of the material. This limitation is important to note, because the majority of the surface chemistry occurs on defect sites [3]. In order to study defects, one needs a local probe such as scanning tunneling microscopy (STM). Unfortunately, the current state of STM theory fails to provide conclusive structural determinations.

A deeper understanding of the surface can be obtained by combining STM and LEED, because they provide complementary information to each other [4]. STM has no restrictions regarding long range order, but all the structural information is mixed up with the electronic density of states of the material. When working with a surface structure previously determined by LEED, the known geometric information provides a good basis for the deconvolution of the electronic and geometric information in the STM image. Another example of LEED being used in conjunction with another technique is its use with a surface vibrational spectroscopy, such as sum frequency generation (SFG). The advantage of SFG is that it can be used in the high pressure regime. With this ability, it can monitor surface reactions as they occur; an impossibility with LEED. LEED's contribution is again its large database of structures. Vibrational peak positions can be assigned when data are taken from a known LEED structure. The information exchange between these techniques is bi-directional. Since LEED structural determinations depend on a trial and error approach, any orientational information which can be obtained from other techniques is extremely beneficial in synthesizing trial structures and in determining the chemical reasonableness of the final structure.

Currently, LEED theory has reached the point where new innovations are deemed evolutionary, not revolutionary. The largest contribution in maturing the discipline was the theoretical description of the multiple scattering process [1,5]. This task was solved due to the tremendous effort of many theorists in the late

1960's and early 1970's. In the 1980's, the application of perturbation theory automated the creation and evaluation of trial structures, therefore decreasing the time to solve a surface structure [6-9]. Throughout this whole theoretical development process, the advent of faster computers provided the means to perform these complex scattering calculations, thereby allowing the theorists to test their developing methods.

On the experimental side, little has changed since the first commercially available post-acceleration LEED was introduced in the 1960's. Equipment changes on the conventional LEED optics are currently driven by 1. faster data acquisition and 2. lower incident beam current. Each of these motivations are needed to allow investigations of electron beam sensitive surfaces. Both of these criteria can be met with the use of a light intensifying camera to record the LEED pattern displayed on the fluorescent screen [10]. The advantage of this method is that it is easily adaptable to all current LEED units. The best solution in lowering the electron dose to the sample is to replace the fluorescent screen with microchannel plates (position sensitive electron multipliers) [11]. This detection system eliminates the background signal of the video system, as a result increasing the signal-to-noise ratio of the LEED intensity data. Most importantly, this system uses a picoampere primary beam current compared to a microampere current used in a conventional setup.

With the theoretical and experimental aspects of LEED fully developed, we are allowed to apply it to more complex surfaces. A survey of the surface

structural literature shows a lack of investigations on strongly ionic, insulating compounds [12]. This dearth of information is a result of the material's incompatibility with traditional electron based methods and their previous lack of usefulness in technological applications. Experimentally, the method of adsorbing thin insulating films on a conductive substrate overcomes the charging problem [13]. Also, interest in these materials, especially thin insulating films, have increased due to the development of three dimensional electronic circuits [14,15]. In these circuits, an epitaxially grown insulating layer would serve as a large band gap boundary layer between two semiconductor structures allowing more circuits to be built in a smaller space. In addition to this technological importance, the nature of the interaction between ionic compounds and metals and ionic compounds and semiconductors raises fundamental questions [14]. Finally, it has been found that surface reactions involving atmospheric pollutants and NaCl crystallites may impact tropospheric ozone concentrations [16-20].

With these scientific and technological questions in mind, this work hopes to contribute to the knowledge base by providing detailed surface structural descriptions of NaCl(100), LiF(100) and $MgCl_2$(0001) thin films. Since these films are grown on dissimilar substrates, the interaction between the ionic bonded adsorbate and the metallic substrate has also been investigated.

Chapter 2

Low Energy Electron Diffraction (LEED)

2.1 INTRODUCTION

Electron diffraction was discovered by Davisson and Germer in one of the most serendipitous events in science [21]. Davisson and Germer were experimenting with backscattering electrons from a polycrystalline nickel target, when an accident in the lab resulted in an oxidized target. The Ni target was cleaned by heating the nickel in H_2. This heating produced large crystalline domains within the sample; these well-ordered areas scattered the beam differently than was seen previously. This difference was due to the exploitation of the wave nature of the incident electrons whose wavelength was described earlier by de Broglie [22].

$$\lambda = \frac{h}{\sqrt{2 \cdot m_e \cdot E}} \tag{2.1}$$

where λ is the wavelength of the electron wave, h is Planck's constant, m_e is the mass of the electron and E is the electron energy.

Surface sensitivity is maintained for low energy (5-500 eV) electrons from the fact that electrons possessing these energies interact strongly with matter [22]. This strong interaction results in a high inelastic scattering probability. Estimates for the volume sampled with elastically scattered electrons is given by the

attenuation length. Physical processes that lead to inelastic scattering include: 1. plasmon scattering 2. valence electron excitation 3. core electron ionization [24]. The effect of phonon scattering is negligible, since the electron energy analyzer used in LEED is not sensitive enough to distinguish these minute energy losses.

Although electron diffraction has been known since 1927, the technique was not widely used due to limited availability of the equipment. The innovation of the display-type LEED units replacing the Faraday cup detection system along with the increased availability of ultra-high vacuum equipment as a result of the rise of the semiconductor industry in the early 1960's, sparked a tremendous growth of LEED and other surface analytical experiments [2]. Concurrently, the theoretical models of the increasing amount of diffraction data were beginning to go beyond the single scattering theory, since the experimental data necessitated such a change. The 1970's witnessed the formalization of the multiple scattering theory, and the beginning of surface structural determinations [2].

2.2 DIFFRACTION CONDITION

The diffraction pattern observed in LEED results from the kinematic scattering of the incident electrons; multiple scattering only affects the intensity changes with electron energy [2]. Illustrated in Fig. 2.1 is the von Laue description of kinematic scattering [25]. Incident on the two scatterers is an

electron plane wave with a wave vector of $\vec{\mathbf{k}}$. The plane wave description of the incident wave is accurate, since the source can be approximated as a point source , since it is far away from the sample. The scattered radiation observed with wave vectors $\vec{\mathbf{k}}$ and $\vec{\mathbf{k}}'$ will constructively interfere if the following condition is satisfied:

$$\vec{\mathbf{d}} \cdot \left(\vec{\mathbf{k}} - \vec{\mathbf{k}}'\right) = 2\pi n \tag{2.2}$$

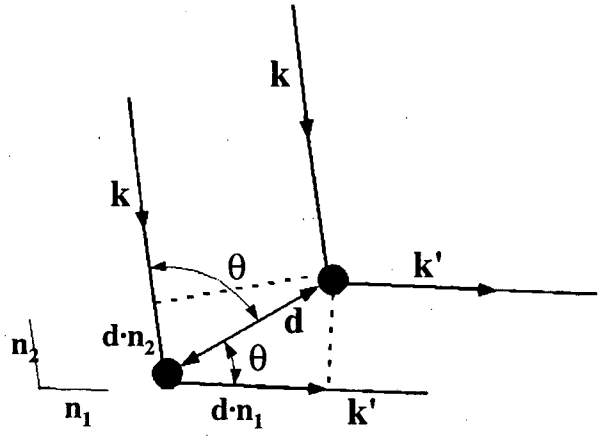

Fig. 2.1. Von Laue diffraction condition.

where $\vec{\mathbf{d}}$ is the position vector between the two scatterers, $\vec{\mathbf{k}}$ is the incident wave vector and $\vec{\mathbf{k}}'$ is the scattered wave vector. Plane waves are used again to model the scattered radiation. Although the point scatterers would produce spherical waves, the plane wave usage is valid when the observation is performed far away

from the point source even for a single scatterer. In a periodic solid, $\vec{\mathbf{d}}$ can be replace by $\vec{\mathbf{R}}$, the basis vectors for lattice.

$$\vec{\mathbf{R}} \cdot \left(\vec{\mathbf{k}} - \vec{\mathbf{k}}'\right) = 2\pi n \text{ which is equivalent to } \mathrm{Exp}\left[i\left(\vec{\mathbf{k}} - \vec{\mathbf{k}}'\right) \cdot \vec{\mathbf{R}}\right] = 1 \qquad (2.3)$$

Comparing equation 1.3 to the reciprocal lattice definition:

$$\mathrm{Exp}\left(i\vec{\mathbf{K}} \cdot \vec{\mathbf{R}}\right) = 1 \qquad (2.4)$$

It can be easily surmised that the Laue equation (equation 1.3) will be satisfied if the difference between the incident and scattered wave vectors $\left(\vec{\mathbf{k}} - \vec{\mathbf{k}}'\right)$ is equal to a reciprocal lattice vector $\left(\vec{\mathbf{K}}\right)$, resulting in a diffraction event.

When applying this diffraction condition to a periodic array with the scatterers positioned at d_1, d_2, ... d_n within a n-atom basis unit cell, the diffraction amplitude is dependent on the constructive interference magnitude of the radiation from these basis sites. Mathematically, the geometrical structure factor, S_K, quantifies this value.

$$S_K = \sum_{j=1}^{n} \mathrm{Exp}\left(i\vec{\mathbf{K}} \cdot \vec{\mathbf{d}}_j\right) \qquad (2.5)$$

where $\vec{\mathbf{K}} = \left(\vec{\mathbf{k}} - \vec{\mathbf{k}}'\right)$, $\vec{\mathbf{d}}_j$ is the positional vector of the j^{th} basis and n is the number of basis atoms. Intensity of the diffracted beams is proportional to the square of this geometrical structure factor.

It can be surmised from the von Laue formulation of diffraction for noninteracting radiation (e.g. x-rays) that the energy is conserved in all directions. This assumption breaks down for low energy electrons, since their surface

sensitivity results from their strong interaction with matter. This electron-matter interaction still requires the conservation of energy parallel to the surface, but not perpendicular to it. The loss of perpendicular energy conservation of the wave vector imposes less restriction on the diffraction condition, thus kinematically speaking, diffraction events can always be seen. Experimentally, this is not the case, but the reasoning is in the realm of the multiple scattering.

2.3 NOMENCLATURE

Illustrated in Fig. 2.2(a) is a real space representation of a hexagonal surface of a face centered cubic (fcc) material (for this example platinum). The vectors $\vec{\mathbf{a}}_1$ and $\vec{\mathbf{a}}_2$ represent the unit vectors of the clean surface or, for the case of clean surface reconstructions, the unreconstructed surface. These vectors define the smallest unit cell in which translations alone can recreate the clean surface, i.e. its translational symmetry. Fig. 2.2(b) shows the surface after adsorbing an overlayer (oxygen in this case). The vectors $\vec{\mathbf{b}}_1$ and $\vec{\mathbf{b}}_2$ define the overlayer's translational symmetry. Since the overlayer's unit cell is larger than that of the underlying substrate, the substrate also can be unambiguously created by simply copying and translating the unit cell bound by the $\vec{\mathbf{b}}_1$ and $\vec{\mathbf{b}}_2$ vectors. $\vec{\mathbf{b}}_1$ and $\vec{\mathbf{b}}_2$ can always be expressed as a linear combination of $\vec{\mathbf{a}}_1$ and $\vec{\mathbf{a}}_2$.

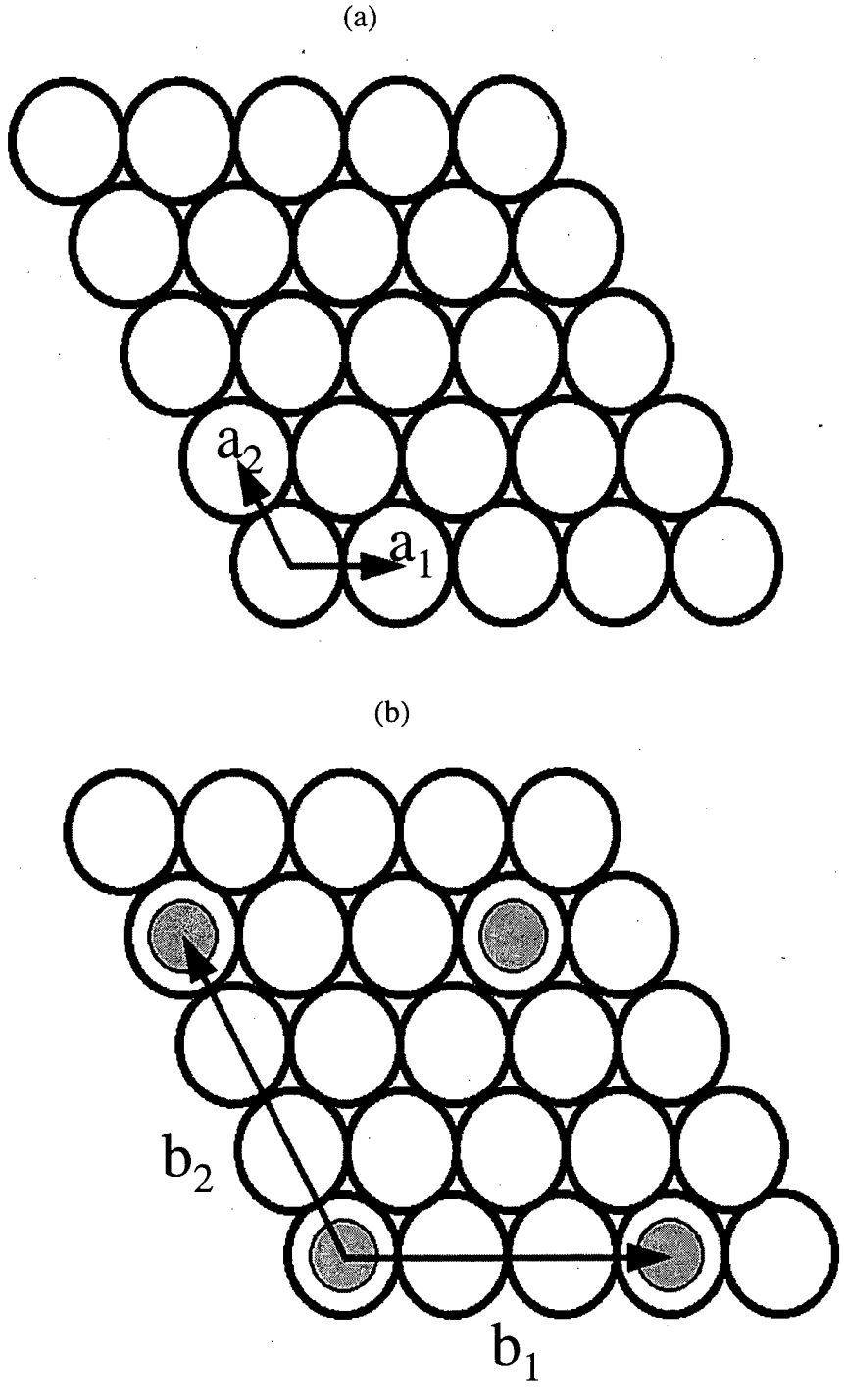

Fig. 2.2. Real space diagram of a (a) hexagonal surface and (b) the same surface with a (3 x 3) overlayer. The unit cell vectors are indicated by **a** and **b** for the substrate and the overlayer,respectively.

$$\vec{b}_1 = J_{11}\vec{a}_1 + J_{12}\vec{a}_2 \tag{2.6a}$$

$$\vec{b}_2 = J_{21}\vec{a}_1 + J_{22}\vec{a}_2 \tag{2.6b}$$

$$\text{equivalent to } \begin{bmatrix}\vec{b}_1 \\ \vec{b}_2\end{bmatrix} = \begin{bmatrix}J_{11} & J_{12} \\ J_{21} & J_{22}\end{bmatrix} \times \begin{bmatrix}\vec{a}_1 \\ \vec{a}_2\end{bmatrix} \tag{2.7}$$

where J_{xx} are coefficients and $\vec{J}$ is the matrix of the coefficients. The matrix $\vec{J}$ is often used to name the observed patterns. For the example in Fig.2.2(b), the name:

$$\text{Pt(111)} - \begin{bmatrix}3 & 0 \\ 0 & 3\end{bmatrix} - \text{O}$$

labels the overlayer structure. An alternate notation which is encountered in the literature is the Wood notation [2]. In this notation, the overlayer unit cell size and orientation are expressed relative to the substrate's unit cell. Generally, the Wood notation has the following form.

$$\text{Substrate(111)} - \text{w}\left(\frac{|\vec{b}_1|}{|\vec{a}_1|} \times \frac{|\vec{b}_2|}{|\vec{a}_2|}\right) \text{R}\,\alpha - \#\,\text{Adsorbate}$$

where w is p if the unit cell is a primitive cell and c if the unit cell described is a centered unit cell. R α is the angle of rotation in degrees between the overlayer unit cell and the substrate's unit cell. The number (#) preceding the chemical symbol is the number of adsorbate molecules in the unit cell. The omission of w indicates that the unit cell is a primitive one, and the omission of R α says that α is zero degrees. In the example used in Fig 2.2(b), the Wood notation would be Pt(111)-(3×3)-O. In this work a modification of the Wood notation was needed.

The overlayers grown were so thick that the underlying substrate did not contribute to the diffraction intensity, so the pattern was essentially a (1×1), but this Wood notation does not refer to the substrate, but to the multilayer adsorbate film. For example, NaCl(100) – (1×1) on Pt(111) indicates that the pattern seen is the square (1×1) pattern associated to the (100) face of bulk NaCl and not to the hexagonal (1×1) face of Pt(111), since no Pt intensity contributes to the LEED pattern.

2.4 QUALITATIVE ANALYSIS

Multiple scattering and the existence of rotational domains complicate the determination of coverages via LEED pattern analysis. Both of these effects produce a larger number of diffraction beams than is expected if the electrons were scattered by a kinematic process. Multiple scattering leads to the problem of being unable to distinguish true overlayer structures from coincidence lattices [24]. This is illustrated in figure 2.3(b) where an overlayer whose unit cell is four times larger than the substrate's produces the same LEED pattern (Fig. 2.3(a)) as an overlayer with a 4 to 3 coincidence lattice (Fig. 2.3(c))to the substrate. Extra spots are visible, since the effective unit cell is a linear combination of the surface and substrate unit cell, not just the surface unit cell alone due to multiple scattering events. For example, an incident electron can scatter off the overlayer

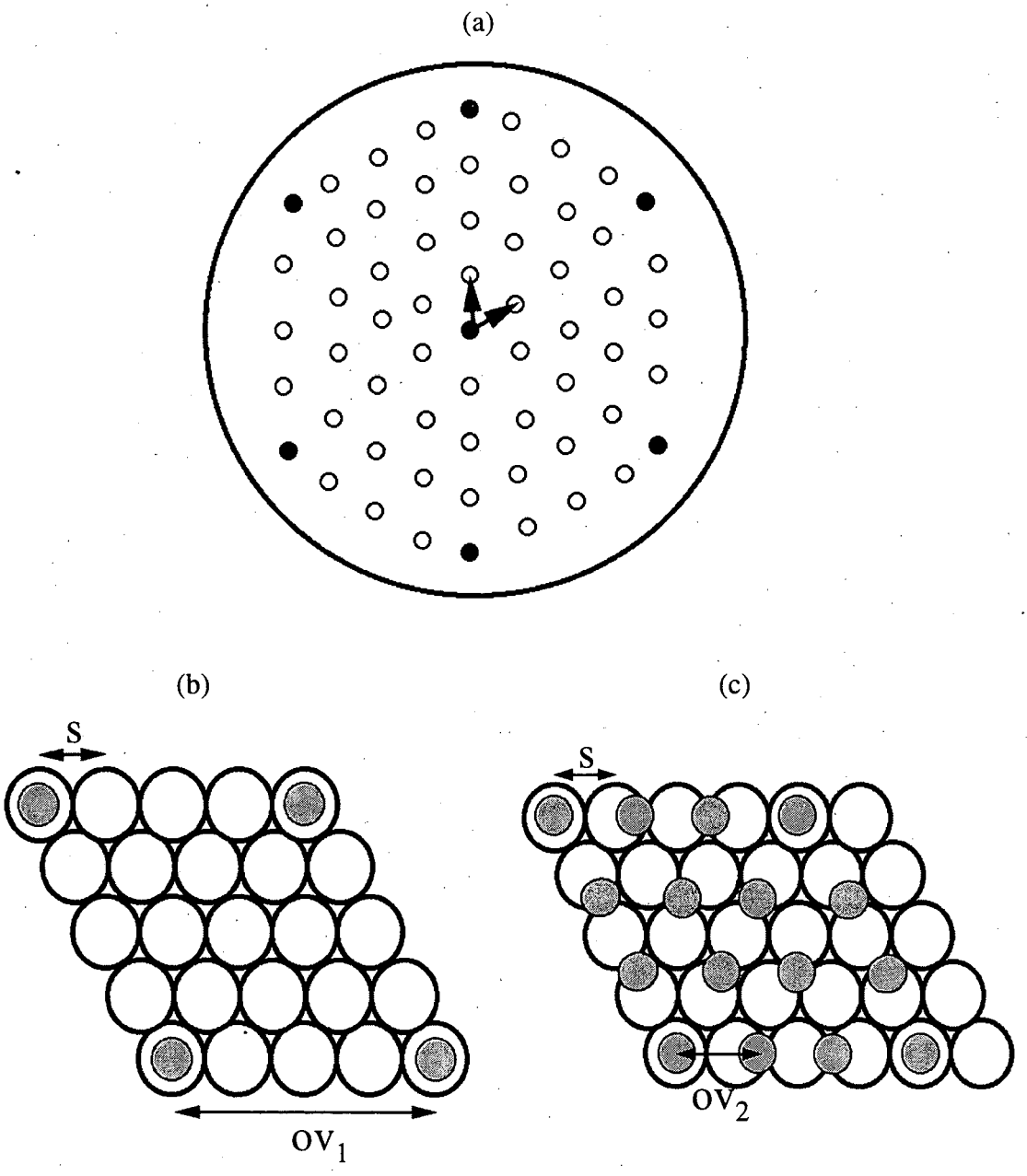

Fig. 2.3. (a) (4 x 4) LEED pattern with two possible real space structures that could produce such a pattern. The first structure (b) is an overlayer with an overlayer unit cell parameter (ov_1) four times larger than the substrate's unit cell parameter (s). The second structure (c) is a coincidence lattice where three overlayer unit cells of length ov_2 are in registry with four substrate unit cells of length s

lattice and then this scattered electron can diffract again from the substrate's surface mesh.

The effect of multiple rotated domains is the production of additional diffraction beams in the observed pattern [24]. The most common reason for the creation of multiple rotated crystalline domains is when the overlayer lattice has a lower symmetry than that of the substrate. In this situation, the higher symmetry of the substrate has to recovered in the overall LEED pattern. This is best understood by examining Fig. 2.4. Fig. 2.4 is the real space representation of a square overlayer on a hexagonal face of an fcc substrate. In this arrangement, three domains are needed. We see that all the overlayer atoms in these three domains interact with equivalent substrate atoms, as a result all three domains are isoenergetic to one another. This situation produces three times the number of diffraction beams due to the existence of three sets of surface unit vectors.

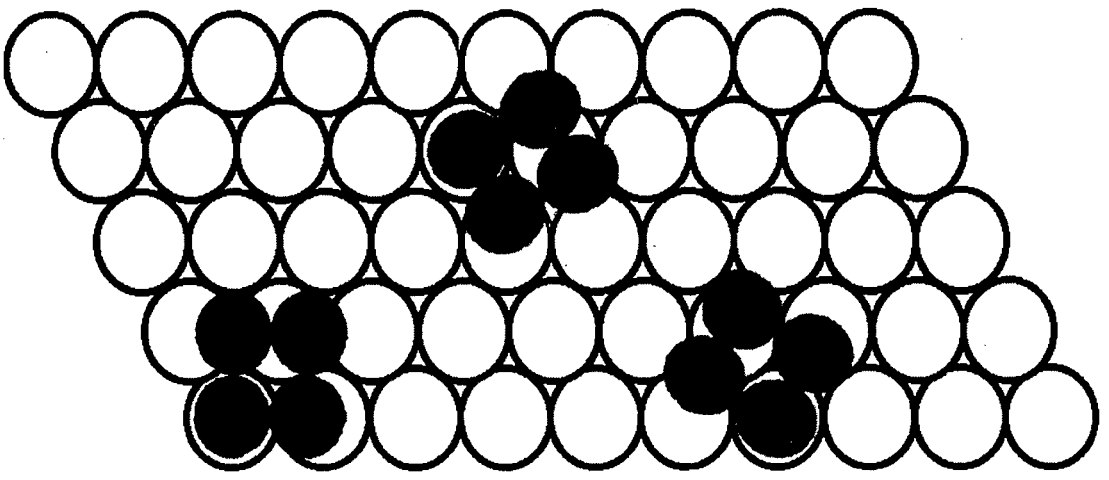

Fig. 2.4. Illustration of the rotational domains that arise when an overlayer with square symmetry is adsorbed onto a hexagonal substrate. In order to recover the symmetry elements of the more symmetric substrate, the overlayer must have a minimum of three domains rotated 120° from on another.

An additional piece of information that can be found by a visual examination of the LEED pattern is the relative ordered domain size. The angular spread of the diffraction beam is determined by the following equation [24].

$$\delta\varphi \approx \frac{\lambda}{2 \cdot M \cdot a_1 \cos(\theta)} \tag{2.8}$$

where $\delta\varphi$ is the angular spread of the diffraction beam, λ is the wavelength of the incoming radiation, M is the number of scatters in the unit cell, φ is the angle of incidence and a_1 is the unit cell length. From equation 1.8, the broader is the diffraction spot; the smaller is the number of scatters (i.e. the smaller the domain which is creating this diffraction spot). One use of equation 1.8 is to compare the overlayer's LEED spots to those of the substrate. If the overlayer spots are larger than the substrate's diffraction spots, then one can qualitatively state that the

domain size is smaller in the overlayer relative to the substrate. Quantitative data requires the crystal to be in the exact focal point of the electron energy analyzer, since the spot profile ($\delta\varphi$) will be distorted due to inexact electron energy selection.

2.5 VACUUM APPARATUS

2.5.1 Sample Holder

Specialized crystal manipulators are needed for quantitative work, because of the need to orient the crystal at a known incidence angle to the electron gun. To accomplish this task, the manipulator must have some degree of tilt out of the manipulator's plane. In this study, a three point collar with precision micrometers placed between the rotary drive's ball and socket joint provided this motion. An alternate method in aligning the crystal is to manufacture a tilting stage directly to the crystal holder itself. This tilting stage is actuated by an attached linear drive integral to the rotary drive. The advantage of this approach to tilting the crystal over the three point stand is the increased range of motion and the relative separation of the tilt movement from the other degrees of freedom of the crystal. Main advantages of the three-point stand mechanism are its ease of adaptability to non-specialized manipulators and its simplicity of operation which requires less moving parts, consequently less maintenance.

Another common feature, although not required, is the ability to cool the crystal below 200 K. This can be performed by flowing liquid nitrogen (LN_2) through cryogenic feedthroughs and into a copper block which is thermally connected to the crystal. Proper isolation from external heat sources is a requirement in order to achieve the lowest temperature. In the current experimental setup, this method can cool the attached crystal to 120 K. Another experimental setup is to manufacture a small LN_2 reservoir near the top of the manipulator, then thermally connect this reservoir to the crystal holder with copper or gold braids. Thermal isolation of the crystal stage is extremely important with this configuration, since the cooling is limited by the conduction of the metal braids. The use of conductive braids is mechanically simpler, but the ability to increase the coolant flow allows for more flexibility (i.e. larger room for error) in the design of the sample holder. The reason for cooling the crystal is to minimize the lattice vibrations of the solid [2]. Diffraction intensity is increased when the root mean square displacement of the atoms due to lattice vibrations is minimized. This effect is common for all diffraction techniques and has been modeled by the Debye-Waller factor. The Debye-Waller factor has the form Exp(-2M) and changes the observed intensity (I) from the perfectly rigid lattice intensity (I_0) by $I = I_0 \cdot \mathrm{Exp}(-2 \cdot M)$. Assuming the thermal vibrations are isotropic the Debye-Waller factor takes the following form.

$$\mathrm{Exp}(2 \cdot M) = \mathrm{Exp}\left[\frac{-(3 \cdot \hbar^2 s^2 T)}{m_a k_b \theta_D^2}\right] \qquad (2.9)$$

Where T is the thermodynamic temperature, k_b is the Boltzmann constant, θ_D is the surface Debye temperature and m_a is the atomic mass of the surface atoms. It can be seen that by decreasing the temperature this factor can be lowered, thus increasing diffraction intensity.

2.5.2 LEED Optics

Energy selection of diffracted electrons is performed with the use of a high pass filter constructed of four hemispherical concentric grids illustrated in Fig. 2.5 [23]. The first grid nearest to the sample is at the ground potential as are the electron gun drift-tube and the sample. This grid provides a field free region so the backscattered electrons are not deflected by stray electrostatic fields. The next two grids are electrically coupled and are negatively biased at a potential slightly below the electron beam energy. These grids represent the filtering section where only the quasi-elastically scattered electrons are allowed to pass. One grid can perform the duty of the two coupled grids, but an additional grid is need to create a homogenous electrostatic repeller field; the reasoning will be discussed shortly. The fourth grid is also grounded to provide a field free region for post-diffraction acceleration.

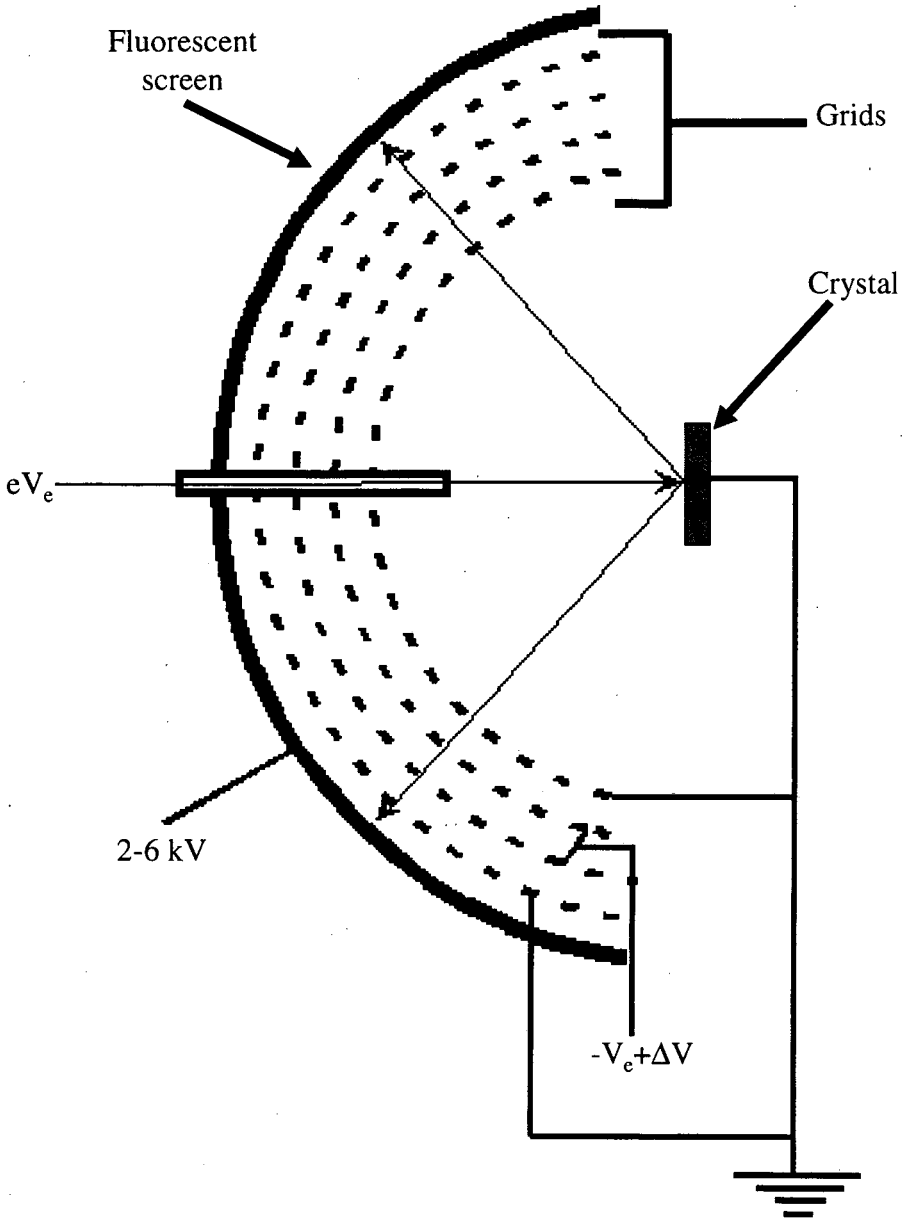

Fig. 2.5. Diagram of the LEED optics, where V_e determines the electron energy

In modern commercial LEED units, the diffraction pattern is visualized by post-filtering acceleration of the scattered electrons onto a fluorescent screen held at a positive potential of 2-6 kV. This large bias voltage is the reason for the addition of another repeller grid. The phosphorous screen's light is peaked in the green area of the spectrum at 525 nm. Being of the rear-view design, the screen is a Pyrex hemisphere coated on one side to allow for the viewing of the pattern from behind.

The entire unit (optics, phosphorous screen and electron gun) is surrounded by a μ-metal cylinder to prevent deflection of the diffraction beams from stray magnetic fields. μ metal, when properly annealed, is an alloy with a high magnetic permittivity. Its bulk composition is 77.2% nickel, 14.9% iron, 4.8% copper and 1.5% chromium.

2.5.3 Electron Gun

The source of electrons is produced by thermionic emission from a directly heated thoriated tungsten bent filament or from a indirectly heated single crystal of $LaB_6(100)$. The use of a LaB_6 single crystal complicates the electron gun operation, because great care is used when turning on the filament or risk fracturing the single crystal. The reason for using such a sensitive material is its low work function (2.69 eV) compared to tungsten (4.5 eV), thus it has good emission even at low power inputs [26]. The usual configuration of the filament inside the gun assembly is out of the line of sight of the exit aperture. The off-axis mounting of the filament prevents light from the heated filament from

obscuring the light intensity from the phosphorous screen and aids in the cleanliness of the sample by not emitting desorbing material from the filaments surface onto the sample. Surrounding the filament assembly is a Wehnelt cap. The Wehnelt cap is at a negative voltage and restricts the electron flux. The restriction of the flux acts as the first focusing stage. An additional three electrostatic lens extracts, focus and accelerate the electrons. This entire electron beam assembly is mounted in the center of the electron optics allowing room for the crystal to be positioned in the focal point of the concentric grids.

Above 50 eV, the beam diameter is 1 mm with a coherence length of approximately 100 Å [24]. From the beam size, it can be concluded that the diffraction pattern represents an ensemble average of the multiple translation and rotational domains that is illuminated with the electron beam. The coherence length of the beam determines the minimum domain size; a smaller domain will not constructively add to the diffraction pattern. Conversely, if the surface possesses multiple rotated structures larger than the beam size, the experimentalist has to physically raster the electron beam over the crystal to obtain a full understanding of the long range order of the surface.

2.6 LEED DATA ACQUISITION

2.6.1 Camera

The brightness of the diffracted beams within a single experiment can vary from being visible to the naked eye to needing light amplification along with signal averaging to see the spot. The low end of this large dynamic range necessitates a light intensifying camera. Since no camera has the ability to accommodate these extremes, a collection of lens with varying aperture sizes is used to limit the amount of light allowed into the light amplifying camera. There exists two main commercial solutions for light intensification—video tubes or charge coupled devices (CCD). Based on the legacy of this group, a video tube camera is used for all the data collection. The author's experience with data collected from an intensified liquid nitrogen cooled CCD camera demonstrates that the sophistication of CCD technology has overtaken video tubes, and because of the larger commercial use of these devices, the cost of a comparable CCD camera is a fraction of the video tube camera which is currently being used. The specific video tube being used is an silicon intensified target (SIT). A schematic of the SIT tube is illustrated in Fig 2.6 [27]. The tube consists of a curved fiber-optic faceplate that is coated with the photocathodic material S-20 multi-alkali compound (Na, K, Cs and Sb), a silicon diode array target, an electron gun and a number of electrostatic lens for focusing and rastering the electron gun beam. The amplification process begins when light impinges upon the photocathode,

thereby releasing a photoelectron current which is focused with electrostatic lens onto the silicon target. This incoming photoelectron beam generates electron-hole pairs in the silicon proportional to the light intensity. Since the front of the silicon target is maintained at a positive potential, these electron-hole pairs migrate to the rear of the target where an electron beam scans across this area. The amount of electrons needed to neutralize the holes is determined by the difference of electrons supplied by the amount backscattered from the target. This signal current is converted to a voltage and sent to the preamplifier and signal processor.

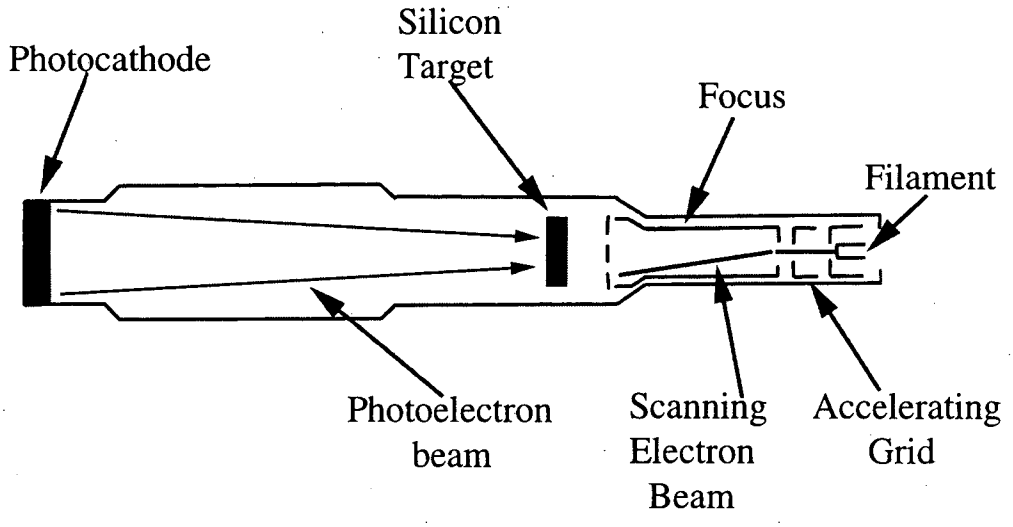

Fig. 2.6. Schematic of the silicon intensified target (SIT) tube used in the LEED data acquisition camera

2.6.2 Frame Grabber

The analog signal that exits the camera is inputted into a real-time digital video processor [10]. All of the 480 horizontal video scan lines are digitized into 512 x 512 pixel image with each pixel assigned an eight bit shade of gray proportional to the light intensity. Eight bit color corresponds to a scale of 256 levels in which to display the light intensities. This image is stored in the frame memory buffer which is a one megabyte RAM allocation located on the video processor system board. A user defined number of digitized frames are averaged to increase the signal-to-noise ratio (s/n). Signal-to-noise of a single averaged image is increased by $\sqrt{N}$ over the signal-to-noise ratio of a single image, where N is the number of frames used to produce the averaged image. The interim image before all the N number of frames are averaged is stored in the accumulation buffer, another 1 MB of RAM on the board. After all the frames needed for the average are collected and summed, the final integrated image is moved to the destination buffer and is finally written to the hard drive. The time needed to perform this procedure is about four seconds when N=128 frames. The file which represents the final averaged image is not saved as a standard image format such as GIF, JPEG or TIFF. In order to manipulate the image, the binary data has to be loaded into the video processor.

2.7 EXPERIMENTAL METHOD

2.7.1 Sample Positioning

For quantitative work, the angle of incidence of the impinging electron beam has to be determined to within 0.5° or less. The most convenient incidence angle is 90° relative to the surface, because it is the easiest angle to determine accurately. Crystal alignment is aided by the fact that the symmetry of the beam intensities have the same symmetry as the crystallographic plane being investigated. The most used method in determining normal incidence of the electron beam on the sample begins by finding a beam energy where a set of symmetry equivalent diffraction spots vanish. If the symmetric spots disappear at exactly the same energy, then the sample is positioned correctly. This method is very time consuming, although it can be expedited by first finding the normal incidence position of the clean single crystal and then replicating this position when a film is adsorbed. Efficient sample positioning becomes very important when working with extremely electron beam sensitive materials such as the alkali halides and the alkali earth halides. Severe disordering of these materials results after long electron beam exposures, resulting in a finite film lifetime. This is not usually the case with clean metals, oxides or most adsorbed gas films. The vanishing method is only a qualitative measure of normal incidence; the true test involves the extraction of the intensity versus energy curves (I-V) for each of the symmetric beams and then comparing each to one other. The positions of the

peaks and valleys of these curves with respect to energy should not deviate more than the size of the experimental energy grid, 2 eV in all the presented data. If the deviations are beyond this requirement, the data are considered unusable.

Because of the hemispherical geometry of the energy filtering grids, accurate energy selection of the backscattered electrons can only occur if the sample is in the focal point of the LEED optics [27]. This requirement is considered secondary to the more important normal incidence criterion. Anisotropies of the spot profiles caused by the sample being out of the focal point do not affect the intensity data, because the beam intensity is integrated over the entire spot.

2.7.2 I-V Curve Extraction

The benefit of the current data collections setup is the ability to perform the beam intensity extraction after the collection. Intensity extraction is performed with a computer program coded by Dr. Ulrich Starke. The user manually tracks the diffraction spots with an octagon which determines the area to be integrated. This intensity is then adjusted with respect to the background intensity. The background intensity is determined from the integration of the pixel intensity outside of the octagon. This method can be problematic if the LEED pattern is very dense, by causing an incorrect value for the background intensity due to the other beams being in the vicinity where the background intensity was being determined. Caution should be used when tracking spots. Integration should stop if the spot becomes blocked by a screen defect or the

electron gun support, since an incorrect background intensity and relative beam intensity would be calculated.

2.8 QUANTITATIVE ANALYSIS

2.8.1 Introduction

An in-depth description of the LEED calculations are beyond the scope of this work. The author refers the reader to the references by Van Hove et al. and Pendry for a detailed discussion of the theory [2,5,28]. This section will provide an overview of the physical processes which led to the development of the dynamical scattering theory and the theoretical models used to simulate these processes.

As discussed in the diffraction condition section, the diffraction intensity (I) is proportional to the square of the geometrical structure factor. This geometrical structure factor for polyatomic crystals can be separated into one part describing the scattering of the atoms (F) and geometrical positions of the basis atoms (G) [24]. Now, equation 1.5 has the following form.

$$I \propto |F|^2 |G|^2 \tag{2.10}$$

G, the lattice factor, is unaffected by the switch from the kinematic to the dynamical scattering theory. F, the scattering factor, has to be the modified extensively, because the scattering processes are markedly different in the dynamical limit than in the single scattering kinematic limit.

In x-ray diffraction (i.e. the kinematic process), F is synthesized from the summation of the individual atomic scattering factors which make up the basis of the crystal. This procedure describes the scattering by the atoms with spherical waves, since the atomic scattering factors have a spherical scattering density. Interaction between the incoming radiation and the atoms is negligible, thus conserving radiation energy and momentum in all directions. In dynamical scattering, the scattering potential described by F differs greatly from the one modeled by the kinematic assumptions. The two main differences are 1. Strong interaction of the radiation with the atoms (surface specificity) 2. Interaction of the incoming radiation with the backscattered radiation (multiple scattering). These characteristics manifest themselves in the new scattering potential as inelastic scattering events, angular dependent scattering and backscattered radiation interaction.

A structural analysis begins with the synthesis of the scattering potential, then an array of possible models are created using the available chemical knowledge of the system and the qualitative observations of the LEED pattern. Multiple scattering simulations are performed upon each of these models and theoretical intensity versus electron energy (I-V curves) are calculated. These theoretical curves are compared to the experimental curves, and their similarities are quantified by a figure of merit (R-factor). The model with the lowest R-factor and chemically reasonable structure is considered to be the structural solution. A global minimization of the R-factor is not guaranteed by the search methods

currently employed by the computer programs, thus a through trial-and-error search combined with reasonable parameters for bond distances and angles from other analytical techniques are the main tools in finding the "correct" structure.

2.8.2 Scattering Potential

A periodic muffin-tin potential is used to describe the potential of the near surface region [2,25]. There exists a fundamental problem in creating such a potential—the electron-electron interaction. In order to overcome this problem, the independent electron approximation is employed. In the independent electron approximation the electron-electron interactions are represented by an effective one electron potential. This one electron potential is derived from atomic free-atom wavefunctions which are truncated at the isotropic muffin-tin radii which is essentially the atomic radii. Electron exchange is treated locally through the Slater approximation.

The scattering properties of the constituent atoms are indirectly found by measuring the atomic scattering amplitudes of the incident plane and spherical waves. Incoming and outgoing radiation is most conveniently described by plane waves. This plane wave formalism is a good approximation of reality, since the source for the incoming electrons and the detector for the backscattered electrons are a long distance away from the crystal. Waves with spherical symmetry are the natural choice for scattering between the ion cores because of the spherical symmetry imposed on the muffin-tin radii. The best way to exploit the inherent conveniences of both symmetries is a partial wave analysis of the incident waves

upon the potential. In a partial wave analysis, plane waves are described by using a basis set of spherical waves. Now, that the scattering potential, incoming waves and resultant waves all have spherical symmetry; only the radial part of the Schrödinger equation is needed to be solved. Phaseshifts for the scattered waves are created by matching the logarithmic derivatives of the wavefunctions both inside and outside of the muffin-tin sphere. These phaseshifts result as a consequence of the wavefunction gaining energy by passing over the attractive ion core potential, thus shortening its wavelength within the muffin-tin sphere. The outgoing wave will be phaseshifted with respect to the incoming one.

In the dynamical scattering calculations that follow the determination of the scattering potential, the phaseshifts are the only quantities used to describe the potential around the atoms. The model that is used in the theoretical experiment is an array of point scatters with phaseshifts assigned to each. Temperature effects are simulated by multiplying the phaseshifts with an isotropic Debye-Waller factor. Inelastic scattering is included by modifying the Schrodinger equation with a complex potential energy term.

$$\frac{\hbar^2 k^2}{2m}\Psi = (E + V_{or} + iV_{oi})\Psi \qquad (2.11)$$

This modification simply eliminates radiation flux; it does not try to model the physical processes responsible for such losses.

2.8.3 Dynamical LEED Calculations

Simulated LEED intensity calculations are split up into two parts: 1. Scattering within a composite layer 2. Scattering between composite layers. Composite layers are layers with more than one atom per unit cell. The composite layers can have multiple subplanes which can be coplanar and can consist of multiple chemical species, but they must have the same Bravais lattice symmetry. Multiple composite layers are stacked on top of one another to create the substrate and the overlayer in a LEED calculation.

The transmission and reflection of the incident electrons within a composite layer are calculated via the Combined Space Approximation (CSA) or Beeby inversion scheme [2,5]. Physically, an impinging plane wave is factored into spherical waves through a computationally intensive matrix inversion. The scattering paths of the spherical waves are calculated by applying the scattering t-matrix, which define the atomic potential of the constituent atoms, along with free-space propagation functions (Green's functions). Multiple scattering events are fully accounted in determining the characteristics of the transmitted and reflected waves exiting the composite layer, thus this method is an exact treatment of the scattering process. The number of multiple scattering events is determined by the inelastic losses within the material. After all the scattering has been determined within the composite layer, a Huygens construction of spherical wave fronts from a periodic array of spherical scatterers is used so a plane wave

formalism can be applied to describe the transmitted and reflected radiation. A full mathematical description can be found in reference [2].

Between composite layers, perturbative method is employed. This method known as Renormalized Forward Scattering (RFS) does not treat the scattering exactly as in the Combined Space Approximation [2,5]. The RFS method first gathers the following information that result from the CSA calculations: 1. the number of transmitted and reflected waves 2. intensity of the transmitted and reflected waves. RFS follows the transmitted waves layer-by-layer until its intensity goes to zero due to inelastic effects, then starting from the deepest layer reached by the transmitted wave, the exiting wave is created by summing up all the reflected waves' intensity due to the previously transmitted ones. This first pass represents the first order result. Higher order results are calculated by repeating this process until the exiting intensity extinguishes due to inelastic losses. Convergence of RFS is problematic if the inelastic effects are small or the interlayer spacing between composite layers is too small (<1.0 Å). Usually, RFS uses 12-15 layers and requires three to four orders to achieve convergence.

2.8.4 The Pendry R-factor and the Tensor LEED Approximation

After a fully dynamical calculation has been performed on a trial structure, a figure of merit (R-factor after reliability factor) quantifying the goodness of fit between the theoretical and experimental I-V curves is needed to determine the structural solution. There exist many definitions of R-factors, but the most widely reported one is R_{Pendry} [29].

$$R_{Pendry} = \frac{\int (Y_e - Y_t)^2 dE}{\int (Y_e^2 + Y_t^2) dE} \qquad (2.12)$$

where $Y = \frac{L}{1 + V_{oi}^2 L^2}$ and $L = \frac{dI}{I}$ and I is intensity of the I-V curve

This R-factor is used most because of its high sensitivity to structural parameters which affect the I-V curves' peak positions, and its weak dependence on nonstructural parameters which affect the beam intensities.

With the wide availability of fast computers, the most time consuming part of the LEED analysis is the creation and inputting of trial structures into the program, since this task is left to the theorist to perform--until the invention of tensor LEED. The advent of tensor LEED (TLEED) is a direct application of first order perturbation theory [30].

$$\delta A \approx \sum_n \left\langle \vec{k} + \vec{g}; \text{out} \middle| \delta t_n \middle| \vec{k}; \text{out} \right\rangle \qquad (2.13)$$

Where $\left\langle \vec{k} + \vec{g}; \text{out} \right|$ is the scattered wavefunction, δt_n is the movement of the n^{th} atom, $\left| \vec{k}; \text{out} \right\rangle$ is the incident wavefunction and δA is the change in diffracted beam amplitude. Applying spherical symmetry to equation 1.13, one gets:

$$\delta A \approx \sum_n \vec{F}_n \delta t_n \qquad (2.14)$$

where $\vec{\mathbf{F}}_n$ is a Cartesian tensor (from which the method derives it name) that can be evaluated in tandem with performing the dynamical scattering calculation on a trial structure.

This approximation automatically generates and performs a perturbative dynamical calculation on multiple structures which were derived from one user-defined trial structure. Within the radius of convergence (approximately 0.4 Å) of the approximation, the R-factor space is fully defined. An effective search of this hypersurface is an active area of research in LEED theory. The limited radius of convergence for the TLEED method is due to its neglecting of scattering paths which include more than one scattering event from the displaced atom.

Chapter 3

Experimental Equipment and Procedures

3.1 INTRODUCTION

The maintenance of an atomically clean, well ordered surface is the main challenge to experimentalists. The size of this obstacle can be seen through the application of the kinetic theory of gases which yields a relation between molecular flux (J_M) in units of molecules per square centimeter per second, pressure (P) in torr, temperature (T) in Kelvins and molecular weight (M_w) in moles per gram [24].

$$J_M = 3.51\times10^{22}\frac{P}{\sqrt{T\cdot M}} \qquad (3.1)$$

Using oxygen, whose partial pressure in the atmosphere is about 190 torr, at 300 K, a flux of 6.81×10^{22} molecules/cm^{2}s is incident onto a surface with about 10^{15} surface sites, thus adsorbing a monolayer of gas in 1.2×10^{-8} second, assuming a unity sticking probability of the adsorbed gas. The value for the number of surface sites was estimated by the molecular density of Pt atoms in its unreconstructed (100) face--1.3×10^{15}, which is representative of the metals used in this study. Through the use of ultra high vacuum technology, the length of time before the surface becomes contaminated can be extended by orders of magnitude.

For example, the system, where all the experiments were performed, maintains a base pressure of 5.0×10^{-10} torr with the majority of the residual gas being CO, carbon monoxide. With these conditions, a monolayer of gas does not adsorb for 1.45 hours. Since the preparation and the subsequent analysis of the surface occurs within 40 minutes, cleanliness of the surface is assured.

3.2 THE UHV SYSTEM

3.2.1 Ultra High Vacuum (UHV) Chamber

All experiments were performed in a 60 liter, stainless steel UHV chamber (Fig. 3.1) which consisted of four eight inch ports and four 2.75 inch ports on the side of the chamber arranged perpendicular to the chamber's vertical axis. Three additional 2.75 inch ports were present on top of the apparatus above one of the eight inch ports, so the focal point of these ports was half way between the chamber's center and the closest wall of the chamber. Five additional 2.75 inch ports ringed the base well along with a six inch port. The top of the chamber and the bottom of the base well had a six inch and a ten inch port, respectively. Being of Ultek manufacture, all the ports welded to the chamber possessed rounded edged flanges to mate with the oxygen free electronic grade copper gaskets used in the creating the junction between the bell jar and the various instrumentation.

Unlike the chamber itself, the instruments were mounted on Varian or Varian licensed Conflat™ metal flanges which has a conical sealing edge to be

used with copper gaskets. The sealing action is begun by pressing the a flat copper gasket between the rounded flange edge of the chamber with the conical edge of the Conflat flange, thus causing a lateral cold flow of the much softer copper metal of the gasket itself. Arresting the flow of the gasket material is the vertical wall of the flange and a capture groove that is concentric to the sealing knife edge.

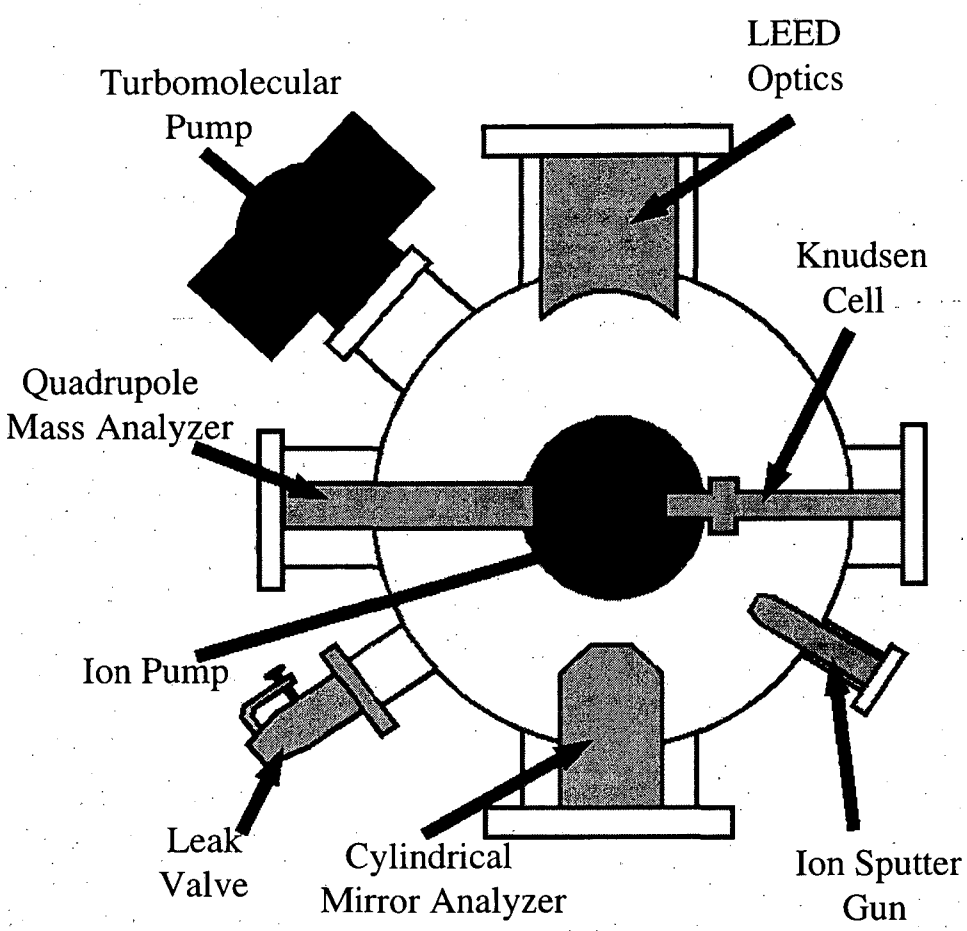

Fig. 3.1. Top view of the analysis chamber used in all the experiments. All the surface preparation and analysis equipment (LEED optics, Knudsen cell, CMA, quadrupole mass analyzer and ion sputter gun are all located on the same plane in the middle of the chamber. The leak valve and all the pumps are below.

A benefit of this limited flow of the gasket material is the production of a very high pressure at the interface between the gasket and the flange. This pressure causes the copper to fill the small surface defects present in all flanges, resulting in an excellent seal. The seal is reliable through a temperature range of 73-723 K and can hold a vacuum of 1.0×10^{-13} torr.

The base well was sealed to the analysis chamber through the use of copper wire. This seal differs from the Conflat/rounded edge seal by the use of gendered mating flanges and a 0.080 inch diameter oxygen free electronic grade copper wire taking the place of the copper gaskets. Although the equipment is different, the theory of creating and maintaining a seal is the same as discussed previously--cold flow of the much softer gasket material. To create the pressure needed, the wire is compressed between the flange's beveled edges. These edges force the gasket material to move towards the high vacuum side, but the wall limits the flow of the copper. This limiting action creates pressures high enough to fill the scratches and other irregularities found in the sealing regime.

3.2.2 Vacuum Pumps

The base pressure of $<5.0\times10^{-10}$ torr is maintained through the use of a 300 L/s triode ion sputter pump. The ion pump uses the fact that ionized atoms and molecules have an increased reactivity with surfaces than their neutral counterparts. This pump represents the most widely used example of the gas entrainment pump family to create and maintain UHV. The heart of the sputter-

ion pump is the Penning cell [31]. A modern ion pump uses a large number of these cells which are created from a parallel array of short stainless steel anodic tubes with two titanium plates spaced 4 mm from either side of these tubes. Many large iron magnets surround these Penning cells to create a strong magnetic field parallel to the tubes' long axis. Electrons liberated from both cathodic plates are electrically-magnetically confined into tight spiral paths in the anodic tubes, thus increasing the possibility of ionizing entering gas molecules by collisions with the entrained electrons. These gas ions are accelerated toward the cathode, impact the surface, release secondary electrons to be trapped in the anodes tubes and sputter cathode material on the tubes and the walls of the pump. These processes allow for multiple pumping mechanism: 1. adsorption or precipitation after molecular dissociation 2. burial under freshly sputtered titanium of ions and neutrals 3. gettering of active gases through the formation of stable titanium compounds.

Although an ion pumps can be and are made from just two electrodes (diode pump with the tubes at a high positive potential and the titanium plates at ground), this arrangement is found to pump noble gases very inefficiently. The explanation can be seen by the mechanism used to pump noble gases--ion and neutral atom burial in the cathode. In a diode pump, newly incoming accelerated atoms collide with previously buried material, resulting in the remission of the previously buried gas molecules. To overcome this problem, the triode version the ion pump was devised by slotting the titanium cathode plates and putting them at a very negative potential and leaving the tubes and the walls of the pump at

ground. Ion and neutral burial is enhanced in this arrangement, since the sputtering of the cathodic titanium is performed on a separate electrode than the final resting place of the noble gas ions and neutrals. With the sputtering process decoupled from the burial, the pump is less vulnerable to reemission of previously buried atoms. This advantage is makes the triode pump the best choice for use in systems whose pressure occasionally fluctuates, which is the case in a molecular beam epitaxy (MBE) set-up. The main disadvantage is the smaller amount of cathodic material when compared to the diode pump due to the fact that the cathode has less bulk in the triode pump.

The best pressure was achieved when the ion pump is used in combination with another UHV generating pump. This is due to the fact that the leak rate of the system was above the duty of the ion pump alone, as a result of imperfections in the manipulator Conflat sealing edge. Originally, a 800 L/s oil diffusion pump performed this extra pumping duty. The method of operation of this pump is quite different than that of an ion-sputter pump, because a different pumping principle is used. The principle used in an oil diffusion pump (DP) is gas transfer [31]. Pumps of this type remove gas molecules in a preferred direction via momentum transfer or positive displacement, thus resulting in a compression of the gas and eventually to the ejection of it into the atmosphere. In a diffusion pump, vapor jets provide the method of transferring momentum to incoming gas molecules. The vapor is created by boiling a low vapor pressure, high molecular weight, silicone-hydrocarbon blended fluid (Santovac 5) in an resistively heated

boiler until it reaches its boiling point. The vapor is directed up a chimney then down and out through a number of nozzles towards the water cooled walls of the DP. The purpose of the nozzles is to create a number of high compression pumping stages in the pump. Any gas molecules diffusing into this vapor stream are given a downward momentum and passed on to a high pressure region.

These pumps consist of no moving parts, so they are very tolerate of operating conditions in which excess particulates or reactive gases are involved. DP's also provide very high pumping speeds relatively inexpensively. The use of a boiling liquid is the main disadvantage of the diffusion pump, because they continuously backstream vapor, an obvious detriment to the maintenance of a UHV environment. The use of a water cooled cold cap on top of the chimney in combination with a liquid nitrogen cooled trap between the experimental chamber and pump allow a diffusion pumped system to achieve pressures on the order of 10^{-10} torr. In working with such a system, the operator has to be fastidious in filling the dewar that provides the liquid nitrogen for the trap or risk contaminating the chamber with a low vapor pressure oil film which requires a long, hot bake-out in order to recover UHV conditions.

Even with a properly maintained system, there exists some hydrocarbon vapor backstreaming into the analysis chamber. When working with platinum, a known catalyst for cracking hydrocarbon, it becomes a necessity to eliminate all sources of hydrocarbons, thus prompting the replacement of the diffusion pump by a 330 L/s turbomolecular pump. Properly venting the pump immediately after

shutdown eliminates backstreaming of the bearing lubricating oil and spins down the blades from 60,000 RPM in less than two minutes.

Like a diffusion pump, a turbomolecular pump is a gas transfer pump, but momentum transfer is exacted by multiple stages which consist of a moving rotor and a fixed stator [31]. The pump looks like a jet engine with its bladed turbine mounted on a high speed motor and slotted stator blades mounted on the pump body. The turbine provides the momentum transfer of the gas molecules towards the outlet of the pump with the stator blades preventing the molecules from migrating back into the chamber. It is typical for a turbomolecular pump used for UHV production to have 3-4 compression stages, similar to the number of stages in a diffusion pump.

To create a pressure difference between the individual stages, each stage has to possess a different pumping speed from other. This can be achieved by either rotating the rotors of each stage at a different speed or through changing the blade design in each stage. Technically, it is easier to modify the blades' angles, spacings and lengths rather than including a variable speed transmission to drive multiple copies of the same rotor. Modern turbomolecular pumps engineer the blades nearest the inlet to have the highest pumping speed and the smallest compression ratio and the blades closest to the outlet to have the opposite criteria.

3.2.3 Vacuum Gauges

The chamber pressure is measured indirectly with a nude ionization gauge inserted into the system through one of the 2.75 in. ports located on the base well.

A direct pressure measurement in the high and ultra-high vacuum region is not practical, since very specialized equipment is needed to quantify the small amount of force that is produced with these gas densities. The in-vacuo transducer utilized is a hot cathode version with the Bayard-Alpert geometry [31]. The transducer consists of a heated biased filament, located outside a wire grid which is held at a positive 150 V, radiating thermionic electrons. This grid imparts enough kinetic energy to the electrons to ionize any background gas molecules which pass in the vicinity of the gauge. The resulting positive ions are then attracted to a thin collector wire in the center of the grid which is held at a negative 30 V. Upon collision of the ion with the collector, the ion is quickly neutralized and electrons are emitted from the wire's surface, a phenomenon that was first discovered by Oliphant for He^+ ions incident on a Mo target. Since the collector is connected to a power supply and ammeter, a current measured and is proportional to the number density of residual gas molecules.

The effective pressure range is 10^{-4} to 10^{-11} torr. The high pressure limit is a result of the material in which the filament is constructed. Thoriated iridium filaments provide good "burn out" protection in the high pressure range, especially for an oxygen rich environment. The lower limit if due to the following physical process. The thermionic electrons from the hot filament collide with the accelerating grid producing soft x-rays. These resultant x-rays, when striking the collector, produce photoelectrons which are indistinguishable from the electrons produced by the incoming positive ions. Because of this x-ray limit of the ion

gauge, even in a perfect vacuum, i.e. no gaseous species present, there would be a non-zero ion gauge reading due to these photoelectrons.

Higher pressures (1 to 10^{-3} torr) such as those found in the foreline of the turbomolecular or diffusion pump are monitored with a thermocouple gauge. In this gauge, a filament is heated by a constant current power supply, and a small thermocouple is spot-welded to the middle of this filament. The voltage of this thermocouple is inversely proportional to pressure observed due to the changing thermal conductivity of the system at different pressures. For example, at high pressures, there exists sufficient gas molecules to transfer heat from the filament to the outside walls of the gauge itself, thus lowering the temperature of the filament. In high vacuum, the lack of available gas molecules hinders this cooling effect.

3.2.4 Gas Introduction

Gases needed for cleaning the single crystal were introduced via one of the two Varian variable leak valves located on the base well of experimental chamber. This valve is capable of producing a stable leak rate as low as 1.0×10^{-10} torr-liter/sec, though the translation of a movable sealing piston connected to a long cantilevered arm that is actuated by a extra-fine pitched threaded screw. The seal is created by an optically flat sapphire crystal, located on a movable piston, pressed against a captured copper gasket. Care should be exercised when working with these valves, since the point of closure can not be determined by feel. These valves are usually adjusted so that the closed position is exceeded when the user

feels resistance to the clockwise rotation of the knob. Excessive force will shorten the life of the copper gasket or worse crack the sapphire, thereby creating a permanent leak in the valve. Luckily, both of these parts are user replaceable. One of the two leak valves is used to backfill the chamber with gas, and the other is fitted with a direct doser to introduce gas directly onto the sample itself.

On the high pressure side of the leak valve is a stainless steel gas manifold which is interfaced with the gas cylinders through Swagelok connections. The use of Swagelok is motivated by the convenience of making connections without the use of welding or brazing on fittings. Since a manifold system is used to supply the two leak valves, flushing out the system was of great importance if the purity of the gas is to be maintained. It was standard practice to flush the lines three times with evacuation between each flushing before the gas was used in the experimental chamber. After the gas was let into the chamber, the purity was then checked through the use of the quadrupole mass spectrometer.

3.2.5 Manipulator

The manipulator used in these experiments was an off-axis one with x, y, z translation and rotation in the plane perpendicular to the manipulator's axis and tilt. The x-y translation stage is micrometer driven on cross roller bearing slides. This stage is mounted to two stainless steel rear guide bars and connect to a third micrometer which is the z translation actuator. The use of high precision micrometers in the translation stages allows reliable repeatability in positioning the sample for the various experimental procedures. The rotary drive consists of a

standard length stainless steel shaft connected to a 2.75 in Conflat flange that houses the bearings for the rotational motion. The rotary drive is attached to a three point mount located on top of the x-y stage. The three point mount allows for secure and repeatable tilting of the manipulator through its use of three micrometers located at its contact points with the stage.

The sample is mounted to the manipulator by first spot welding 0.005 in. Ta foil strips to the back of the metal crystal. This assembly is then spot welded to two additional 0.030 in. Ta strips that are attached to a Mo face plate by 0-80 screws. It is important to note that in order to achieve normal incident of the Pd(111) sample to the low energy electron diffraction (LEED) unit's electron gun, small washers were used to shim the crystal assembly by placing them below the second set of Ta strips. The multiple pieces of Ta are used to mount the crystal, since spot welding any material other than Mo to the Mo face plate is very difficult, and when it is successful, it usually results in a poor weld. This face plate is then attached the copper block that houses the heating and cooling equipment.

Heating was performed through the use of electron bombardment (e-beam). E-beam heating is accomplished by biasing a thoriated W filament located behind the crystal to ≈-1.5 kV, then the filament is slowly heated resistively by flowing 2 A of current causing thermionic emission of electrons from the filament. These energetic electrons are accelerated into the sample which is at ground. The incoming electrons induce phonon excitations within the crystal,

resulting in heating of the sample. The description of the filament assembly, illustrated in figure 3.2, is as follows: A 0.005 in. thoriated W filament with approximately 10-13 turns is inserted in a high purity alumina tube, so to electrically isolate the filament from the copper cooling block. The power leads from the filament is fed into a two hole alumina insert to separate them.

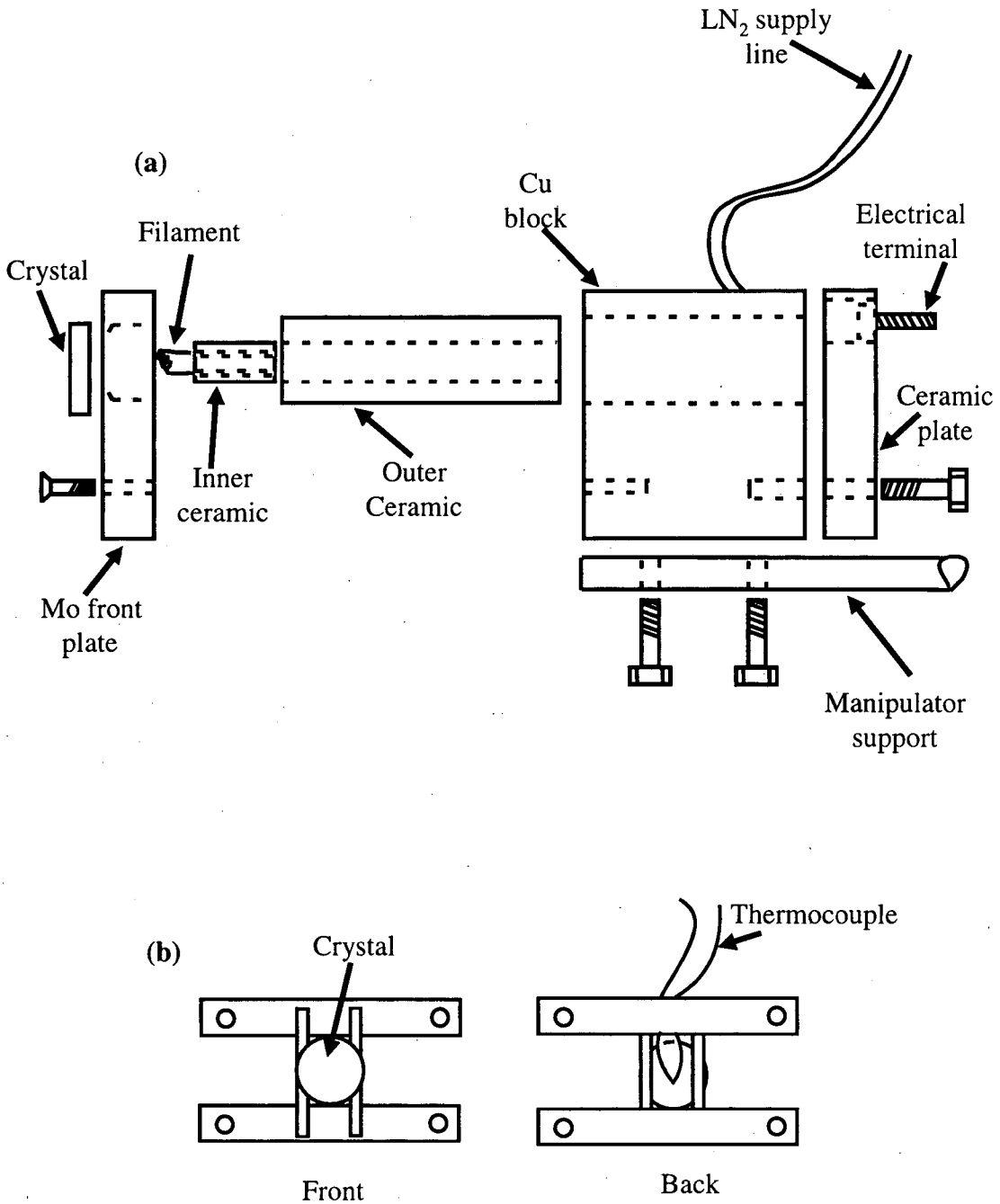

Fig. 3.2. (a) Exploded side view of the manipulator heating and cooling assembly (b) Detail of crystal mounting configuration

These leads are then fed out through the rear of an attached alumina backing plate and are wound around two 4-40 screws. Also connected to these screws are the copper leads to the power feedthroughs, providing power to the filament.

Cooling by liquid nitrogen (LN_2) is accomplished by flowing it through the copper block where the Mo faceplate with the crystal assembly is attached. The copper block is hollowed out to allow for a continuous flow of LN_2. The LN_2 is delivered to the block by stainless steel tubes that are coiled on the vacuum side of the manipulator to allow for rotational and translational freedom.

A thermocouple made from 0.005 in. chromel and alumel wire is spot welded to the back of the crystal to monitor the temperature. This arrangement does not give the exact surface temperature due to this arrangement, but the deviations should be minimal, because of the high thermal conductivity and the thickness (1-2 mm) of the metal substrates.

3.3 AVAILABLE ANALYTICAL TECHNIQUES

3.3.1 Low Energy Electron Diffraction (LEED)

Omicron Spectaleed electronics and optics provided the means for the visualization of the LEED patterns. A Dage-MTI silicon intensified target (SIT) camera in accompaniment with a Matrox real-time video capture card was used to record the LEED images for subsequent I-V extraction and to signal average over multiple exposures. It is important to note that the automatic controls on the SIT

camera were turned off while recording I-V quality diffraction information and the default setting for the frame grabber were employed. By not extracting I-V curves while obtaining the LEED data, a rapid acquisition of a full data set in under 20 minutes of this electron beam sensitive overlayer could be accomplished. LEED intensity data collection followed a standard procedure with the exception of a lower beam current, to minimize electron beam damage to the overlayer [32]. LEED data were collected at normal incidence with a crystal temperature of ≈115 K in 2 eV increments.

3.3.2 Temperature Programmed Desorption (TPD) and Residual Gas Analysis (RGA)

A direct method of determining adsorbate composition is through temperature programmed desorption (TPD). This technique employs a mass spectrometer to monitor the desorbing species coming off the surface of the heated substrate. Usually, the surface temperature is increased linearly through the use of a proportional-integral-derivative (PID) controller, but in this experimental setup, electron bombardment heating of the sample was used, thus making automatic control difficult. The temperature ramp was performed by the experimenter and monitored by a chart recorder. The resulting temperature versus time data is then correlated to the mass signal versus time data.

The mass data are collected through the use of a UTI 100C quadrupole mass spectrometer. The method of operation is as follows. First, desorbing molecules are ionized by 70 eV electrons thermionically emitted from a heated

helical tungsten filament. Electron energy can be adjusted by the user by changing the bias on the ionizer's anode to minimize fragmentation or to optimize the signal of a specific chemical species. These positive ions are then sent to a radio-frequency (RF) quadrupole mass filter for separation [31]. The quadrupole consists of four molybdenum cylindrical rods positioned to approximate the ideal geometry of a hyperbola. Two of these rods possess a positive DC voltage along with an oscillating RF field whose peak-to-peak amplitude is greater than the DC voltage. This half of the quadrupole acts as a "heavy mass" filter, more specifically high m/z ratio pass filter. It fulfills this role, because the heavy cations (high m/z ions) are unaffected by the fluctuating RF field, but the lighter ones are attracted to these rods and are neutralized. The other half with its negative DC potential and RF field performs the "low pass" filtering. The light ions are able to find a stable oscillatory path through the filter, but the larger ions with their increased inertia are eventually attracted to this pair of rods and are neutralized. With these two filters combined, a band pass filter results, thus effecting efficient separation of the ionized species. The separated ions are attracted to a negatively biased stage of an electron multiplier. Upon striking the first stage, secondary electrons are generated and amplified through the use of multiple dynode stages until the signal reaches the anode. The anode signal is read by a PC interfaced to the mass spectrometer's electronics.

Since any molecule bound to the surface is held there with some specific energy, TPD not only reveals the chemical identity of the species, but the binding

energy of the desorbing molecule and hints to the desorption mechanism. In TPD, the main assumption is that the temperature ramp has to be executed so that the pumping rate of the vacuum system exceeds the desorption rate of the surface species. In these experiments, the mass spectrometer is mounted in a position where the ionizer, mass filter and detector is rapidly pumped. It is important to note that the chamber should not be pumped exclusively by the ion pump while performing TPD experiments, since this pump alone does not effectively remove the desorbed materials fast enough. A good test to insure that the system is adequately fulfilling this pumping requirement is to obtain a spectrum at two or more different surface coverages. The mass spectra's intensity maxima should be the same within the error of the instrument and not increase with increasing coverage. With the pumping requirement satisfied, the signal from the mass spectrometer is directly proportional to the rate of desorption with respect to time.

Since rates come directly from experimental observations, a qualitative examination of the resulting spectra readily gives the user the order of the desorption rate and further analysis yields activation energies [33,34]. This can be seen by the following examples for zero and first order desorption mechanisms. Zero order desorption was the most common mechanism encountered in this work, because of the strong adsorbate-adsorbate interactions of the ionic solids. The existence of this mechanism for desorption is a product of strong adsorbate-adsorbate interaction which physically means that the adsorbate is simply condensing on the substrate from the gas phase with no regard for the composition

and surface structure of the underlying substrate. Applying the Arrhenius form of the reaction constant, k, the following equation describes a zero order reaction process:

$$\frac{dN}{dT} = \frac{A}{\beta} \cdot Exp\left(\frac{-E_a}{R \cdot T}\right) \qquad (3.2)$$

Where N is the number of desorbing atoms, T is the absolute temperature, , β is the heating rate, $\frac{dT}{dt}$, A is the Arrhenius pre-exponential, E_a is the activation energy for desorption and R is the ideal gas constant. Since this is a zero order process, the E_a is simply $\Delta H_{sublimation}$. From equation 3.2, a plot of $\frac{dN}{dT}$ of versus T is an exponential curve that will immediately drop to zero when the supply of adsorbate is exhausted. The T_{max} is dependent upon the surface coverage of the adsorbate; the higher the coverage the larger the T_{max}. A plot of $\ln(\frac{dN}{dT})$ with respect to $\frac{1}{T}$ of just the data on the exponentially rising leading edge of the spectrum gives a value for $E_{desorption}$.

A first order desorption process of the adsorbate occurs when there is an attractive interaction between the adsorbate and the substrate, such as chemisorption of the adsorbate to the substrate. The kinetics of this behavior can be described by the following equation which employs the Arrhenius form of the rate constant again:

$$\frac{dN}{dT} = \frac{N \cdot A}{\beta} \cdot Exp\left(\frac{-E_a}{R \cdot T}\right) \tag{3.3}$$

where the variables have the same definitions as in equation 3.2. It can be seen from equation 3.3 that the peak that results from this process is a compromise between the rate constant's exponential dependence on temperature and the rate's inverse dependence on surface concentration. The asymmetric peak shape and the steadiness of the peak temperatures are reliable indicators to a first order desorption process. The reason for the immovability of the peak temperature was explained by Redhead who theorized that the maximum desorption rate occurred when $\frac{dN}{dT}$ was at its maximum, i.e.

$$\frac{d^2N}{dt^2} = 0 = N \cdot A \cdot \left(\frac{dT}{dt}\right) \cdot Exp\left(\frac{-E_a}{R \cdot T_{max}^2}\right) + A \cdot \left(\frac{dN}{dt}\right) \cdot Exp\left(\frac{-E_a}{R \cdot T_{max}}\right) \tag{3.4}$$

$$\text{this simplifies to } \frac{dN}{dt} = \left(\frac{-N \cdot E_a}{R \cdot T_{max}^2}\right) \cdot \left(\frac{dT}{dt}\right) \tag{3.5}$$

$$\text{substitute equation 3.5 into } \frac{-dN}{dt} = N \cdot A \cdot Exp\left(\frac{-E_a}{R \cdot T}\right) \tag{3.6}$$

$$\text{thus yielding } \frac{E_a}{R \cdot T_{max}^2} = \frac{A}{\beta} \cdot Exp\left(\frac{-E_a}{R \cdot T_{max}}\right) \tag{3.7}$$

From equation 3.7, it can be seen that the peak temperature, T_{max}, is independent of surface concentration of the adsorbed species, N. E_a, the desorption energy, is readily determined with the use of equation 3.7, since T_{max} and β are known experimental values and a common estimation for A is 10^{13} s^{-1} which is on the

order of a vibrational frequency. If an experimental determination of A is desired, the heating rate, β, has to be changed by a minimum of two orders of magnitude, because of the small dependence of the Arrhenius pre-exponential, A, to the heating rate.

An ancillary use of the quadrupole mass spectrometer is for residual gas analysis (RGA) of the vacuum system's environment. The determination of the make-up of the background gases allows one to correct the pressure reading received from the ionization gauge. A correction is needed to account for the differences of ionization energy between various compounds, although uncorrected pressures are published here. The observation of a significant amount of diffusion pump oil backstreaming into the system prompted the replacement of the diffusion pump for a cleaner turbomolecular pump to alleviate the carbon contamination on the Pt surface. Since the mass spectrometer was in direct line of sight with the Knudsen cell, the composition of the effluent was easily determined. A final advantage of performing RGA on the system is to insure the integrity of the gas delivery system and the UHV system itself. Leaks in the gas manifold system can be seen as large amounts of N_2 and O_2 signal where there should be only pure argon, a common sputtering gas. UHV leak detection is performed with the use of helium gas flooding the possible leak area. Since helium is not removed well by any pump, it has a long residence time in the chamber and can be easily seen I the background.

3.3.3 Auger Electron Spectroscopy (AES)

Auger Electron Spectroscopy (AES) can be used qualitatively to determine the surface species and quantitatively as a means to find surface thickness and stoichiometry of the adsorbed layer [24]. This versatility is a direct result of the process itself. The Auger process (Fig. 3.3) begins by the ionization of a core electron energy level by an incident electron. After its creation, the core hole can be annihilated by two competing processes:

1. An electron from a higher energy level relaxes into the core vacancy and the excess energy is given to another electron as kinetic energy through a radiationless process. (The Auger Process)
2. An electron from a higher energy level fills the core vacancy, and the resulting surplus energy is released as a photon. (X-ray Florescence)

The surface specificity of this technique, as with LEED, results from the electron's increasing probability to inelastically scatter with increased distance from the surface. The electron's attenuation length is on the order of 50 Å, since the typical Auger energies range from 10-1000 eV.

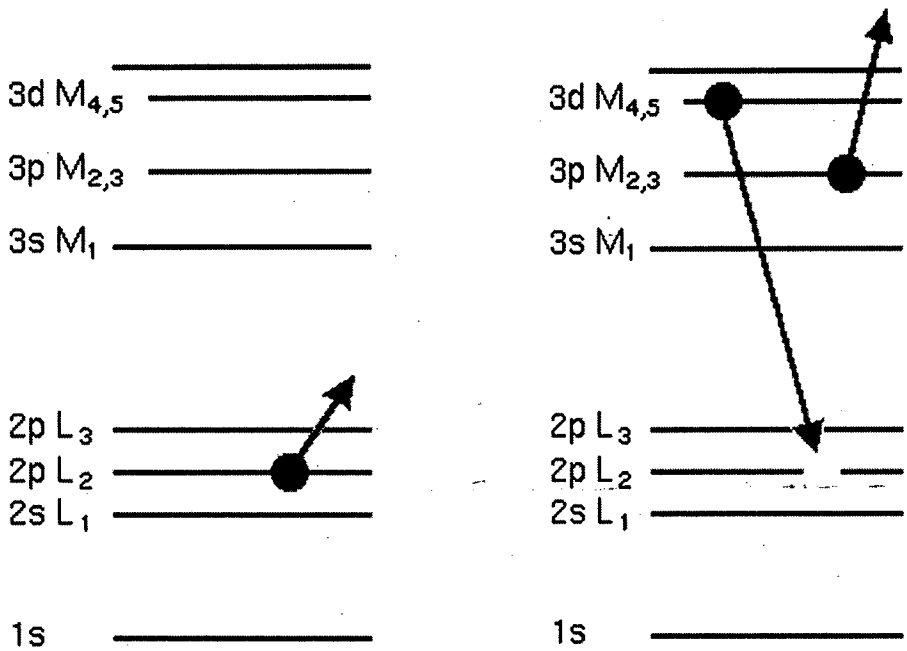

Fig. 3.3. Energy level diagram of a LMM Auger process.

Chemical identity results from the characteristic energies of the ejected electrons. These energies can be predicted by the following equation:

$$E(L_2M_{4,5}M_{2,3}) = E(L_2) - E(M_{4,5}) - E(M_{2,3}) \qquad (3.8)$$

Where the labels L_2, $M_{4,5}$ and $M_{2,3}$ refer to the same levels illustrated in the diagram of the Auger process, and the energies are taken from a table of the isolated atom binding energies. Equation 3.8 provides only a coarse estimate of the experimental values. Other factors which affect the experimental energy are: 1. the work function of the sample 2. the work function of the spectrometer 3.

core level shifts due to chemical environment and 4. electron energy loss mechanism changes that occur with perturbation of the surface structure.

Chemical sensitivity is dependent on both the ionization cross section of the material and the probability of the material to produce an Auger electron instead of an x-ray. The ionization cross section (Q_i) is found to be approximately directly dependent on the energy of the primary electron beam impinging on the surface (E_p) and inversely dependent on the square of the ionization energy of the bound electron (E_i) [24].

$$Q = \frac{2\pi e^2}{E_p E_i} \cdot b \cdot \ln\left(\frac{4E_p}{E_i\left[1.65 + 2.35\exp\left(1 - \frac{E_p}{E_i}\right)\right]} \right) \tag{3.9}$$

The maximum cross section is usually found to occur when $E_p \approx 3E_i$. The competition between the two relaxation processes, x-ray and Auger electron production, leads to a more complicated analysis in determining Auger electron yield. Theoretical yields for Auger electron and x-ray production assuming K type transitions are strongly dependent on the nuclear charge, Z; as it can be seen in equations 3.10 and 3.11.

$$Y_a = \frac{1}{1 + \beta \cdot Z^4} \tag{3.10}$$

$$Y_x = \frac{\beta \cdot Z^4}{1 + \beta \cdot Z^4} \tag{3.11}$$

β is a experimentally fit parameter. In a plot of yield versus atomic number, Auger electron yield dominates for light atoms and is close to unity from Li to Si [24]. The cross over point where X-ray production is as probable as Auger electron ejection occurs at Ge. This should not be interpreted that Auger is ineffective for elements heavier than Ge, since K level ionization does not represent the most probable Auger transitions for heavier atoms. Transitions involving L and M initial ionizations become more important with increasing atomic number. In addition, the density of states of the other two higher energy levels is also a factor in Auger transition intensity. These variables do not permit an easy theoretical determination of an atom's Auger sensitivity, as a result there exists tables of experimentally measured Auger cross-sections of all the elements at various primary energies.

The equipment needed to perform AES is an electron gun and an electron energy analyzer. On the PHI model 10-155 cylindrical mirror analyzer (CMA), the electron gun is integrated with the analyzer. The gun is coaxial to the long axis of the CMA and placed in the middle of the two cylinders. An electron beam is produced by heating a bent tungsten filament held at a negative 3 kV with respect to ground. The beam is focused to a spot of 1 mm in diameter. The CMA consists of two concentric cylinders. The inner cylinder is maintained at ground with the outer cylinder connected to a negative voltage, so when an electron enters through the entrance slit in the inner cylinder, it is guided toward the inner cylinder. The electric field allows only electrons with the correct velocity to enter

the exit slit and be measured as an amplified current by a channeltron. The ionization source produces a large slowly increasing background with the Auger peaks appearing as small peaks. This background is the result of the inelastically scattered incident electrons and their resulting secondary electrons. Differentiating this spectrum aids in the location of the individual Auger peaks; this is done in the analog mode by modulating the voltage on the outer cylinder with an amplitude of 2 V at a frequency of 7.0 kHz. Measuring the outcoming signal at the same frequency as the reference frequency applied to the outer cylinder through the use of a lock-in amplifier gives the differential of the Auger current with respect to time. The lock-in amplifier increases the Auger signal by averaging the differentiated signal by a time constant of 300 ms.

3.4 EXPERIMENTAL PROCEDURES

3.4.1 Single Crystal Preparation

Single metal crystal boules aligned to within 2° of the preferred crystal plane are available commercially. Although most suppliers provide a quality product, additional alignment is necessary before slicing the boule into individual single crystals. This process is started by first mounting the boule into the boule goniometer. This precision goniometer is then mounted to an optical rail on a real time Laue backscattering diffraction unit. The Laue diffraction method uses a non-monochromatic x-ray beam, so multiple Bragg peaks are seen. This method

is well suited in determining crystal orientation, because when the incident direction lies along a symmetry axis of the crystal, the pattern of the diffracted beams will have the same symmetry as the crystal [25]. If the beam intensities share the same symmetry as the crystal, then the crystal is aligned within 0.05° of the preferred axis of symmetry. The crystallinity of the boule is first checked to insure against the possibility of twinning within the crystal. This test is performed by scanning the x-ray beam across the diameter of the boule and watching for multiple 000 spots. Upon passing this test, the boule is aligned to with 0.5° of the crystallographic axis, then the crystal and goniometer are mounted onto a Electro-Discharge Machine (EDM) to slice the individual samples.

The individual slices are mounted onto a phasing goniometer to correct any misalignments that occurred during the slicing procedure [35]. The mounting surface of the goniometer is a milled stainless steel insert that can be either fixed in position (the diffraction position) by a rear mounted screw or allowed to float (the polishing position) on a spring behind the insert. The stainless steel insert housing is mounted on a set of gimbals in the front. In the rear, the housing is fixed in place with four screws. These screws allow for adjustment of the crystal's surface normal angle. The sides of the outer cylinder of the gonimeter is machined exactly perpendicular to the two ends. This criterion is the most important, since the polishing plane must be the same as the alignment plane. The alignment plane is given by the plane perpendicular to the side of the outer cylinder, because the goniometer is placed in a V-block to measure the Laue data.

The polishing plane is determined by the surface that contacts the polishing machinery, and this is the front end of the goniometer. After alignment, the crystal which is still mounted on the gonimeter is ground on 0000 emery grade paper until the surface is flat.

The crystal slice is then mounted in an epoxy in preparation for polishing. Polishing is performed with a brass wheel with a flat machined face mounted on a constant rpm motor. On this wheel assembly, a self-adhesive napless cloth is used as a carrier for the polishing compound which consists of size selected industrial diamonds suspended in an organic paste. If the experimenter was careful in dismounting the crystal from the phasing goniometer and grinding the surface flat, then the six micron polishing compound can be used to begin the coarse polishing. In order to minimize the polishing time, the grit size is slowly decreased from six to one to 0.25 microns. The last stage of polishing is the most crucial, since all metal samples are known to pit if left on the polishing wheel too long with the 0.25 micron abrasive. These pits leave the experimenter only one option—start the process over again with the six micron abrasive. One method in preventing pitting from occurring is to inspect the crystal constantly during the final polish and to stop the polishing when there exists a minimum of one micron scratches.

The final surface preparation is performed in vacuo. The crystal is sputtered for extended periods of time with high energy Ar^+ ions. The sputter is performed in an alternating sequence with short anneals. Sputtering removes the

damaged volume that resulted from the 0.25 micron final polish, and the anneal aids in creating large crystalline surface domains. These cycles of sputtering and annealing are repeated until a sharp diffraction pattern is measured by LEED.

3.4.2 Substrate Preparation

For freshly polished crystals, the cleaning procedure is more time consuming, but the same steps are used as for crystals that have been in vacuum before. The procedure is dependent on the material, although the common operations are sputtering with noble gas ions, chemical reduction or oxidation of contaminates and long anneals to repair the physical damage incurred by sputtering.

For Pt, the main surface impurity is carbon due to the metal's chemical activity. A majority of the carbon can be removed by annealing the crystal in 10^7 torr of O_2 to a temperature of 900°C for 2-3 min, thus oxidizing the carbon to CO and CO_2 for subsequent desorption. It is important not to anneal a Pt sample until a majority of the carbon has been oxidized, because at approximately 900°C, the carbon can form an ordered graphitic layer on the surface. This graphitic layer, which can be observed by LEED, does not react as effectively as the amorphous carbon to the oxidative treatments. To rid the surface of this graphitic contamination, multiple cycles of sputtering the surface with energetic Ar^+ ions followed by flashing the crystal in 10^7 torr of O_2 are performed until the carbon is eliminated as determined by AES. Sulfur, a common bulk impurity in Pt, can be

easily removed by sputtering. Long anneals in vacuum (thirty minutes to two hours) are usually required in order to have a sharp diffraction pattern.

Pd does not crack hydrocarbons as efficiently as Pt, so after the initial carbon has been oxidized, there is little need to perform multiple anneals in O_2. Since AES was the only method used in determining the cleanliness of the surface and the Pd 279 eV Auger peak overlaps with carbon's 272 eV peak, small amounts of carbon contamination could not be quantified The main contaminate is sulfur. Sulfur is a bulk impurity that surface segregates very readily. It can easily be sputtered away, but after annealing, the sulfur is present. Since the sulfur concentration in the bulk is orders of magnitude larger than the surface area, this problem will always exist. To circumvent this problem, it is necessary to deplete the surface volume of sulfur. One method is to reduce the sulfur by heating the crystal in an atmosphere of H_2. Great care is needed when performing this chemical treatment. One reason is the inherent danger in working with H_2 gas and the other reason is that Pd forms a hydride with a different unit cell density and lattice constant than Pd metal, so the crystallinity of the sample can be destroyed if the experimentalist is not familiar with the H_2-Pd phase diagram. Long anneals in vacuum are usually not necessary, because the cleaning procedure effectively forms large crystalline domains.

Rhodium's cleaning procedure followed that of palladium's with the exception of the caution during H_2 exposure.

3.4.3 Adsorbate Preparation

The $MgCl_2$ was purchased as powders from Sigma-Aldrich and stored under an argon atmosphere. Both were purchased with a purity of 99.999%. Single crystal NaCl and LiF were cleaved and crushed into a powder with a mortar and pestle. These powders were then out gassed by heating them to 350°C in vacuum for three hours.

3.4.4 Thin Film Growth

The ionic solids are vaporized with a Knudsen cell (K-cell) of standard design (Fig. 3.4). The ionic compounds are contained in a removable crucible. The crucible material is dependent on the chemical reactivity of the adsorbate being used at the time. A graphite crucible was used in the $MgCl_2$ experiments. This crucible was machined out a solid cylinder of graphite, then it was out gassed and sintered in a vacuum oven. For NaCl and LiF, a molybdenum crucible held the compound. This crucible change was in response to the increased temperature that was needed in vaporizing these alkali halides. The molybdenum's increased thermal conductivity allowed the deposition source to operate at a higher temperature without changing the power supply or heater design. Adequate temperatures were not achievable with the graphite crucible.

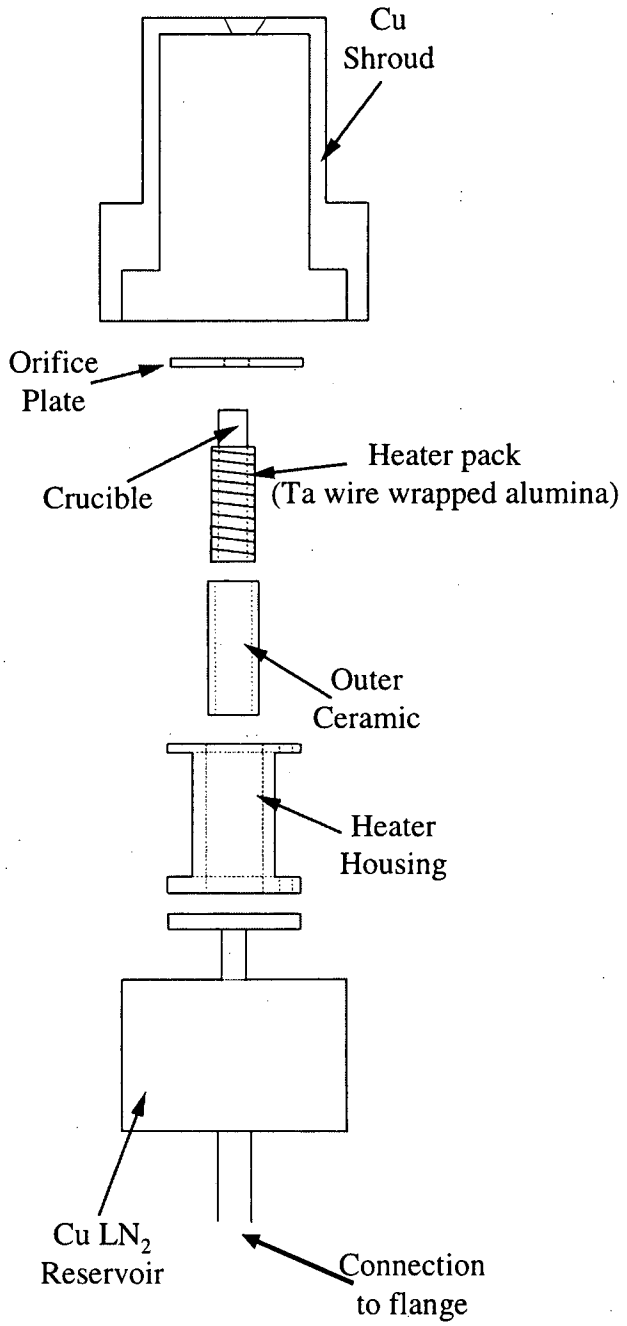

Fig. 3.4. Exploded side view of the Knudsen cell used in all the experiments

The crucible is housed in the removable furnace pack fabricated from high purity sintered alumina which has a double thread cut into the side to hold 0.2 in. tantalum wire. Surrounding the wire-alumina heater is a cylinder of high purity sintered alumina to electrically and thermally isolate the heater from the surrounding metal shroud. This furnace is brought up to temperature by resistively heating the tantalum wire. The temperature of the crucible is measured by a K-type thermocouple in contact with the closed end of the crucible. This assembly is then mounted in a stainless steel cylinder. In order to minimize the thermal contact with the whole apparatus, the furnace is supported on six 0-80 set screws within the stainless steel cylinder. These screws also allow for adjustment of the crucible so that it is inline with the orifice.

Finally, the entire assembly is surrounded by a copper shroud which is cooled by flowing liquid nitrogen (LN_2) through the rear of it. This cooling is needed to prevent the chamber walls from heating up and to getter the desorbed gases from the whole of the K-cell. Manufactured into the copper shroud is a 0.19 in. orifice which can be covered with a stainless steel shutter giving the user accurate control over the deposition time.

The temperature is maintained by a proportional-integral-derivative (PID) controller that feeds the required amount of current into the heater filament in response to the temperature. Power is limited by the controller with an on-off mode solid state relay. Limiting the heater power is allowed through the use of a

variable transformer integrated into the power supply. This adjustment is necessary, because of the PID controller's limited range.

The Knudsen cell is designed as to allow no binary collisions as the molecules leave the orifice in the molecular flow regime [36]. This lack of effluent molecule interaction allows the same vibrational and rotational energy of the molecules in the low pressure regime (in the UHV chamber) as that in the high pressure regime (inside the Knudsen cell).

Symmetric evaporation due to the strong ionic bonding of the metal halides was witnessed in the vapor effluent. The nonsymmetrical species seen these background subtracted mass spectra are due to cracking in the electron beam [37-39]. Previous work documents the existence of polymeric species in the vapor composition of the thermally evaporated alkali halides. It has been published that even at temperatures well above the ones used in these experiments that there was no thermal cracking of the metal halides.

In the absence of a quartz microbalance, the characterization of the source is done indirectly by measuring the adsorbed film thickness (d) by Auger signal attenuation (i_a) of the substrate. This reduction of Auger signal is modeled by the following equation [40-42].

$$i_a = i_0 \cdot \mathrm{Exp}\left(\frac{-d}{\lambda_0}\right) \qquad (3.12)$$

where i_0 is the Auger current of the clean substrate and λ_0 is the escape depth of the electron. For Pt, Pd and Rh, their characteristic Auger transitions lie within

the region of 100-800 eV, and this corresponds to film thickness maximum of 30 Å or 8-15 monolayers depending on the adsorbate's structure.

At the start of an investigation of a new adsorbate, a source temperature has to be found in which the deposition rate is large enough to grow a film before significant contamination of the substrate occurs, but also slow enough to allow an accurate measure of the deposition time. It can be seen from the Clausius-Clapeyron equation (equation 3.13) that the vapor of a material has a direct exponential dependence on temperature (T) and the enthalpy of sublimation (ΔH_{sub}), thus small changes in temperature greatly influences the vapor pressure.

$$\frac{P}{P_0} = \mathrm{Exp}\left(\frac{\Delta H_{sub}}{R \cdot T} + C\right) \qquad (3.13)$$

where P is the vapor pressure of the adsorbate, P_0 is the vapor pressure at standard state, R is the gas constant and C is a constant of integration. Adsorbed films of various thicknesses are produced by keeping the deposition time constant while increasing the K-cell temperature. These experiments give the response of the source with respect to the measured temperature which may differ from the actual temperature of the evaporated material because of less than perfect thermal conductivities of the source.

Once the source has been characterized, the desorption behavior of the adsorbate has to be quantified; this is done with TPD. The reason for determining the substrate-adsorbate interaction is that in all the experiments a heated substrate is used to exact additional control of film thickness and to anneal the growing

crystalline surface layer. In most experiments, the substrate temperature is held at the point where desorption occurs. This temperature is determined by the TPD spectra, but these spectra serve only as guide to the general temperature region. The experimental substrate temperature is usually below the one seen in TPD, because the desorption rate is inversely proportional to the adsorbate coverage. This effect is due to the formation of islands of finite size on the surface. Smaller islands of adsorbate are more easily desorbed than large islands, thus causing the desorption temperatures to shift to lower temperatures. The strong adsorbate-adsorbate interaction of the ionic solids amplify this phenomenon. A method used in finding the optimum substrate temperature begins by measuring film thicknesses with the source at its predetermined temperature and varying the crystal's surface temperature. The crystal temperature that produces a film of 20 Å is chosen for subsequent experiments.

As mentioned previously, annealing of the adsorbed film occurs during deposition due to the use of an elevated substrate temperature, but additional film annealing in vacuum is also performed. These post deposition anneals have proved invaluable in working with the alkali halide films. It has been theorized that the large crystalline domains grow at the expense of the smaller ones and that the smaller domains desorb into the vacuum system during these anneals.

Chapter 4

Previous Investigations of Alkali Halides

4.1 INTRODUCTION

The ionic solids created by the alkali halides behave so ideally that bulk structural and electronic characteristics are easily derived from elementary theories of ionic bonding [25]. This simplicity was the main reason why NaCl was among the first crystal structures solved by W. H. Bragg, since to a good approximation, the crystal can be visualized as rigid spheres stacked within the unit cell. Experimental confirmation of the validity of this liberal assumption is seen in the ions' electronic charge densities [25]. For the (100) face of NaCl, the ions possess spherical electronic charge distributions with small distortions caused by the ions' neighbors in the crystal. The cohesive energy of the alkali halides can, to a good approximation, be derived using only the interionic Coulomb interaction. This interaction which is proportional to the inverse of the interionic distance dominates over the fluctuating dipole interaction which has an inverse sixth power dependence on interionic spacing. Including additional terms into the crystal binding energy such as: 1. positive core-core repulsion 2. fluctuating dipole force between the ion cores 3. zero point vibrations of the lattice improves the theoretical cohesive energy by only 10% over the cohesive energy derived from the Coulomb interaction alone.

4.2 BULK SURFACE INVESTIGATIONS

One of the consequences of being such a well characterized solid is that it becomes the obvious choice in investigating phenomena that are not as well understood; this is the way that alkali halides entered the surface science literature. In the realm of surface science, alkali halides, specifically NaCl and LiF, were among the first materials in which a quantitative use of low energy electron diffraction (LEED) data was attempted to elucidate a surface structure, since they were deemed to be a good candidate for the conventional single scattering theory of electron diffraction [43,44]. The aforementioned spherical electron density of the alkali halides corresponds well to the muffin-tin model of the surface scattering potential. When using low Z number compounds, the probability of multiple scattering events is minimized as much as possible. These early attempts in the application of the kinematic diffraction theory further stressed the need for a fully dynamical scattering theory, since even for these "ideal" systems, additional empirical definitions were needed achieve a good correspondence between the experimental and theoretical intensity versus electron energy (I-V) curves. Since these previous studies used electron-based techniques to investigate the surface of bulk NaCl samples, the obvious problem of charge accumulation by the sample was always a factor, and it was also found that NaCl was subject to destructive electron stimulated desorption (ESD) of Cl neutrals

[45]. These two effects complicated an already difficult analysis and will be discussed in detail later in this chapter.

Alkali Halide	Surface layer Corrugation[a,b]	Second layer Corrugation[a,b]
LiF	4.84	-2.23
LiCl	20.77	-19.21
LiBr	23.53	-22.23
LiI	26.5	-25.45
NaF	0.81	-0.1
NaCl	6.69	-3.49
NaBr	9	-5.66
NaI	14.4	-11.63
KF	-2.05	1.16
KCl	2.16	-0.76
KBr	3.28	-1.44
KI	5.5	-3.01
RbF	-3.79	2.43
RbCl	0.81	-0.06
RbBr	1.83	-0.64
RbI	3.61	-1.8
CsF	-8.89	7.63

[a]In units of % interlayer spacing of the specific alkali halide compound
[b]A positive corrugation indicates that the anion lies above the cation

Table 4.1. Results from the shell model calculations performed by G. C. Benson and T. A. Claxton from reference [47].

4.3 (100) SURFACE RECONSTRUCTION

In addition to testing emerging quantitative LEED structural theories, the pursuit of alkali halide surface structure was also fuelled by the theoretical

prediction by Verwey that the (100) surface of alkali halide crystals possessed a significant distortion due to the alkali cations' movement towards the bulk with the halide anions maintaining their x-ray determined bulk-like positions [46]. The impetus for this reconstruction is the difference in polarizability of the individual ions coupled with the loss of coordination at the surface termination.

Verwey's initial model which allowed the surface atoms to relax due to these polarization differences was given an additional degree of sophistication by Benson and Claxton by including lower lying atomic planes to the calculation [47]. The model describes the cohesive interaction of the alkali halide ions in terms of the Coulombic interaction modified by the Born-Mayer potential which accounts for the core-core repulsions. The key ingredient to this model is the idea of ion polarizability. Rigorously, polarizability has contributions from the distortion of the ionic charge distribution about the ion center (atomic polarizability) and from distortions due to ionic displacements (displacement polarizability). Atomic polarizability is modeled by treating the ion as an electronic shell of charge $Z_i e$ and mass $Z_i m$ connected to a stationary positively charged ion core by a harmonic oscillator with a spring constant defined as $k = Z_i m\omega_0^2$, giving the following definition of atomic polarizability, α^{at} [25].

$$\alpha^{at} = \frac{Z_i e^2}{m\left(\omega_0^2 - \omega^2\right)} \tag{4.1}$$

where $Z_i e$ is the electronic shell charge, m is the electronic shell mass, ω_0 is the characteristic vibrational frequency of the electronic shell and ω is the vibrational frequency of the shell-core system.

Displacement polarizability, α^{dis}, is derived ignoring atomic polarizations (the rigid ion approximation) and modeling short range interionic forces such as electrostatic multipole moments and core-core repulsion as a restoring force to ion displacements, thus giving the same form of the equation as seen in atomic polarization [25].

$$\alpha^{dis} = \frac{e^2}{M(\varpi^2 - \omega^2)} \tag{4.2}$$

Where e is the electron charge, M is the reduced mass of the ion pair, ϖ is the lattice vibrational frequency and ω is the vibrational frequency of the displaced ions.

The results of the application of this model are tabulated in Table 4.1. From the results, it can be seen that the largest reconstruction occurs on the surface layer with the successive layers having less and less deviations from their bulk coplanar positions. All but KF and RbF have the cation below the anion in the surface level with the cation's and anion's positions being reversed in the second layer. Since this reconstruction is based on the differences of ion polarizability, trends tracking the separation with respect to the ion's polarizability show that the surface layer rumpling is directly related to the increase of anion polarizability, but inversely related to cation polarizability.

When the anion's and cation's polarizability are increased, there is a decrease in surface rumpling. The theorists maintain that only a qualitative conclusions should be made about the correlation between ion polarizability and surface structure. The reason for such caution is that the calculations did not use self-consistent constants.

Experimental confirmation of this surface layer corrugation prompted many innovations in working with insulating materials. The extreme sensitivity of alkali halide single crystals encouraged others to extend the previously mentioned calculations to include divalent compounds with the rocksalt structure, specifically MgO, which did not have ESD problems [48-52]. Additionally, the choice of MgO was prompted by its wide-spread use as a heterogeneous catalyst support. Charging was still a problem with MgO, because of its insulating property. Experiments which led to its structure determination used pulsed electron beams to discharge the surface. Another method widely used with nonconductive surfaces—the growth of thin epitaxial films of the insulator on a conductive substrate was performed by Henzler et al with NaCl to obtain spot profile LEED data.

4.4 REACTION TO ELECTRON BEAM IRRADIATION

Since traditional surface science techniques employ electrons, the accumulation of charge by insulators, such as alkali halides, has always hampered

the study of these materials. The effect of surface charging is further complicated by the alkali halides' ability to effectively emit secondary electrons as a means to alleviate the surface acquisition of a negative potential. The efficiency of the material's secondary electron emission in preventing charging is found to depend on the incident electron energy. At a constant surface temperature, there exists a cross-over voltage (V_p) where the total secondary electron emission yield is equal to unity, thus producing a stable LEED pattern [53]. If the incident electron beam energy falls below eV_p, then the sample surface charges down to the cathode potential, thus repelling the beam current towards the source. Restoration of a stable LEED pattern is not possible by simply raising the incident electron energy back to eVp; it can only be restored by flooding the surface with much more energetic electrons, approximately $3 \times eV_p$.

The cross-over voltage's magnitude has a inverse temperature dependence. There exist two theories on this temperature dependence. One theory states that an excited electron with an energy less than that of the band gap can either gain or lose energy by coupling with the longitudinal optical phonons of the solid [53]. Such an electron can diffuse about the crystal until it escapes to the vacuum level as a secondary electron or until it loses enough energy to be trapped by the surface potential barrier (on the order of 0.1 eV). The average energy loss per collision with the longitudinal optical phonons is governed by the following equation:

$$\alpha(T) = \frac{h\nu}{2\eta_T + 1} \tag{4.3}$$

$$\text{where } \eta_T = \frac{1}{\text{Exp}\left(\frac{h\nu}{kT}\right) - 1} \tag{4.4}$$

where ν is the phonon frequency, h is Plank's constant, k is Boltzmann's constant and T is the absolute temperature of the surface. $\alpha(T)$ decreases with increasing temperature, thus the incident electrons are less likely to lose energy to the lattice vibrations and be captured by the surface potential barrier.

An alternate theory to the decrease of the cross-over voltage (V_p) with increasing temperature is related to the electron stimulated desorption (ESD) process [54]. A consequence of the ESD process is that the surface becomes metallized by alkali metal. Metals have a secondary electron yield below the alkali halides, thus the change of surface composition from alkali halide to alkali metal affects the efficiency of secondary electron emission. Temperature comes into the equation when desorption of the newly formed metal is considered. At a low temperature, the electron beam is converting surface alkali halide to alkali metal at a constant rate. Since the metal is not as good a secondary electron producer as that of the alkali halide, the system charges down to the cathode potential. If the system is heated to the desorption temperature of the alkali metal, then metal desorption begins to compete with the metal production. When the desorption rate is balanced by or greater than that of the production rate of the alkali metal, the sample, now consisting of totally alkali halide begins to conduct

by secondary electron emission like an undamaged sample. Although both theories correspond to the experimental observations relating sample temperature to cross-over voltage, the metallization theory is further corroborated by scanning electron microscopy (SEM) data which shows island formation of alkali metal islands on the surface [55].

Electron stimulated desorption (ESD) of halogen neutrals and the surface enrichment of alkali metal was observed immediately by Prutton et al while doing the first LEED experiments on NaCl [56]. This extremely efficient process has been explained by Pooley and Hersh independently. The Pooley-Hersh model assumes that an electron incident on a defect free ionic crystal at low temperature creates an electron-hole pair in a halogen atom [57]. The lattice distorts as to shorten the halogen-halogen distance, so the hole produced during the ionization is shared between the two adjacent halogen atoms, thus forming a dihalide anion. The electron removed from the halogen during ionization remains bound to its associated hole via screened coulombic interactions, thus forming an excitonic doubly charged dihalide anion. This dihalide anion dissociates, after a finite amount of time, placing one neutral halogen atom in an interstitial lattice site and leaving the electron trapped in the negative ion vacancy, effectively forming an F-center. The interstitial halogen atom usually possess significant translation kinetic energy and momentum so that it is probable that this atom merges with a halide anion in the lattice forming an H-center which is a single valent dihalide atom interstitially located. This H-center is extremely mobile within the surface

region especially along the {110} directions. The annihilation of the H-center usually results in the desorption of a neutral halogen atom. The electron creating the immobile F-center usually merges with the adjacent alkali cation forming a neutral metal atom on the surface. Following is the Pooley-Hersh sequence for NaCl accompanied by a schematic of the process:

Excitation

$$Cl^- + Cl^- + \text{electron} \rightarrow Cl^- + Cl^{-*}$$

Divalent dihalide formation

$$Cl^- + Cl^{-*} \rightarrow Cl_2^{2-*}$$

Dihalide dissociation

$$Cl_2^{2-*} \rightarrow Cl^- + Cl_{interstit} + \text{electron} + \text{vancancy}$$

F-center production

$$\text{electron} + \text{vancancy} \rightarrow \text{F-center}$$

F-center annihilation

$$\text{F-center} + Na^+ \rightarrow Na$$

Movement of interstitial halogen

$$Cl_{interstit} + Cl^- \rightarrow Cl^- + Cl_{interstit}$$

H-center creation

$$Cl_{interstit} + Cl^- \rightarrow Cl^-_{2,interstit}$$

H-center annihilation

$$Cl^-_{2,interstit} \rightarrow Cl^- + Cl_{desorb}$$

Chapter 5

LEED Analysis of NaCl(100) Thin Films on Pd(100) and Pt(111)

5.1 INTRODUCTION

The investigation of NaCl(100) has spanned modern surface science literature from the 1960's to today [43,58,59]. The reason for this large body of work is not that it was interesting, but NaCl(100) was chosen because of its inertness, its ease of formation and its "simple" structure. Early experimentalists did not have ultra-high vacuum and the wealth of surface preparation methods of today, so it was necessary to find surfaces that fit these first two criteria. NaCl(100) was given the role as the test bed for many surface structural techniques, since it was believed that the surface was a simple truncation of the bulk structure. The NaCl(100) surface is easily formed by cleaving in vacuum or in an inert atmosphere, and once cleaved, it can easily be cleaned by heating it in vacuum to drive off the absorbed water. In addition to its experimental simplicity, the structure and electronic characteristics of NaCl(100) were believed to correspond well to simple theoretical treatments of the resulting low energy electron diffraction (LEED) data. Within the single scattering assumption, one of the first LEED structural analyses concluded that the distance between the surface and the second layer was expanded by 2.5% [43]; this result can not be considered

reliable, because such a simplistic model was employed.

The first experiments with NaCl demonstrated its instability under the electron beam [45]. Electron stimulated desorption (ESD) of Cl neutral were observed during these experiments. ESD and charging of the sample were beginning to show that NaCl may not be as elementary as once thought.

Currently, there is a renewed interest in this compound, since recent studies in the field of atmospheric chemistry have linked surface reactions between NaCl and common gaseous pollutants such as HNO_3, N_2O_5, NO_2 and $ClONO_2$ to the production of ozone reducing gas-phase Cl atoms [16-20].

In this chapter, which is based on reference 58, the NaCl film growth parameters along with its desorption characteristics from Pd(100) and Pt(111) will be discussed in full. The treatment of the LEED intensity data and the resulting structure analysis will conclude the chapter.

5.2 EXPERIMENTAL

5.2.1 Preparation of the Pd(100) and Pt(111) Substrates

All experiments were performed in a stainless steel ultra high vacuum (UHV) chamber, with a base pressure of $<5.0\times10^{-10}$ Torr, equipped with a PHI model 15-155 cylindrical mirror analyzer with an on-axis electron gun for Auger electron spectroscopy (AES), and a UTI 100C quadrupole mass analyzer for residual gas analysis and temperature programmed desorption (TPD). The

Pd(100) and Pt(111) oriented crystals were prepared from commercially available boules with standard metallurgical methods, thus yielding substrates (8 mm in diameter and 1 mm thick) aligned within 0.5° of the preferred crystallographic plane. These crystals were spot welded to an off axis manipulator with capabilities for electron bombardment heating to 1300 K from a rear mounted W filament and cooling to 110 K from an attached liquid nitrogen reservoir. The temperature was monitored with a chromel-alumel thermocouple spot welded to the substrate's back face. Major contaminants, as measured by AES, were carbon and sulfur. Carbon was removed by repeated oxidative annealings at a surface temperature of 1100 K in 5.0×10^{-8} Torr of O_2, and sulfur through the use of multiple cycles of 2 kV Ar^+ sputtering. Subsequent crystal annealing (2-3 hours) in vacuum provided optimum LEED patterns for both substrates.

5.2.2 The LEED Experiment

Omicron Spectaleed electronics and optics provided the means for the visualization of the LEED patterns. A Dage-MTI intensified camera in accompaniment with a Matrox video capture card was used to record the LEED images for subsequent I-V extraction and to signal average over multiple exposures. By not extracting I-V curves while obtaining the LEED data, a rapid acquisition of a full data set in under 20 minutes of this electron beam sensitive overlayer could be accomplished. LEED intensity data collection followed a standard procedure [32] with the exception of a lower beam current (1.0 μA), to minimize electron beam damage to the overlayer. LEED data were collected at

normal incidence with a crystal temperature of ≈115 K in 2 eV increments over a range of 30-350 eV for the NaCl multilayer on Pd(100) and 72-270 eV for the NaCl/Pt(111) system. To insure normal incidence, symmetric beams were compared to confirm that the changes in the I-V curve's minima and maxima were less than or equal to 2 eV. As a check to see if the impinging electron beam caused significant damage to the ordered NaCl multilayer over the course of the data collection, data sets for both the NaCl/Pt(111) and NaCl/Pd(100) systems were taken while both increasing and decreasing the energy. It was found that peak positions deviated less than 2 eV between sets, thus providing quantitative evidence that the ordered structure largely remained intact during the data acquisition time period. Although the electron beam damage did not compromise the long range order of the multilayer, the detrimental effect of the beam did appear in the diffraction spot intensities, which are more sensitive to surface degradation. The result of the intensity changes is seen as a difference in relative beam intensities between a data set taken while increasing electron energy and one taken while decreasing the energy. In the I-V curves whose energy range exceeds 150 eV, the decrease of intensity with increased beam exposure caused an intensity change of 50-70% in the final maxima collected. Symmetrically equivalent beams from both substrates were averaged, thus giving seven symmetry inequivalent beams with a total range of 1274 eV to be compared with theory.

5.2.3 Deposition of NaCl Single Crystal Thin Films

The NaCl overlayer was grown by exposing a metal crystal with a surface temperature ~600 K to a flux of NaCl vapor emitted from a heated effusion cell, using a tungsten crucible, for 20 minutes. A full description of the source can be found in a chapter five. The ability of this source to produce a pure molecular flux of NaCl can be seen in the mass spectrum of the vapor flux, Figure 5.1. This spectrum is the result of subtracting out the residual gas spectrum of the chamber when the source is off from the mass spectrum taken while the source is at its operating temperature of 803 K. The features from this spectrum can be identified as $Na_2{}^{35}Cl$ and $Na_2{}^{37}Cl$ at 81-83 amu, $Na^{35}Cl$ and $Na^{37}Cl$ at 58-60 amu, ^{35}Cl and ^{37}Cl at 35-37 amu, Na at 23 amu and some residual CO at 28 amu. Based on the thermodynamic stability of the gas phase NaCl molecule, it was determined that the Na^+ and Cl^+ peaks are the result of fragmentation of the molecules and dimers in the ionizer and not products from the deposition source [37].

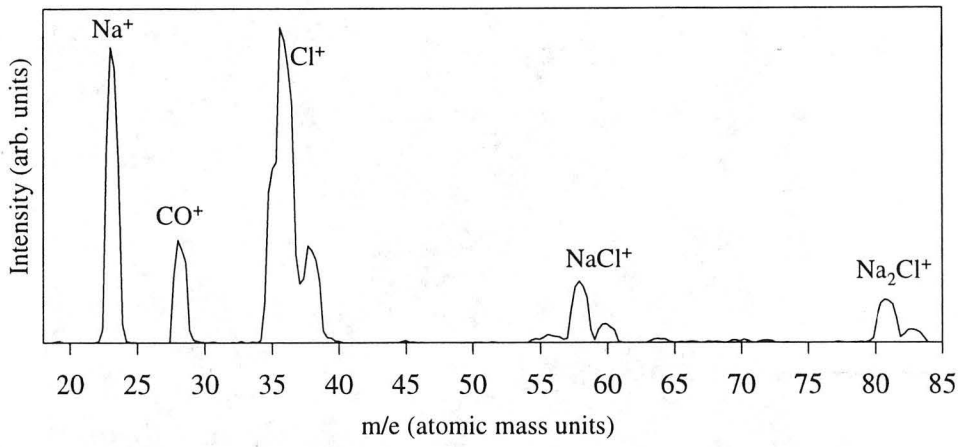

Fig. 5.1. Background subtracted mass spectrum of the source effluent with the source operating at 803 K.

5.3 RESULTS AND DISCUSSION

5.3.1 Condensation, Ordering and Desorption Characteristics of NaCl Films

The method of ordering the adsorbed ionic thin film has been discussed in detail in chapter three. The important element of this method is the use of a heated substrate, because at low substrate temperatures (298 K and below) NaCl resisted ordering on either substrate. The result of such an exposure, as seen by LEED, was the disappearance of the (1×1) pattern of the metal substrate because of the adsorption of a thick disordered layer of NaCl.

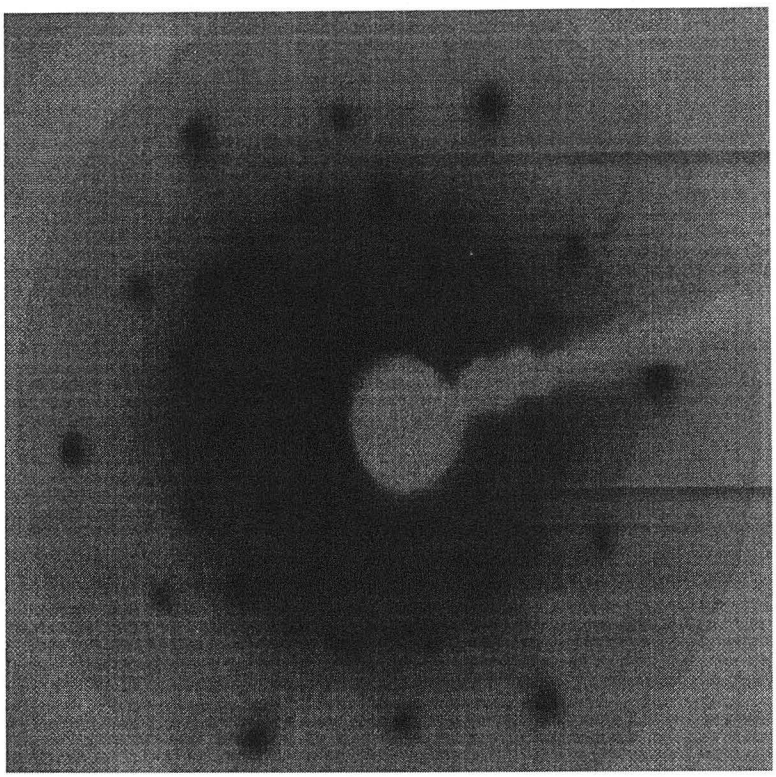

Fig. 5.2. LEED photo taken at an incidence energy of 66 eV of the Pt(111)-c(4 x 2)-CO surface structure with an adsorbed film of rotationally disordered NaCl appearing as a diffuse ring of intensity.

It was found that to counteract the rapid condensation of the adsorbate, it was convenient to heat the substrate to a temperature at which there is significant desorption. This method serves three purposes: 1. Limiting the film thickness by empirically finding the balance between the NaCl adsorption and desorption rates 2. Annealing the film at the elevated surface temperature 3. Desorbing CO, a background gas, to maintain surface cleanliness. CO adsorption was the main hurdle in exacting ordering on the substrate. Illustrated in Fig. 5.2, CO forms a well ordered, chemisorbed Pt(111)-c(4 × 2)-CO pattern [60]. This adsorbed CO

layer forces the NaCl to be rotationally disordered as evidenced by the ring of diffuse intensity just inside the Pt(111) 1,0 beams. With the application of this procedure, NaCl was successfully ordered on Pd(100) and Pt(111) by exposing the substrate, held at a temperature on the edge of the multilayer desorption peak, to the NaCl vapor. Additional annealing to higher temperatures was then performed to induce further ordering of the film and to prepare lower coverage structures.

The first step in finding the optimum substrate temperature for deposition was to collect temperature programmed desorption (TPD) spectra for both the NaCl/Pt(111) and NaCl/Pd(100) systems. Figure 5.3 shows the desorption profile of the $Na^{35}Cl$ and $Na^{37}Cl$ parent peak, m/e=58-60, adsorbed on Pt(111) and Pd(100). The lone feature exhibits an exponentially rising initial rate with a sharp falling edge. Such a profile is indicative of multilayer desorption. A leading edge analysis of the data (Fig. 5.3 inset) was performed for the NaCl/Pd(100) system with the assumption of zero order kinetics [33]. This results in an estimate for the activation energy for desorption of 211 kJ/mol which compares quite favorably to the heat of sublimation for NaCl, 200 kJ/mol [61]. Additional TPD spectral features were not observed even at lower coverages of the adsorbate.

An examination of the TPD spectra can give an idea of the growth mode of the adsorbed film. Illustrated in Fig. 5.3 is the shift of the desorption on-set temperature as a function of coverage. This temperature shift is due to the formation of islands of finite size [34]. The shift to a lower desorption on-set

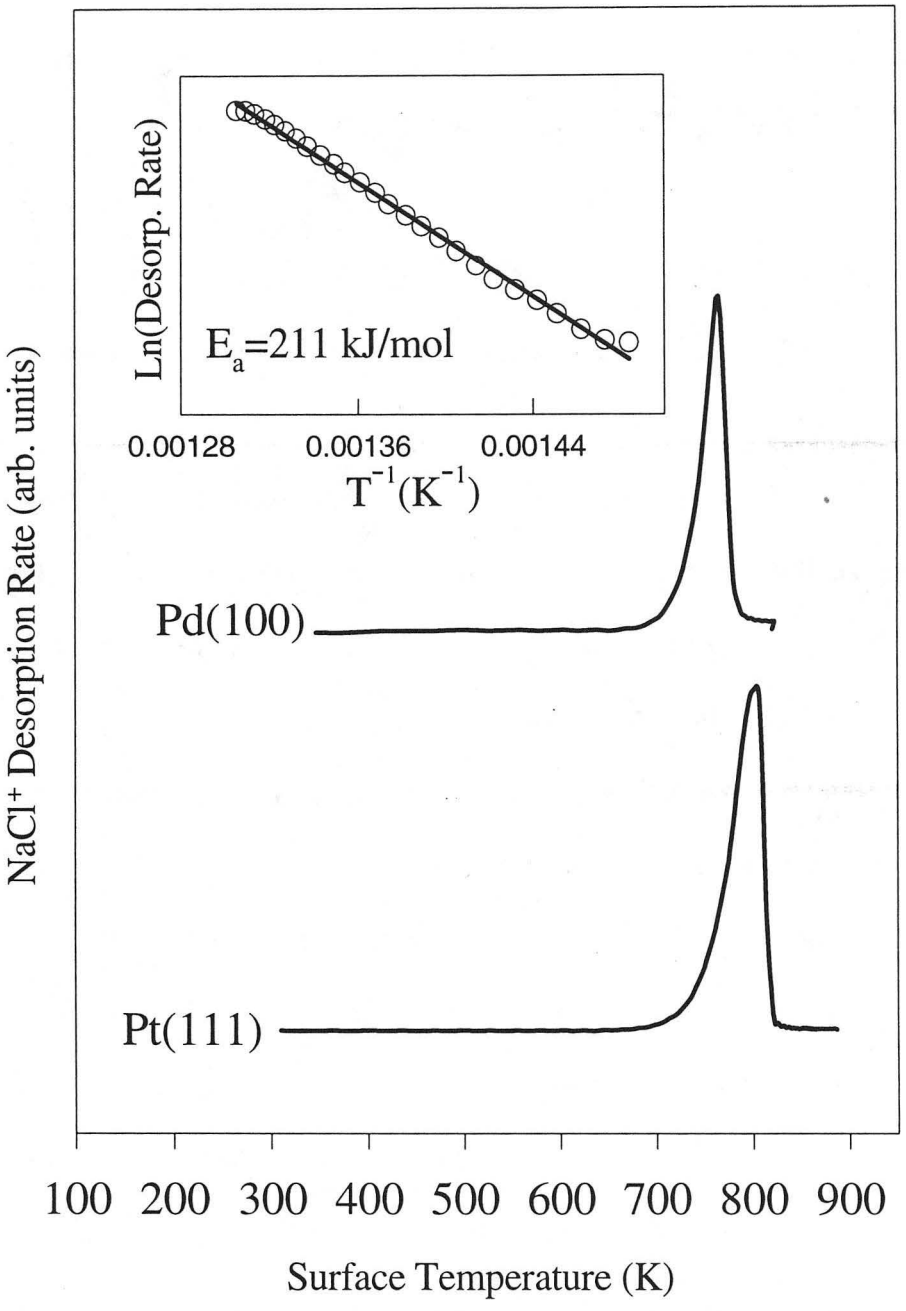

Fig. 5.3. Temperature programmed desorption profiles of multilayer NaCl films adsorbed on Pt(111) and Pd(100). The additional graph inset in the top left illustrates the results of the leading edge analysis of the feature seen in the Pd(100) TPD which yields an activation energy for desorption of 211 kJ/mol. The open circles represent the data and the solid line, the linear regression. It should be noted that a smoothing of the data was performed to filter out an oscillation which resulted from scanning over the m/e range of 58-60.

temperature is due to the fact that atoms on the edge of an island has fewer nearest neighbors than in the bulk, so it desorbs more easily than bulk island, therefore the desorption on-set temperature shifts to lower temperatures with decreasing coverage.

5.3.2 LEED Observations of NaCl Overlayers on Pd(100) and Pt(111)

5.3.2.1 NaCl/Pd(100)

Exposing the Pd(100) crystal, which provides a complementary lattice match with the NaCl(100) surface, with a temperature of 675 K for 20 min. to the effusion cell operating at 807 K produces a multilayer NaCl LEED pattern, which is represented along with the clean substrate pattern in Figure 5.4, a and b respectively. The square diffraction pattern of the multilayer film in conjunction with the lattice constant, determined from the pattern, of 4.0 Å, confirm the identity of the adlayer-- NaCl with the (100) orientation. Closer examination of the multilayer NaCl pattern and the clean substrate pattern, which resulted by desorbing the NaCl while maintaining the same crystal position in front of the LEED, reveals that the unit cell vectors of the multilayer are rotated by 45° with respect to the underlying Pd(100) unit cell vectors. This orientation of the adsorbed layer with respect to the substrate is driven by the near 1:1 lattice match (within 2.5%) when the NaCl film grows along the [010] type surface directions, i.e. along the diagonal of the Pd(100) primitive surface unit cell. Such a match does not present itself if the film grows along [011] type surface directions, i.e.

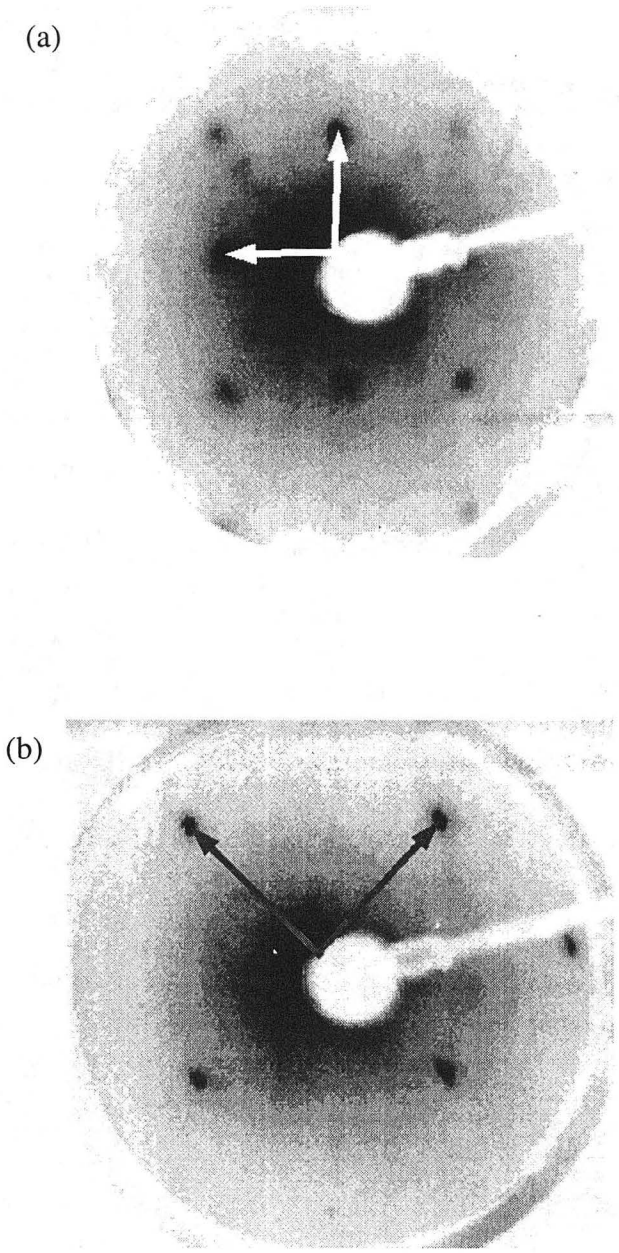

Fig. 5.4. LEED patterns for (a) NaCl(100)-(1x1) on Pd(100) and for (b) a clean Pd(100)-(1x1) surface after desorbing the NaCl overlayer, showing that the overlayer grows along the diagonal of the Pd(100) unit cell. Both images were recorded at the same sample position and incident energy of 65 eV and are plotted with negative contrast for clarity.

along the Pd(100) primitive surface unit cell vectors. Film thickness was estimated to be >15 Å as indicated by the absence of the substrate spots from the LEED pattern in the energy range, 30-350 eV, used for data collection.

5.3.2.2 NaCl/Pt(111)

To determine how the chemical identity of the substrate will affect the ordering of the NaCl films, Pt was chosen as the next substrate, since there was a minimal change in the lattice constant with respect to Pd(100). Since the clean Pt(100) surface reconstructs and would create complications, we chose to use Pt(111) as the second substrate.

Two substrate preparations provided different LEED results for the adsorption of NaCl on Pt(111). For all the NaCl films on Pt(111), the NaCl source temperature was held at 807 K for a 20 min. exposure. The first pattern, figure 5.5, was produced by keeping the substrate temperature at a constant 630 K during the deposition. The pattern consists of two rings of twelve spots that result from the existence of three domains of NaCl(100) rotated by 120° relative to one another, where the first ring of spots is formed from the (1,0) and (0,1) beams of their respective domains, and the outer ring from the (1,1) beams. These isoenergetic domains result from the difference in symmetry of the hexagonal substrate and the square overlayer. A similar pattern has been seen previously for NaCl on Ge(111), but at an annealing temperature 130 K lower and with more rotational disorder than comparable patterns of NaCl on Pt(111) [59].

(a)

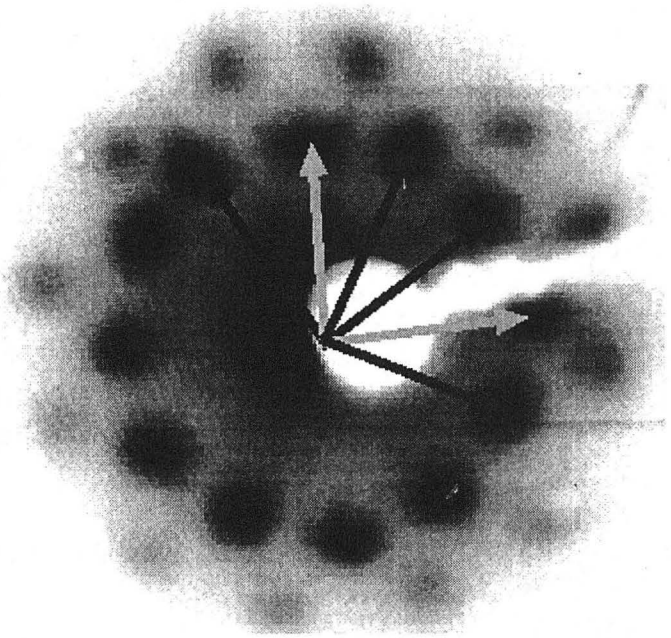

(b)

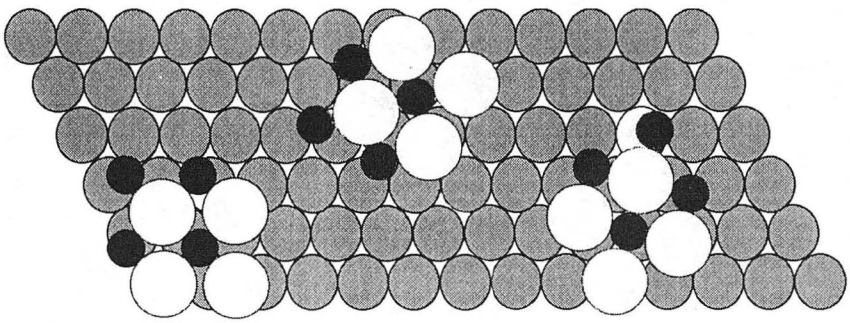

Fig. 5.5. (a) LEED pattern of a multilayer NaCl film grown on Pt(111), recorded at an incident electron energy of 63 eV, illustrating the three rotational crystalline domains. (b) Schematic of the possible real space orientation of the NaCl unit cells as a result of the symmetry difference between the substrate and the adsorbate.

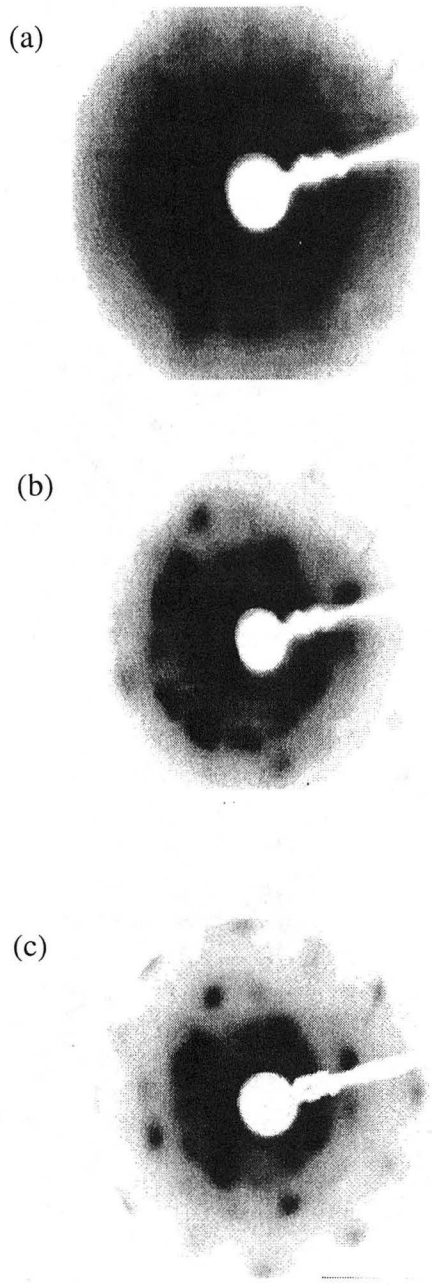

Fig. 5.6. (a) LEED pattern resulting from the adsorption of a multilayer NaCl film on a substrate heated to 703 K during deposition. The pattern was recorded at an incident electron energy of 60 eV. (b) LEED pattern of the film seen in (a) after a one minute anneal at a surface temperature of 708 K at an incident energy of 60 eV, showing how heating drives the film to become less rotationally disordered. (c) LEED image of the same film after annealing it at a surface temperature of 748 K where only one domain exists. An incident energy of 80 eV was used.

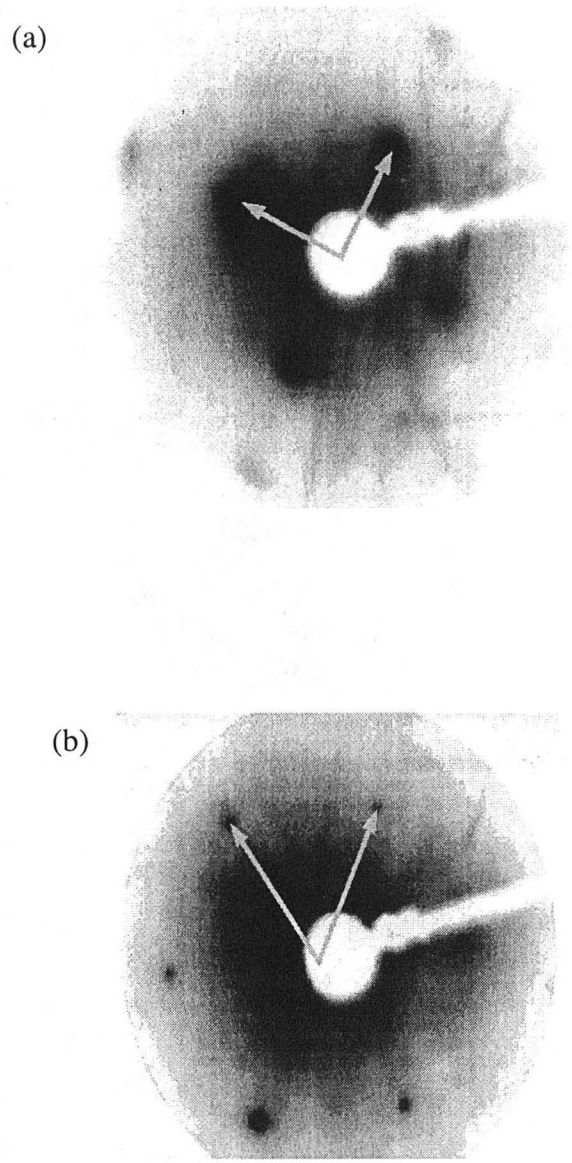

Fig. 5.7. Comparison of the LEED pattern of (a) a NaCl multilayer on Pt(111)recorded at an incident energy of 84 eV and (b) clean Pt(111) recorded at an incident energy of 85 eV to show the relative orientation of the overlayer to the substrate.

The second pattern, figure 5.6(a), was obtained by first maintaining a constant substrate temperature of 703 K. This diffraction pattern can be described as a ring of nonuniform intensity interspersed with discrete LEED spots, but, as documented in figures 5.6(a)-(c), subsequent heating to 750 K in vacuum orders the pattern to a single domain of NaCl(100). The relative orientation of the overlayer to the substrate can be witnessed through the desorption of the multilayer film, thus producing the underlying Pt(111) (1×1) pattern. Figure 5.7 shows that one unit cell vector of the overlayer (figure 5.7(a)) lies parallel to one of the substrate's (figure 5.7(b)) unit cell vectors. The resulting ordering of the film to one domain through desorption and/or diffusion clearly shows the very dynamic environment which the film experiences at temperatures close to the substrate's deposition temperature.

The lattice constant and/or the chemical identity appear to affect the ordering characteristics of the adsorbed NaCl film, since on Ge(111), no ordering of the NaCl overlayer was observed at substrate temperatures above 150 K. Instead, results indicated that a faceted NaCl(111) film grows on Ge(111) at these temperatures [59]. As with the multilayer film on Pd(100), film thicknesses of >15 Å were estimated from the absence of substrate spots from the LEED data in the measured energy range, 72-270 eV.

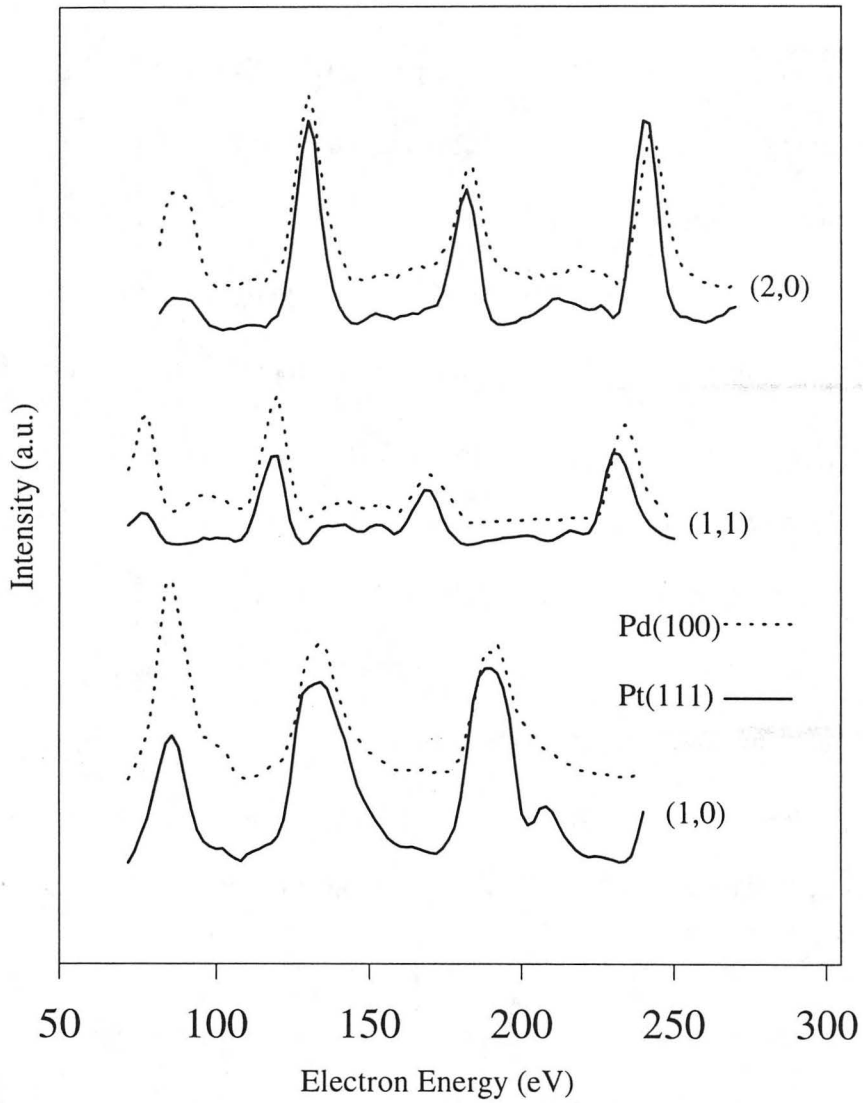

Fig. 5.8. Comparison of selected I-V curves from multilayer NaCl films on Pt(111), solid lines, and Pd(100), dashed lines. The curves' intensities were approximately normalized to ease comparison.

3.2.3 Comparison of LEED Data from NaCl(100) Grown on Pt(111) and Pd(100)

A visual inspection of the LEED patterns provided the initial proof that the structures of the multilayer NaCl films on Pt(111) and Pd(100) were the same within the measured energy range. Estimates for the unit cell dimensions, 4.2 Å for the film on Pt(111) and 4.0 Å for the film on Pd(100), and the four fold symmetry of both patterns provided the needed evidence. Additional proof can be seen in the direct comparison of the LEED intensity versus electron energy (I-V) data. Figure 5.8 shows a subset of I-V curves from the films grown on Pd(100) and Pt(111). These multilayer NaCl I-V curves possess the same maxima and minima, within the experimental increment of 2 eV, with some experimental variations, thus corroborating the proposition that the NaCl film has the same structure on both substrates to a depth sampled by the low energy electrons. An obvious deviation between he I-V curves is seen in the 1,0 beam where the 210 eV feature is a distinct peak in the Pt(111) data, but only appears as a shoulder on the Pd(100) data. The reason for this difference is the orientation of the sample with respect to the incident electron beam. It has been observed that the I-V peak positions are stationary within a sample alignment difference of ±0.5°, but peak shape, especially for low intensity multiple scattering features, has a strong dependence on the incident angle. The most compelling and quantitative evidence for the similarity of the two multilayer films will be found in the optimized structures that result from the quantitative LEED analysis of the individual data sets.

5.4 LEED THEORY

The analysis of the I-V curves was begun by the generation of a set of phase shifts up to l_{max}=9 for neutral Na and Cl using a potential derived under the muffin-tin approximation for the unreconstructed bulk NaCl(100) lattice with the Barbieri/Van Hove phase shift package. Ionic phase shifts were not considered, based on previous work with iron oxides [13] which indicated that they introduced no significant changes in either the final structure or the R-factor at our energies. Inelastic scattering effects which limit the penetration depth of the incoming electrons were modeled by the imaginary part of the inner potential, here being 5.35 eV. Thermal effects were represented by augmenting the phase shifts by a Debye-Waller factor.

The LEED calculations were performed with the Barbieri/Van Hove symmetrized automated tensor LEED (TLEED) package [6,7,62,9]. Each layer in the (100) face of bulk-like NaCl consists of a coplanar array of alternating Cl anions and Na cations. Each Cl-Na layer was defined as a composite layer. Multiple scattering within these composite layers were treated exactly via the Beeby inversion scheme. To describe the structure, five of these composite layers were used; two defining the surface region where relaxations were allowed, and three defining the unrefined bulk. Scattering between pairs of composite layers was modeled with the renormalized forward scattering approximation [2].

For structural refinement, the tensor LEED approximation in combination with the Powell optimization scheme was applied. For all optimized structures, the final structure was defined as a new reference structure and the calculation was repeated, as a check on the approximation. The R-factor comparing theory and experiment and the error bars corresponding to the coordinates perpendicular to the surface were calculated with Pendry's formula [29].

5.5 SURFACE STRUCTURAL ANALYSIS

The square symmetry of the LEED pattern eliminated the other possible orientations of NaCl, such as NaCl(110) which has rectangular symmetry and NaCl(111) which has hexagonal symmetry. The estimate for the unit cell dimension further narrowed the choice of the initial trial structures to the NaCl(100) face and modifications thereof.

The first trial structure was the ideally terminated, stoichiometric NaCl(100) surface whose lattice parameter was defined as the x-ray determined bulk value, 3.99 Å, [63]. In the TLEED calculation, the only structural parameters refined were the atomic positions of the Na and Cl in the topmost two layers, while assuming the preservation of the symmetry of the original structure in the revised structure. The muffin tin zero was the only nonstructural parameter refined. The automated TLEED calculation was directed by the optimization of the Pendry R-factor (R_P), which also represents the figure of merit for the refined

models. This trial structure refined down to an R_P of 0.17. Additional optimization of this model included varying the Debye temperature of the surface layer to investigate possible deviations from the bulk Debye temperature of 321 K used in the initial calculation [25]. It was found that a Θ_{Na}=270 K and Θ_{Na}=300 K improved R_P by 0.004 with no effect on the structural parameters. Figure 5.9 compares the theoretical I-V curves, which resulted from this last stage of refinement, to the experimental curves. The final structure with an R_P=0.16 described in Table 5.1 and illustrated in Figure 5.10 represents the structure solution for the NaCl(100) on Pd(100) and Pt(111).

The largest deviations from the bulk structure occurred in the surface layer, where the Na cations, which in the bulk would be coplanar with the Cl anions, relaxed towards the bulk and introduced a surface layer corrugation of 0.12±0.03 Å, increasing the exposure of the Cl anions at the surface. This movement of the surface Na cations was not followed by a concomitant relaxation of the Cl anions in the second layer to preserve a bulk like interlayer spacing between the surface and second layer. The $d(Cl_2\text{-}Na_1)$ distance, where the indices number the layers, was actually reduced to 2.72±0.03 Å from the bulk value of 2.82 Å.

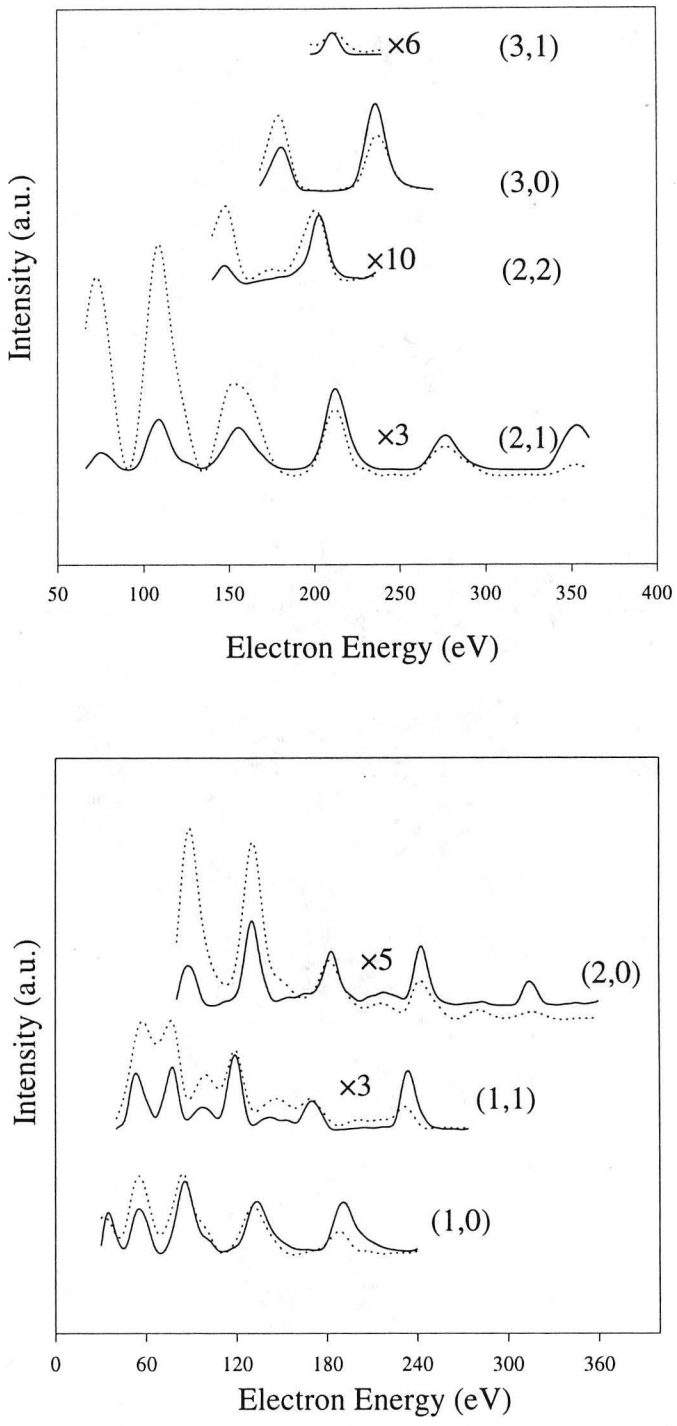

Fig. 5.9. Comparison of the theoretical (dashed lines) and the experimental (solid lines) I-V curves of the fully optimized NaCl(100) structure. All the beams used in the calculations are presented here.

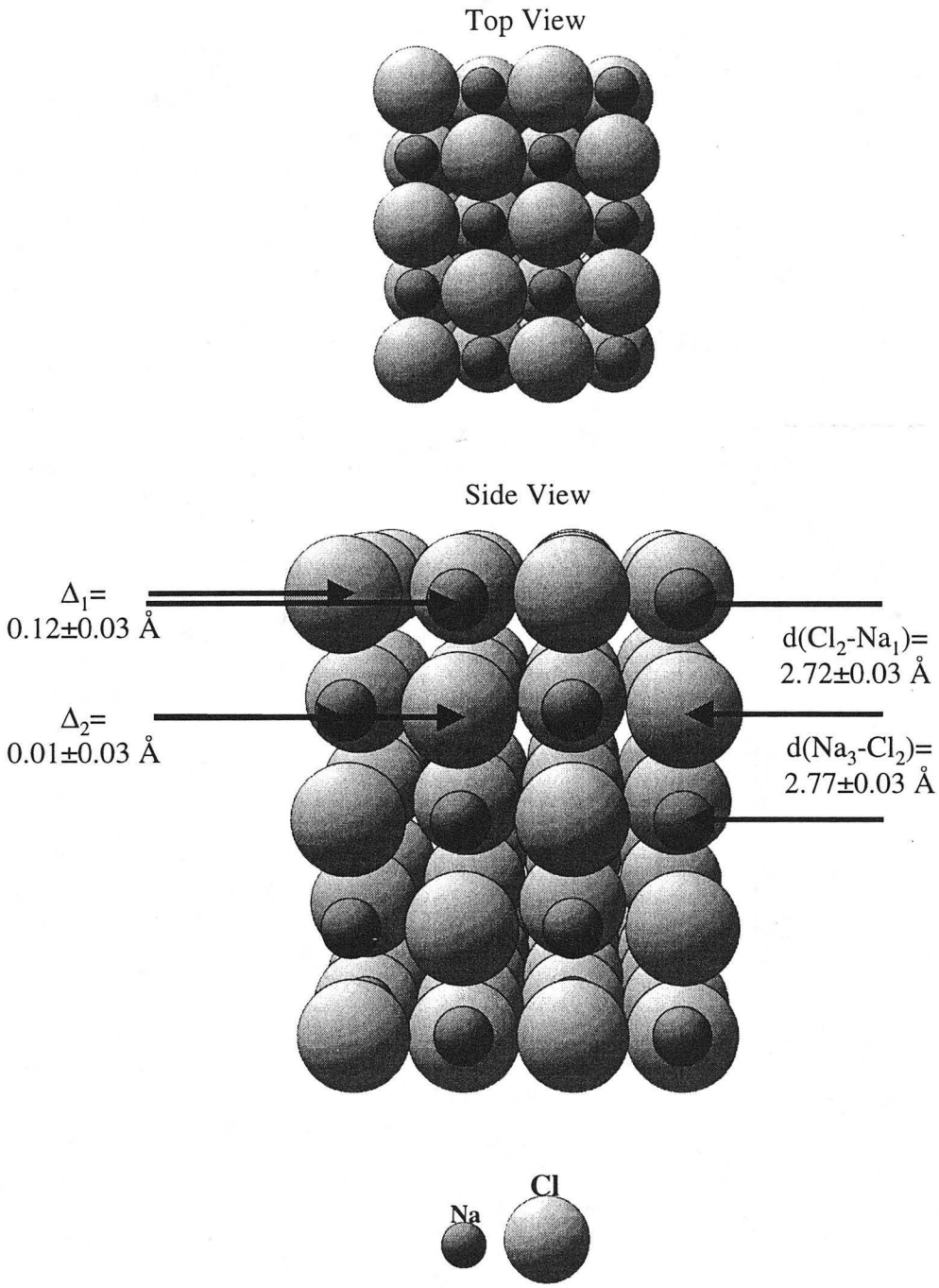

Fig. 5.10. Top view (top) and side view (bottom) of the optimized NaCl(100) surface grown on Pd(100) and Pt(111) (the surface termination is on top); the ionic radii were drawn reduced by 20% for clarity. The values of the interlayer and intralayer spacings in the refined region are shown. The bulk spacings are $\Delta_1=\Delta_2=0.00$ Å and $d(Cl_2\text{-}Na_1) = d(Na_3\text{-}Cl_2)=2.82$ Å.

Region[a]	Chemical Identity	Atom Number	Site Occupation	X^b (Å)	Y^b (Å)	$D_Z \pm \varepsilon_Z$ [c,d] (Å)
interface	Cl_1	1	1	0	0	0
interface	Na_1	2	1	2.82	0	0.12±0.03
interface	Cl_2	3	1	2.82	0	2.72±0.03
interface	Na_2	4	1	0	0	0.01±0.03
bulk	Cl_3	5	1	0	0	2.77±0.03
bulk	Na_3	6	1	2.82	0	0
bulk	Na	7	1	0	0	2.82
bulk	Cl	8	1	2.82	0	0
bulk	Cl	9	1	0	0	2.82
bulk	Na	10	1	2.82	0	0

[a]The interface region refers to the atoms at the vacuum-solid interface that were allowed to be refined in the calculation.
[b]Absolute lateral positions of the atoms are given in two-dimensional Cartesian coordinates.
[c]The provided error bars quantify the theoretical uncertainties of the refined parameters. The absence of error bars indicates that the value was not refined in the calculation, but held constant at its bulk value
[d]The perpendicular lattice positions are defined relative to the previous atom's position. The first atom listed represents the surface termination, and a positive D_Z value indicates a displacement towards the bulk.

Table 5.1. Full description of the refined NaCl(100) structure. The subscripts on the atom labels correspond to the subscripts used in the text and Fig. 5.10.

The separation between these two ions is now less than the touching distance, 2.76 Å, between adjacent Na^+ and Cl^- in the bulk, but since there is also a loss of coordination at the surface termination, a decrease of the ionic radii is to be expected.

No detectable buckling of the anions and cations was found in the second

layer where the intralayer spacing was Δ_2=0.01±0.03 Å. Similarly to d(Cl_2-Na_1), the second interlayer spacing, d(Na_3-Cl_2), was compressed from the bulk value, 2.82 Å, to 2.77±0.03 Å, but unlike d(Cl_2-Na_1), this spacing can accommodate the close packing of bulk-like ions.

Since the bulk value of the lattice constant is not consistent with a close packing of the ions with the published values of their ionic radii [64], it was decided that another reasonable trial structure can be made by shrinking the unit cell from a lattice constant of 3.99 Å to 3.90 Å. The same structural and nonstructural parameters were refined in this model as in the previous one. This model refined down to a chemically reasonable structure albeit with a higher R_P of 0.19. Similar shifts found in the structural solution described above were also present here, such as the displacement of the Na towards the bulk and the lack of any significant shifts below the surface layer. The main difference between this structure and the previous was found in the first interlayer spacing, more specifically d(Cl_2-Na_1). In the compressed lattice model, the d(Cl_2-Na_1) was found to be 2.67 Å which implies there has to be a 3.3% contraction of the ionic radii which is over twice as large as is needed in our first model.

By splitting up the combined data set used in the previous calculations and performing a fully dynamical tensor LEED analysis on the NaCl/Pd(100) and NaCl/Pt(111) data sets individually, the similarity of the multilayer film structure can be fully quantified. This separation reduces the cumulative energy range to 1100 eV for Pd(100) and 1004 eV for Pt(111), but these ranges provide adequate

information for analysis. The initial trial structure for both calculations was the ideally terminated stoichiometric NaCl(100) surface with the bulk unit cell dimension of 3.99 Å --the same initial structure which resulted in the structural solution for the combined data set. As with the previous analyses, the same structural and nonstructural parameters were refined with the exception of the Debye temperatures.

	Δ_1 (Å)	Δ_2 (Å)	d(Cl_2-Na_1) (Å)	d(Na_3-Cl_2) (Å)
NaCl/Pd(100)	0.12±0.03	0.003±0.03	2.73±0.03	2.81±0.06
NaCl/Pt(111)	0.12±0.04	0.01±0.04	2.74±0.05	2.83±0.06
NaCl/Pd(100) and Pt(111)	0.12±0.03	0.01±0.03	2.72±0.03	2.77±0.03

Table 5.2. Comparison of the values for the refined intralayer and interlayer spacings determined for all three data sets: NaCl on Pd(100), NaCl on Pt(111) and the combined Pd(100) and Pt(111) data set. The labels correspond the regions discussed in the text and illustrated in Figure 5.10.

Both data sets converged on optimized structures with R-factors of 0.16 for the Pd(100) data and 0.21 for the Pt(111) data. Although possessing different R-factors, all the resulting structures from the Pd(100), Pt(111) and the combined data set TLEED calculations have the same value for the two intralayer spacings (Δ_1 and Δ_2) and first interlayer spacing, d(Cl_2-Na_1), within the statistical error bars (Table 5.2). The largest structural difference between the data sets was seen in the value for the second interlayer spacing, d(Na_3-Cl_2), but these values are within one standard deviation of one another. The difference in R-factor between the Pd(100) and Pt(111) data sets is primarily due to experimental variations which

resulted from obtaining these data from two separate experiments.

5.6 SUMMARY AND CONCLUSIONS

NaCl has been successfully ordered in its (100) orientation on Pt(111) and Pd(100). The chemical identity of the substrate did not affect the film growth characteristics, but the underlying substrate symmetry had an influence on the azimuthal film orientation: in the case of Pt(111), the overlayer grew along one of the unit cell vectors of the substrate, but for Pd(100), which has a lattice constant within 1% of Pt(111), the film's unit cell vectors were rotated by 45° from the substrate's. Although there was an observable difference in the film growth between the different substrates, the comparison of the optimized structures which resulted from the LEED I-V analysis of the data taken from both substrates confirm that the multilayer films have the same surface structure to the depth sampled by the low energy electrons. Desorption characteristics are also shared by the two substrates, evidenced by the TPD curves whose only feature was a zero order multilayer desorption peak.

Complete LEED data sets were acquired from both substrates, and a fully dynamical LEED calculation was performed to determine the structure. Deviations from the bulk NaCl(100) atomic positions were a 3. 5% and 1.8% compressions of the first and second interlayer spacings, $d(Cl_2\text{-}Na_1)$ and $d(Na_3\text{-}Cl_2)$, respectively, and the movement of the surface Na cations into the bulk

thereby causing a buckling of 0.12 Å at the surface termination. This buckling of the surface has been theoretically predicted due to the different electron polarizabilities of the ions at the (100) surface [47]. Although buckling of the (100) surface of a rocksalt structure has been seen previously, e.g. in MgO(100) [48,49], this work represents the first evidence for this effect in NaCl.

Chapter 6

Structural Analysis of LiF(100) Thin Films on Pt(111)

6.1 INTRODUCTION

The experimental history of LiF(100) in the surface science literature mirrors that of NaCl(100), because both NaCl and LiF were used for the exact same reasons: 1. chemical inertness 2. Easily formed surface 3. well characterized structure [65]. Similar to NaCl(100), LiF(100) is a benchmark system for new innovations in structure determination. One of the first quantitative low energy electron diffraction (LEED) intensity analysis on a non-metal was performed on bulk cleaved LiF(100) [44]. The calculation used a nonrelativistic model for the scattering properties and did not benefit from a R-factor directed structure search. After a visual inspection of the correspondence between the theoretical and experimental diffraction intensity versus electron energy (I-V) curves, the surface was found to possess a 0.25 Å surface corrugation due to the Li^+ ions being displaced towards the bulk. Additional structural studies have not confirmed this finding. In fact, He atom scattering experiments have concluded the contrary; the Li^+ is displace towards vacuum by 0.307±0.003 Å from its bulk position [66]. To confuse the issue further, another structural

method, low energy positron diffraction, reported that the ions maintain their bulk positions to within 0.01 Å [67].

LiF(100) was chosen for this work because the bulk atomic polarizability of Li^+ and F^- were less than that of Na^+ and Cl^-. Specifically, the bulk atomic polarizability of Li^+ is less than one sixth the polarizability of Na^+ and F^- polarizability is 2.5 times smaller than Cl. As mentioned in chapter four, polarizability is theorized to be the key variable driving the (100) surface corrugation of the alkali halides [25].

In this chapter, a detailed experimental description is absent, since the same experimental method in chapter five is employed for LiF. Specific information unique to the LiF experiments, such as substrate temperature and Knudsen cell temperature, have been included. The optimization of the nonstructural parameters was emphasized in the discussion of the tensor LEED analysis.

6.2 EXPERIMENTAL

LEED data were collected at normal incidence with a crystal temperature of ≈115 K in 2 eV increments over the range of 72-370 eV. To insure normal incidence, symmetric beams were compared to confirm that the changes in the I-V curve's minima and maxima were less than or equal to 2 eV. Symmetrically equivalent beams from both substrates were averaged, thus giving seven

symmetry inequivalent beams with a total range of 828 eV to be compared with theory.

6.3 RESULTS AND DISCUSSION

6.3.1 Ordering and Desorption Characteristics

A similar method to that employed in the growth of NaCl thin films, described in chapter five, was utilized in the ordering of LiF on Pd(100) and Pt(111) [8]. With the application of this procedure, LiF was successfully ordered on Pt(111) by exposing the substrate, held at a temperature on the edge of the multilayer desorption peak (~523 K), to the LiF vapor emitted from a Knudsen cell operating at 890 K for 15 minutes. Additional annealing to higher temperatures was then performed to induce further ordering of the film.

The first step in finding the optimum substrate temperature for deposition was to collect temperature programmed desorption (TPD) spectra for the LiF/Pt(111) systems. Figure 6.1 shows the desorption profile of the Li_2F parent peak, m/e=33, adsorbed on Pt(111). The lone feature exhibits an exponentially rising initial rate with a sharp falling edge. Such a profile is indicative of multilayer desorption [34]. Additional features were not observed even at lower coverages of the adsorbate.

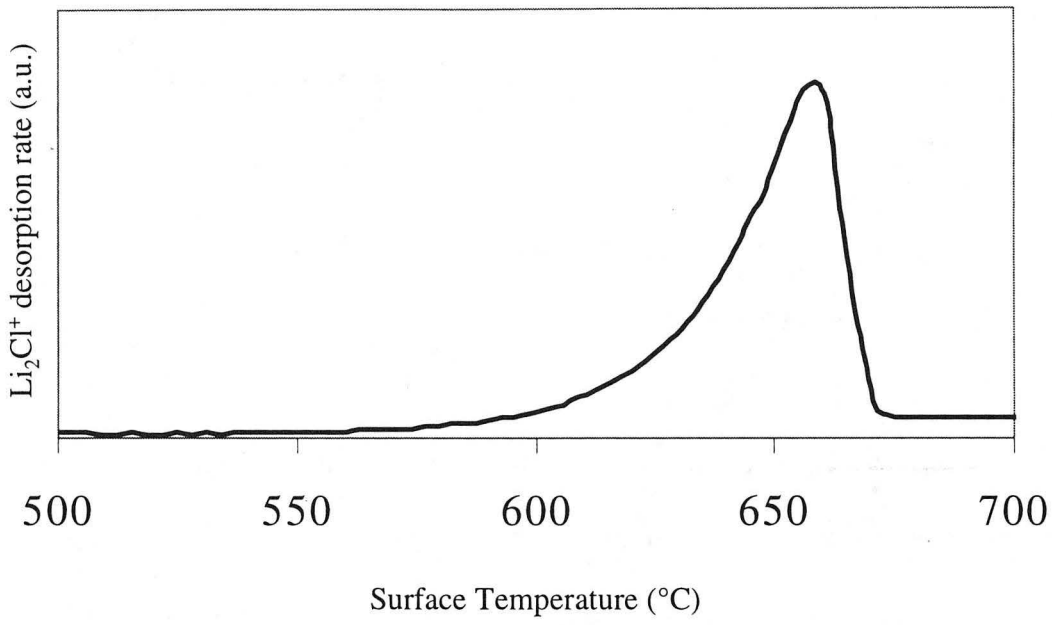

Fig. 6.1. Temperature programmed desorption profiles of a multilayer LiF film adsorbed on Pt(111).

6.3.2 LEED Observations

The film ordered in one domain on the Pt(111) surface illustrated in Fig. 6.2. The diffraction beam profiles were broader than were observed with the NaCl on Pt(111) pattern leading to the conclusion that the LiF film has smaller crystalline domains. There was an absence of the multiple rotated domain structure predicted by the symmetry differences between the adsorbate and the substrate.

LEED data were collected at normal incidence with a crystal temperature of ≈115 K in 2 eV increments over the range of 72-370 eV. To insure normal incidence, symmetric beams were compared to confirm that the changes in the I-V curve's minima and maxima were less than or equal to 2 eV. Symmetrically

equivalent beams from both substrates were averaged, thus giving seven symmetry inequivalent beams with a total range of 828 eV to be compared with theory.

6.4 LEED THEORY

The analysis of the I-V curves was begun by the generation of a set of temperature dependent phase shifts up to l_{max}=9 for Li and F in their neutral and ionic electronic configurations using a potential derived under the muffin-tin approximation for the unreconstructed bulk LiF(100) lattice with the Barbieri/Van Hove phase shift package. Inelastic scattering effects were modeled by the imaginary part of the inner potential, here being 5.0 V.

The LEED calculations were performed with the Barbieri/Van Hove symmetrized automated tensor LEED (TLEED) package [6,7,62,9].

(a)

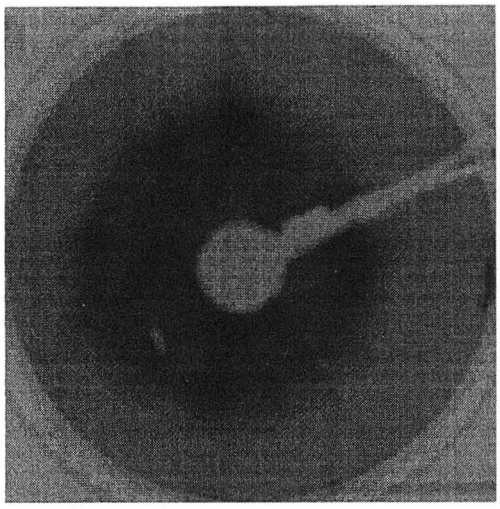

(b)

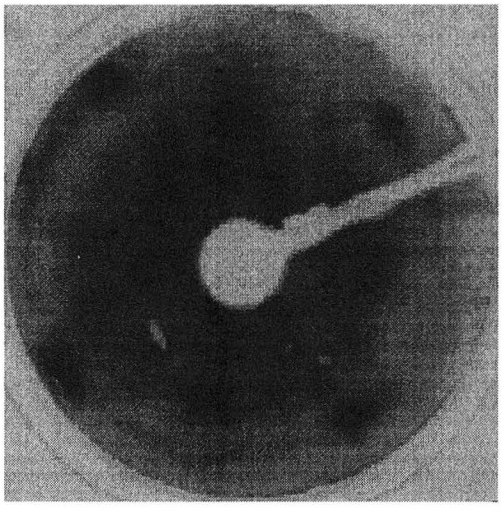

Fig. 6.2. LEED pattern of a LiF(100) multilayer on Pt(111) recorded at an incident energy of (a) 106 eV and (b) 90 eV.

Each layer in the (100) face of bulk-like LiF consists of a coplanar array of alternating F anions and Li cations. Each F-Li layer was defined as a composite layer. To describe the structure, five of these composite layers were used; two

defining the surface region where relaxations were allowed, and three defining the unrefined bulk.

For structural refinement, the tensor LEED approximation in combination with the Powell optimization scheme was applied. For all optimized structures, the final structure was defined as a new reference structure and the calculation was repeated, as a check on the approximation. The R-factor comparing theory and experiment and the error bars corresponding to the coordinates perpendicular to the surface were calculated with Pendry's formula [29].

6.5 SURFACE STRUCTURAL ANALYSIS

The square symmetry of the LEED pattern along with the experimentally determined lattice constant of 2.8 Å indicate an obvious choice for the basis of the trial structure--the bulk terminated LiF(100) surface [68]. Using the x-ray determined lattice parameter of 2.84 Å, the initial structure was constructed from five ideally occupied Li and F layers. The four structural parameters that were refined were the first two intralyer distances in the first (surface) and second layer and the two topmost interlayer distances (the spacings between the surface and the second layer and the second and third layer). Constraining these structural parameters was the preservation of the initial structural symmetry in the resulting structures. The only nonstructural parameter that was refined in this stage was the muffin-tin zero. The phaseshifts describing the scattering properties of the atoms

were synthesized using the electronic configuration of the neutral F and Li atoms and the muffin-tin radii equal to the atomic radii, 0.71 Å and 1.52 Å respectively [64].

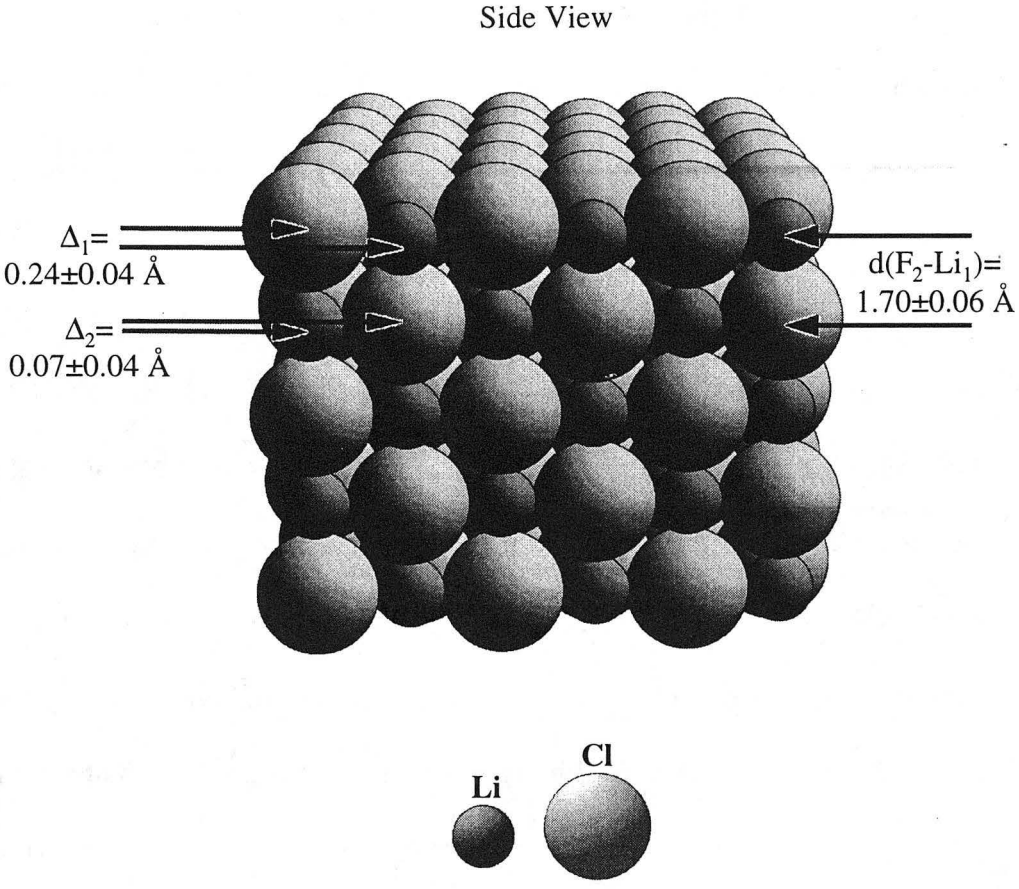

Fig. 6.3. Side view of the optimized LiF(100) surface grown on Pt(111) (the surface termination is on top); the ionic radii were drawn full size. The values of the interlayer and intralayer spacings in the refined region Are shown. The bulk spacings are $\Delta_1=\Delta_2=0.00$ Å and d(F_2-Li_1)=2.00 Å.

Additional refinement of this model included the reduction of the muffin-tin radii of the refined layers by 10% to account for the ions' size reduction with the loss of coordination at the surface. The final structure with an R_{Pendry}=0.24 is illustrated in Fig. 6.3 and represents the structural solution of LiF(100) on Pt(111).

The obvious difference between the surface structure and the bulk is the buckling of the surface and second layer. The surface intralayer spacing refined to a value of Δ_1=0.24±0.04 Å resulting in a corrugation of the surface by 12% of a interlayer distance. This surface reconstruction results from the movement of the Li atoms toward the bulk relative to the F atoms. This movement of the Li atoms are again responsible for the corrugation of the second layer, Δ_1=0.06±0.04 Å, by 3.0% of an interlayer distance. These modifications of the surface reduced the first interlayer distance, $d(F_2\text{-}Li_1)$, where the indices number the layers, from 2.01 Å to 1.77±0.06 Å. The contraction of the first interlayer spacing forces the overlap of the surface and second layer ions, since the sum of Li^+ and Cl^- ionic radii is 2.0 Å. This overlap is eliminated if there is a 10% reduction of the ionic radii in the first two layers; this degree of reduction in radii is common with coordination loss in ionic systems.

In order to insure that the calculated structural shifts are not an artifact of the assumptions included in the refinement two nonstructural parameters were varied systematically: 1. the number of the layers allowed to be at the reduced value (90%) of the muffin-tin radii 2. the amount of reduction of the muffin-tin

radii were varied.

The first parameter varied was the depth of the ion shrinkage. In the fully optimized structure, the first two surface layers possessed a muffin-tin radii that was 90% of the bulk muffin-tin radii. In the calculations which determined the correlation between the depth of the ion shrinkage to the R-factor, the atomic scattering characteristics of each atomic layer was changed in the range of no reduction of ion size to all the layers' ionic radii shrunk by 10% (Fig. 6.4(a)). With the exception of the model with only one layer possessing the reduced ion sizes, all the optimized structures refined down to a R_P ranging from 0.238 (allowing the first two layers to be reduced) to 0.244(allowing the first three layers to be reduced) with all structural parameters within the error bars calculated for the structural solution.

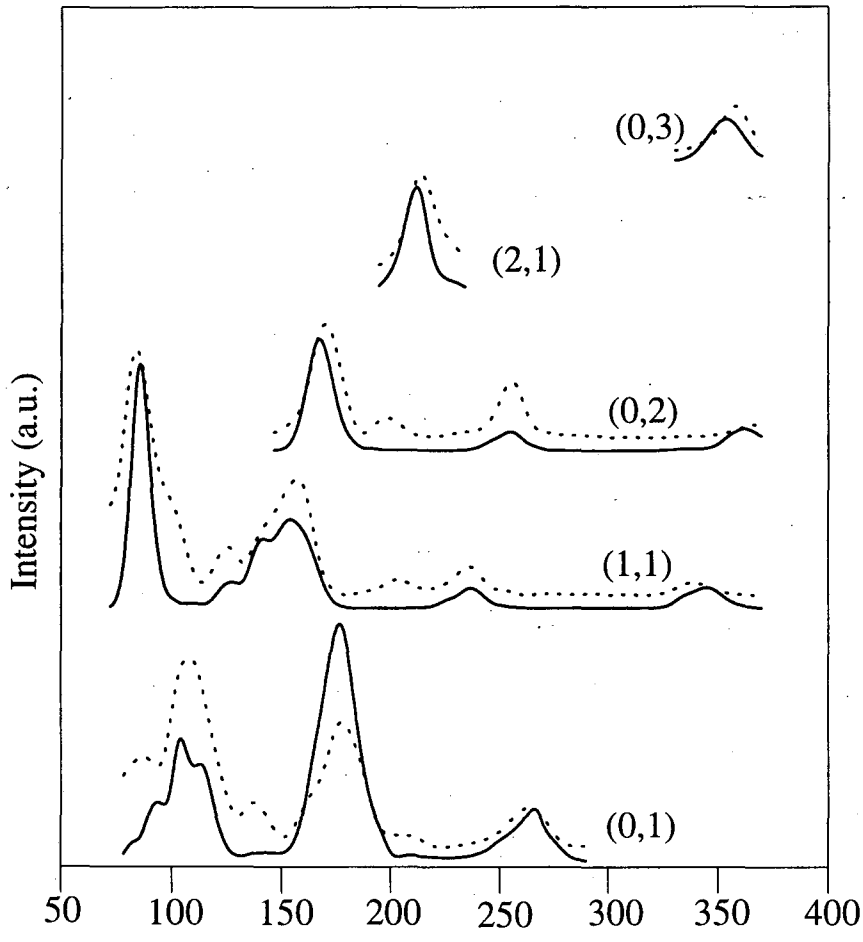

Fig 6.4. Comparison of the theoretical (dashed lines) and experimental (solid lines) I-V curves for the fully optimized LiF(100) multilayer adsorbed on Pt(111). All beams used in the calculations are represented here along with their indices.

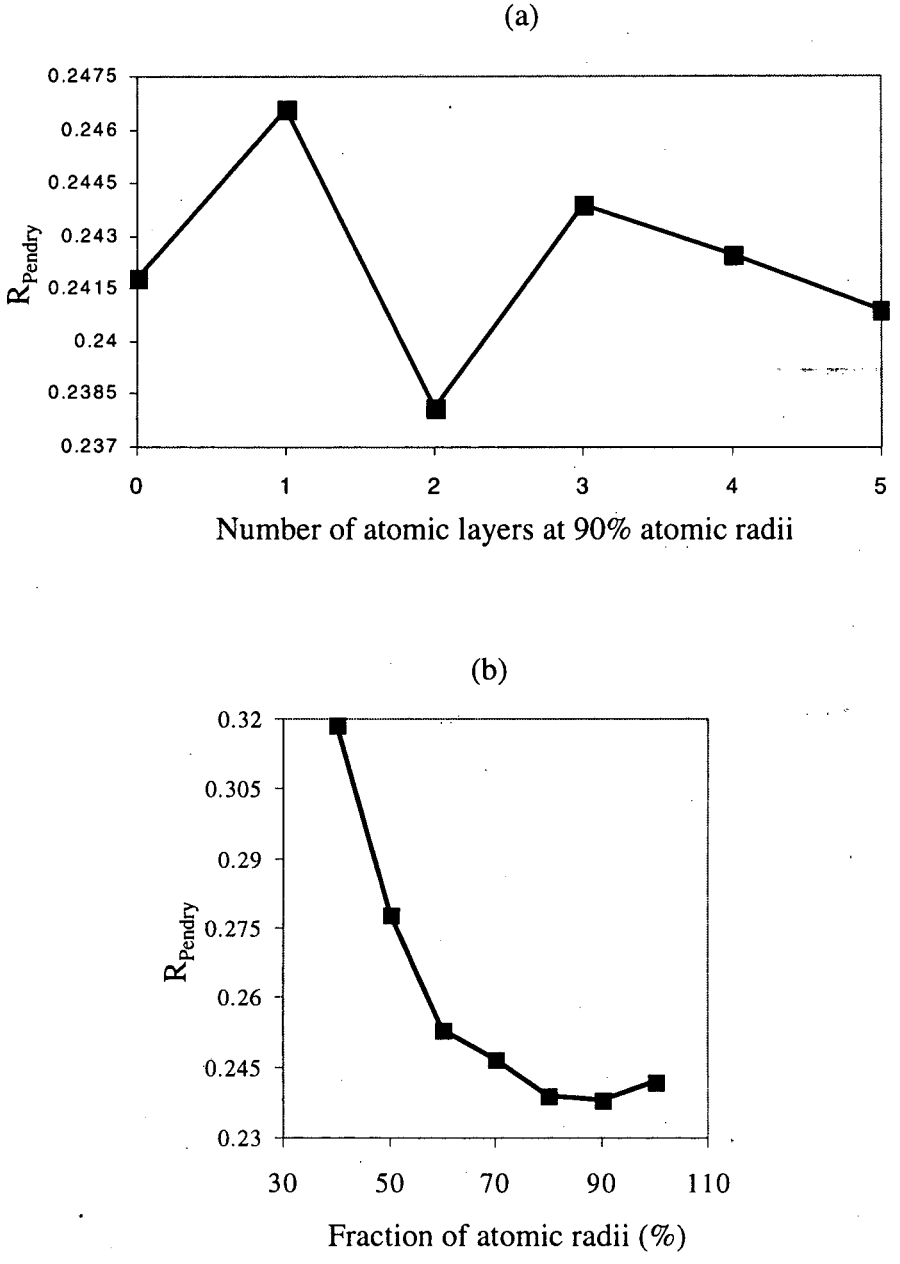

Fig. 6.5. Trend charts determining (a) the depth of the ion shrinkage and (b) the amount of ion shrinkage in the second layer of the LiF(100) multilayer on Pt(111).

The trial structure with only one atomic layer with the reduced muffin-tin radii had an R_P=0.25 with the first layer corrugation, Δ_1, being 0.20 Å and the second layer corrugation, Δ_2, being 0.13 Å.

The second parameter systematically varied was the surface ion size. This parameter was changed indirectly by varying the muffin-tin radii of Li and F. The value of the muffin-tin radii was varied from 100% to 40% of the bulk atomic muffin-tin radii. Fig. 6.4(b) illustrates the strong dependence of R_P on ion shrinkage in the first two atomic layers. Very similar R_P's are found when the first two atomic layers' muffin-tin radii are allowed to be 90% and 80% of the bulk radii; R_P=0.238 and 0.239 respectively. These models share more than just similar R_P's; their interlayer and intralayer spacings are within error bars of the structure illustrated in Fig. 6.3. Decreasing the muffin-tin radii to 70% and below yields large R_P's with structures that have larger values for Δ_1 and smaller values for $d(F_2\text{-}Li_1)$.

Previous work with iron oxides has indicated that ionic phaseshifts do not benefit the structure [13]. For the alkali halides, the ion sizes differ greatly from their atomic counterparts. In LiF, the atomic radius of F is 0.71 Å, but for F^- this radius swells to 1.4 Å; for Li, the neutral atom radius is 1.52, and its ionic radius is 0.6 Å. This disparity between the atomic and ionic radii was first modeled in these calculations by changing the muffin-tin radii of the neutral atoms to that of

the ions, but maintaining the neutral atom electronic configuration. After optimization, the R_P increased to a value of 0.28. The surface layer corrugation, Δ_1, was within the error bars of the structural solution, but the first interlayer spacing, $d(F_2\text{-}Li_1)$ and the corrugation of the second layer, Δ_2, was reduced; the values for these parameter were 1.77 Å and 0.02 Å respectively.

Increasing the sophistication of modeling the ionic character of the Li^+ and Cl^- included modifying the one electron orbital configurations to reflect the ionic charge densities of the compound. The structure that resulted from this modification had a R_P=0.36. The first intralayer spacing, Δ_1, was reduced with respect to that of Fig 6.3 by 0.07 Å as well as the first interlayer spacing, $d(F_2\text{-}Li_1)$, by 0.06 Å. The second intralayer spacing, Δ_2, was only 0.01 Å larger than the structural solution.

6.6 SUMMARY AND CONCLUSIONS

In summary, the surface structure of the multilayer LiF(100) thin film adsorbed on Pt(111) has been determined by the automated tensor LEED method. Starting with an initial trial structure consisting of an ideally terminated (100) LiF surface with the surface lattice parameter maintained at the bulk value of 2.84 Å, the refinement produced a surface with the top layer Li displaced below the F by 0.24±0.04 Å. This reconstruction was not isolated to the surface layer, but a

similar reconstruction was measured in the second layer. In the second layer, the Li was again below the F, but the magnitude of the shift was reduced to 0.07±0.04 Å. These corrugations of the first and second atomic planes reduced the first interlayer spacing to 1.70±0.06 Å, a value smaller than the close-packing distance, 2.0 Å of Li and F atoms. A reduction of the Li and F atomic radii by 10% allows, within error of the calculation, the accommodation of the ions within the refined distance. Although a 10% reduction of the atomic size gave the lowest R_P, calculations, when the atom size was varied systematically by changing the muffin-tin radii, it was concluded that the atomic radii reduction in the LiF(100) surface is between 10-20%, since the structures had similar R-factors, differing only by 0.0004, and possessed shifts within error bars of one another. This magnitude of ionic radii shrinkage is common with the coordination loss which is occurring at the surface termination.

The surface structure of NaCl was previously performed in this group [58]. The fully optimized NaCl structure had the same general features as those found in LiF. For example, the surface corrugation resulted from the movement of the alkali metal ions moving towards the bulk. Also, there was a significant contraction of the first interlayer spacing. This contraction of the first interlayer distance required, in both LiF and NaCl, the reduction of the ionic radii in order to accommodate the spacing.

The differences between LiF and NaCl was mainly seen in the magnitudes of these shared deviations from their respective bulk structures. The corrugation

of the constituent layers was not as pronounced in NaCl as it was in LiF. The first intralayer distance in NaCl was only 4.3% of an interlayer spacing compared to 12% in LiF. In addition, the second LiF layer from the surface also exhibited a 2.5% corrugation caused by the movement of the alkali metal ions towards the bulk; a feature absent in NaCl. The first interlayer distance of LiF was also decreased by a greater relative and absolute amount in comparison to NaCl.. The first interlayer spacings of NaCl and LiF was contracted by 3.5% and 12% of the bulk interlayer spacings respectively. These structural differences between NaCl and LiF are believed to be related to the difference between of the constituent ions' polarizability. The increased polarizability of the NaCl does not require large physical shifts of the ions to compensate for the coulombic interaction loss at the surface. The more tightly bound outer shell of charge in LiF requires a movement of the ions to balance this interaction loss.

These surface layer deviations from the ideal terminations have been theoretically predicted through the application of a classical shell and core model for the ions previously described in chapter four. Although the relative positions of the surface ions have been qualitatively predicted by this model, the actual displacements of the Li and F do not agree. It was theorized that the LiF surface had a 4.8% corrugation; the measured value was 2.5 times larger. When comparing the ionic positions in the second layer, the theoretical and experimental results converge on similar values for the corrugation, 2.2% and 2.5% respectively, but the structural solution determined that the Li was below the Cl in

the second layer while the model stated that the Cl was lower. Such differences between the model and real systems have been suggested by the theorists themselves, because the parameters used in the calculations were not self-consistent, thus only qualitative correlations between structure and polarizability should be concluded from these theoretical results [47].

Chapter 7

Surface Study of $MgCl_2$ Monolayers and Multilayers on Pd(111)

7.1 INTRODUCTION

The most active and commercially used form of the Ziegler-Natta polymerization catalyst is supported on $MgCl_2$ [69]. Its enhanced activity and stereospecificity has been linked to the surface structure of the substrate itself. Current theories suggest that the support acts as a template for the creation of active sites whose structural and electronic properties are conducive for the high turnover and stereoselectivity desired in the commercial production of polyolefins [70]. Despite the obvious importance of the support, there is a lack of information regarding $MgCl_2$'s surface structure. The same problems that hindered the investigation of the alkali halides are responsible for the dearth of surface structural information about $MgCl_2$—charging and electron stimulated desorption (ESD) of halogen neutrals. Since $MgCl_2$ and the alkali halides share the same experimental hurdles, the same method was employed in working with $MgCl_2$ as was used with the alkali halides. This chapter, based on references 71 and 72, describes the adsorption characteristics of $MgCl_2$ monolayers and multilayers on Pd(111). A detailed description of a stable monolayer structure with a significantly different unit

cell than the multilayer structure as well as a full tensor LEED analysis of the multilayer $MgCl_2$ film are included in the following sections.

7.2 BACKGROUND

A majority of the commercial production of polyethylene and polypropylene results from the use of very high activity $MgCl_2$ supported Ziegler-Natta heterogeneous catalysts. The catalyst is produced by comilling $MgCl_2$ with $TiCl_4$ and an electron donor. The role of the $MgCl_2$ support in increasing the activity of the catalyst over other more common supports such as SiO_2, MgO and Al_2O_3 has yet to be unambiguously determined [69]. Based on detailed analysis of the resulting product polymer, the structure of $MgCl_2$ is theorized to aid the $TiCl_3$ active site by adsorbing it in a specific orientation as to enhance the activity and stereospecificity of the catalyst. In addition to structurally complementing the Ti active site, the $MgCl_2$ is believed to back donate electrons to the more electronegative titanium, which stabilizes the coordination of the organic monomers, thus enhancing monomer insertion [69].

7.3 EXPERIMENTAL

7.3.1 Sample Preparation

Experiments were performed in the same stainless steel ultra high vacuum (UHV) chamber previously described in chapter three. The Pd(111) crystal was prepared from a commercially available boule with standard metallurgical methods, yielding a substrate aligned within 0.5° of the preferred crystallographic plane. The metal crystal was spot welded to the off-axis manipulator described in chapter three. Major contaminants, as measured by Auger electron spectroscopy (AES), were carbon and sulfur. Carbon was removed by repeated oxidation in $5x10^{-8}$ Torr of O_2 at a surface temperature of 1100 K; sulfur through the use of multiple cycles of 1-3 kV Ar^+ sputtering. Subsequent crystal vacuum annealing (2-3 hours) provided an optimum Pd(111) (1×1) LEED pattern.

All AES data were obtained with a PHI model 15-155 cylindrical mirror analyzer with an on-axis electron gun interfaced with a PC for the purpose of acquiring data and controlling the voltage ramp. Omicron Spectaleed electronics and optics provided the means for the visualization of the LEED patterns. LEED data were collected with a Dage-MTI intensified camera and a Matrox video capture card.

7.3.2 $MgCl_2$ Source

Using the same Knudsen cell as been described with the alkali halide work, the following mass spectrum (30-120 amu) of the source effluent, operating at ≈810 K, was recorded using an impact energy of 70 eV. This was obtained by subtracting the mass spectrum with the source at 720 K from one obtained with a source temperature at 810 K, the later being at a temperature where $MgCl_2$ sublimation is insignificant. The resultant spectrum shows three distinct sets of peaks which can be correlated with $^{35/37}Cl^+$, $Mg^{35/37}Cl^+$(amu 59 and 61) and $Mg^{35/37}Cl_2^+$ (amu 94 - 96) [87]. It should be noted that the peaks associated with Cl^+ and $MgCl^+$ fragments can be attributed to cracking fragments from $MgCl_2$ rather than from atomic chlorine or molecular MgCl produced by the source. The small peak at mass 44 can be ascribed to CO_2 which has not been completely removed through background subtraction. Figure 7.1 clearly illustrates that, using an appropriate temperature, the source can be utilized to provide a flux of essentially pure $MgCl_2$, consistent with thermodynamic equilibria [61].

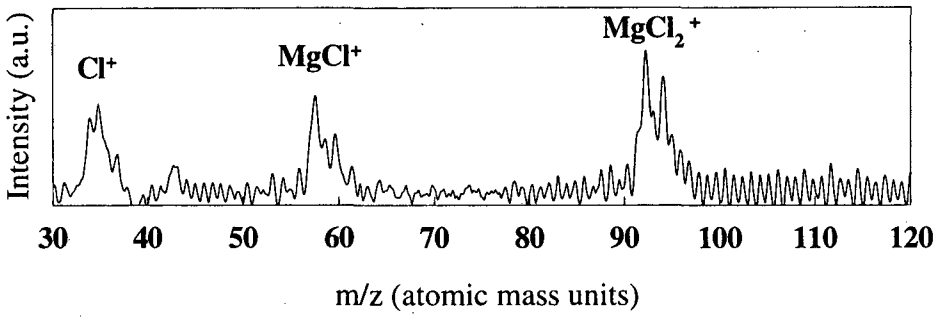

Fig. 7.1. Mass spectrum of the source effluent, operating at 810 K, recorded using an impact energy of 70 eV.

Corroborating evidence of the adsorption of stoichiometric $MgCl_2$ films is seen in Figure 7.2(a) which shows the AES of the surface, held at room temperature, after exposure to the $MgCl_2$ source for 30 minutes. The two peaks clearly visible at 181 eV and 1160 eV can be correlated with chlorine and magnesium respectively.

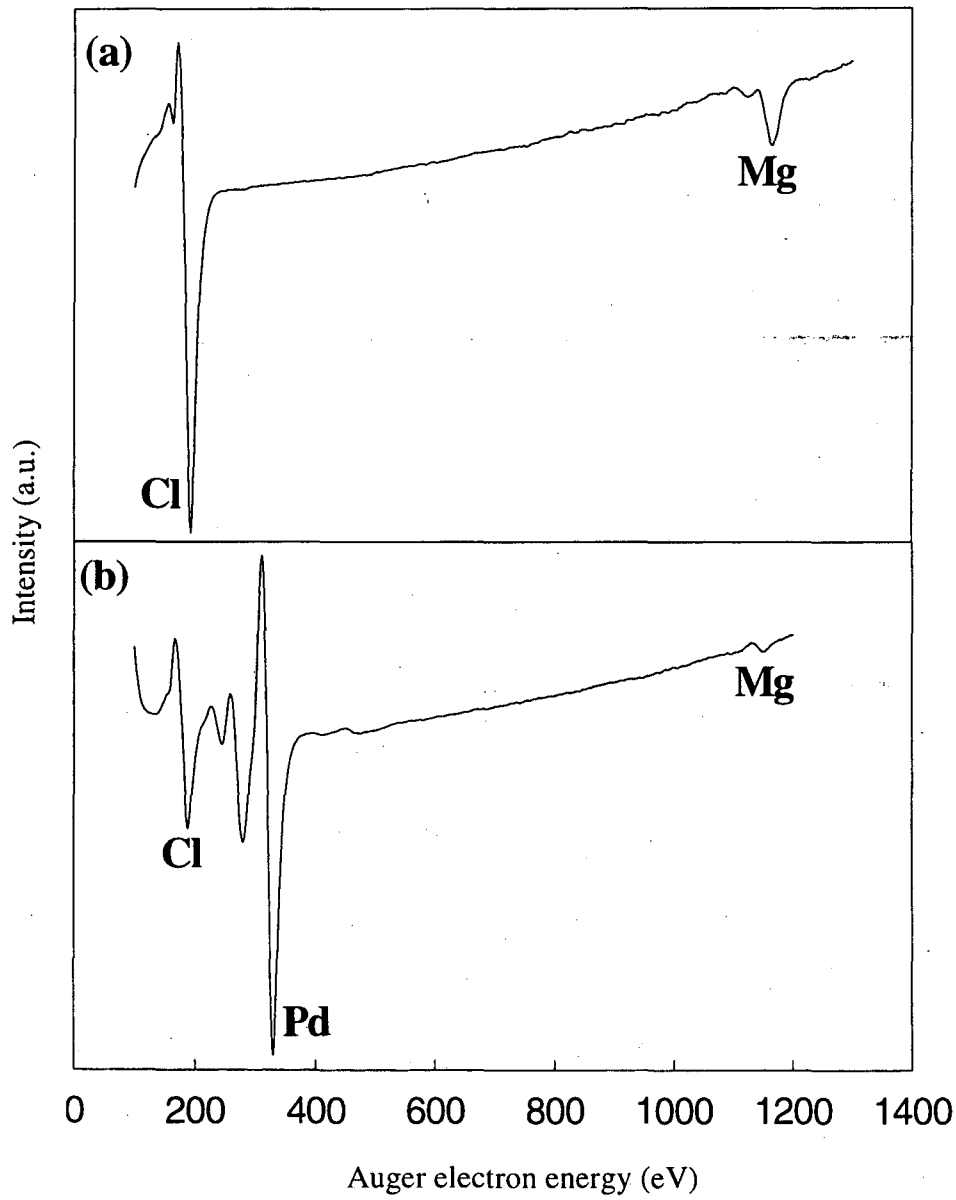

Fig. 7.2. AES of the Pd(111) surface held at (a) room temperature and (b) 650 K and exposed to the source for 30 minutes. Both spectra were recorded using 2 mA of emission current and a 3 keV primary beam energy.

The lack of any Pd substrate peaks is consistent with $MgCl_2$ multilayer formation. The existence of $MgCl_2$ multilayers can be verified by utilizing the measured AES peak-to-peak ratios (I_{Cl} and I_{Mg}). This measured signal is influenced by the inherent stoichiometry $\left(\frac{Mg}{Cl}\right)_{stoich.}$, the different sensitivities at 3 keV (s_{Cl} and s_{Mg})[13] and the mean free paths (λ_{Cl} and λ_{Mg}) associated with the Auger secondary electrons of these two chemical elements [74,74]. Since Fig. 7.2(a) was recorded at normal incidence, this relationship can be expressed in the form :

$$\frac{I_{Mg}}{I_{Cl}} = \left(\frac{Mg}{Cl}\right)_{stoich.} \cdot \left(\frac{s_{Cl}}{s_{Mg}}\right) \cdot \frac{1 - Exp\left(\frac{-1}{\lambda_{Mg}}\right)}{1 - Exp\left(\frac{-1}{\lambda_{Cl}}\right)} \qquad (7.1)$$

Using equation (1) the $\left(\frac{Mg}{Cl}\right)_{stoich.}$ is determined to be 1:2.05, which is in excellent agreement with the expected 1:2 chemical stoichiometry. This result supports the idea that the source effluent is composed of only $MgCl_2$.

Deposition was typically accomplished by positioning the Pd(111) surface 1-2 cm in front of the heated source for a controlled exposure time. AES measurements carried out at various positions on the surface revealed that careful control of the surface's spatial orientation with respect to the source was necessary to

ensure that a uniform flux of $MgCl_2$ at the surface is sustained. Unless noted, all depositions were carried out with a source temperature of 810 K.

7.4 RESULTS

7.4.1 Adsorption and Desorption Characteristics

Figure 7.3 shows the TPD of $MgCl_2$ films produced by exposing the Pd(111) surface, held at room temperature, to the heated source for various exposure times. Due to the difficulty in reproducing exact $MgCl_2$ coverages from similar source exposure the relative coverage in each case is determined by post-exposure AES. The desorption profile monitored at m/e= 94-96, encompassing the $Mg^{35}Cl_2^+$ and $Mg^{35}Cl^{37}Cl_2^+$ parent peaks, displays two distinct desorption features. The lower peak exhibits an exponential rise in the initial desorption rate accompanied by a sharp falling edge. This profile is consistent with multilayer desorption, as has been reported previously for $MgCl_2$ on polycrystalline gold [12]. In contrast, the higher temperature desorption peak displays characteristic first order kinetics with a roughly symmetric peak profile. Although the non-linearity of the temperature ramp does not allow for a detailed kinetic analysis, the desorption behavior shown in Fig. 7.3 indicates the presence of both multilayer and monolayer states. It should also be noted that there is

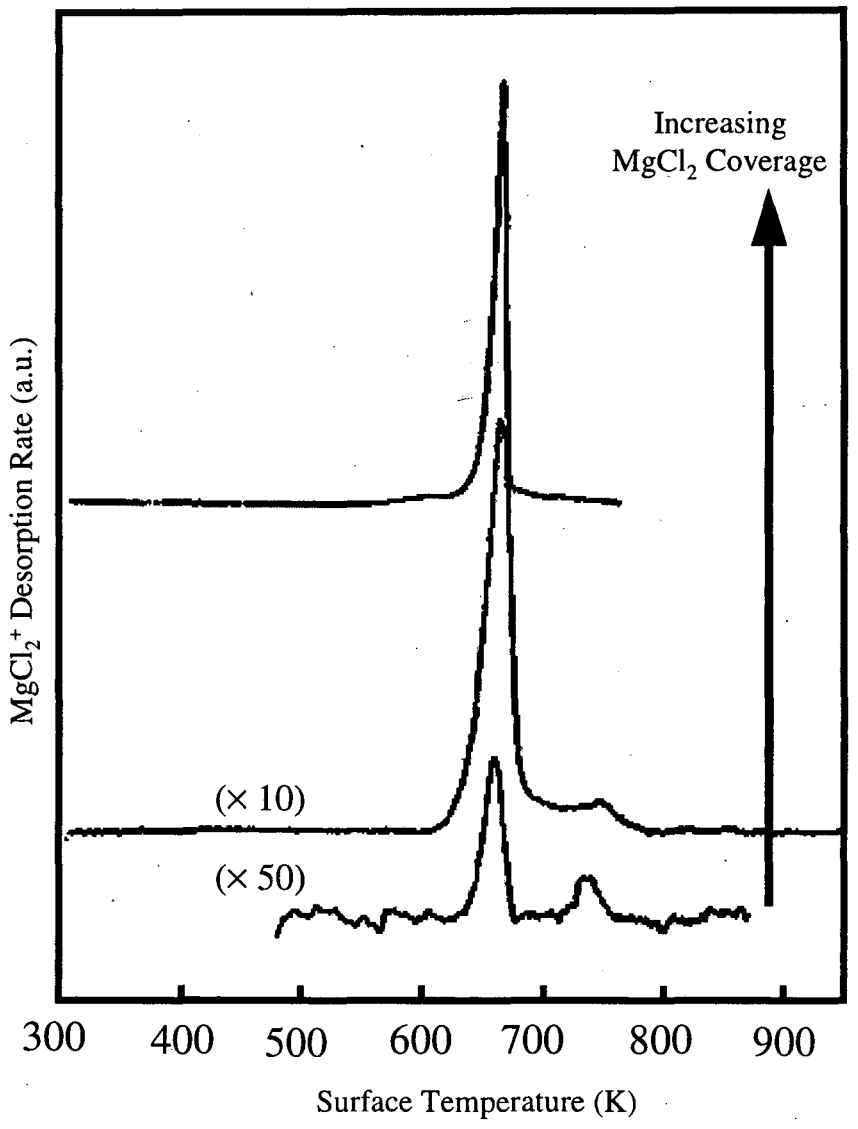

Fig. 7.3. Desorption profile of magnesium chloride deposited on Pd(111) monitored at mass m/e =95-97 corresponding to the parent $MgCl_2$ mass. These profiles are expressed as a function of increasing $MgCl_2$ coverage as measured by AES.

some contribution to the multilayer peak from $MgCl_2$ adsorbed on the manipulator support. Comparing the $MgCl_2$ TPD spectra as a function of coverage to the those of NaCl, it can be seen that the $MgCl_2$ films do not have the obvious desorption on-set temperature shifts that were observed for NaCl. This indicates that there are significantly larger domains being grown on the Pd(111) surface; this behavior alludes to a possible layer-by-layer growth mode versus islanding.

The possibility of a distinct, thermodynamically more stable monolayer phase located in the temperature region between the multilayer and monolayer desorption features is confirmed by comparing AES uptake measurements recorded as a function of exposure time. In these experiments, the sample was held at two separate temperatures during deposition, 298 K and 650 K, the latter falling within the multilayer desorption profile (see Fig. 7.3). With the sample held at room temperature, AES results indicate a rapid uptake of $MgCl_2$ leading to the production of a multilayer film in less than 5 minutes. In contrast, a 30 minute deposition at 650 K results in the AES shown in Fig. 7.2(b) which remains virtually unchanged for deposition times of up to 2 hours. The same surface spectrum can also be observed by adsorbing a thick film at room temperature followed by flashing the surface to 600 K to desorb the multilayer. Confirmation of the stoichiometry of this monolayer $MgCl_2$ structure illustrated in Fig. 7.2(b) can be obtained by application of equation (1) in the limit of single layer coverage. At a monolayer coverage, the $1 - \mathrm{Exp}\left(\frac{-1}{\lambda_i}\right)$ term, which represents the relative contribution from species below

the surface, can be neglected. As a result of the considerable difference in the mean free paths associated with chlorine and magnesium this effect produces a measurable change in the Mg:Cl peak-to-peak ratio in moving between multilayer and monolayer $MgCl_2$ films. Indeed application of equation (1) in these two limits is predicted to change the measured Mg:Cl ratio from 1:20 to 1:8.6, respectively. This is in excellent agreement with the 1:20.2 Mg: Cl ratio, in Fig.7.2(a) for a multilayer film, and the 1:8.4 shown in Fig.7.2(b).

It should be noted that an electron stimulated desorption process, analogous to that previously reported for $MgCl_2$ films grown on a gold substrate and for NaCl, produces a reduction in the Cl concentration along with a concomitant increase in oxygen signal associated with MgO formation [75]. So as to minimize this effect, all AES used in this study are the result of a single scan.

7.4.2 Qualitative Structural Analysis

As in the case with NaCl and LiF, thick multilayer $MgCl_2$ films grown at room temperature yielded no ordered structures. However, when deposition was carried out on a Pd(111) surface held at 643 K, three distinct LEED patterns were observed as a function of increasing coverage.

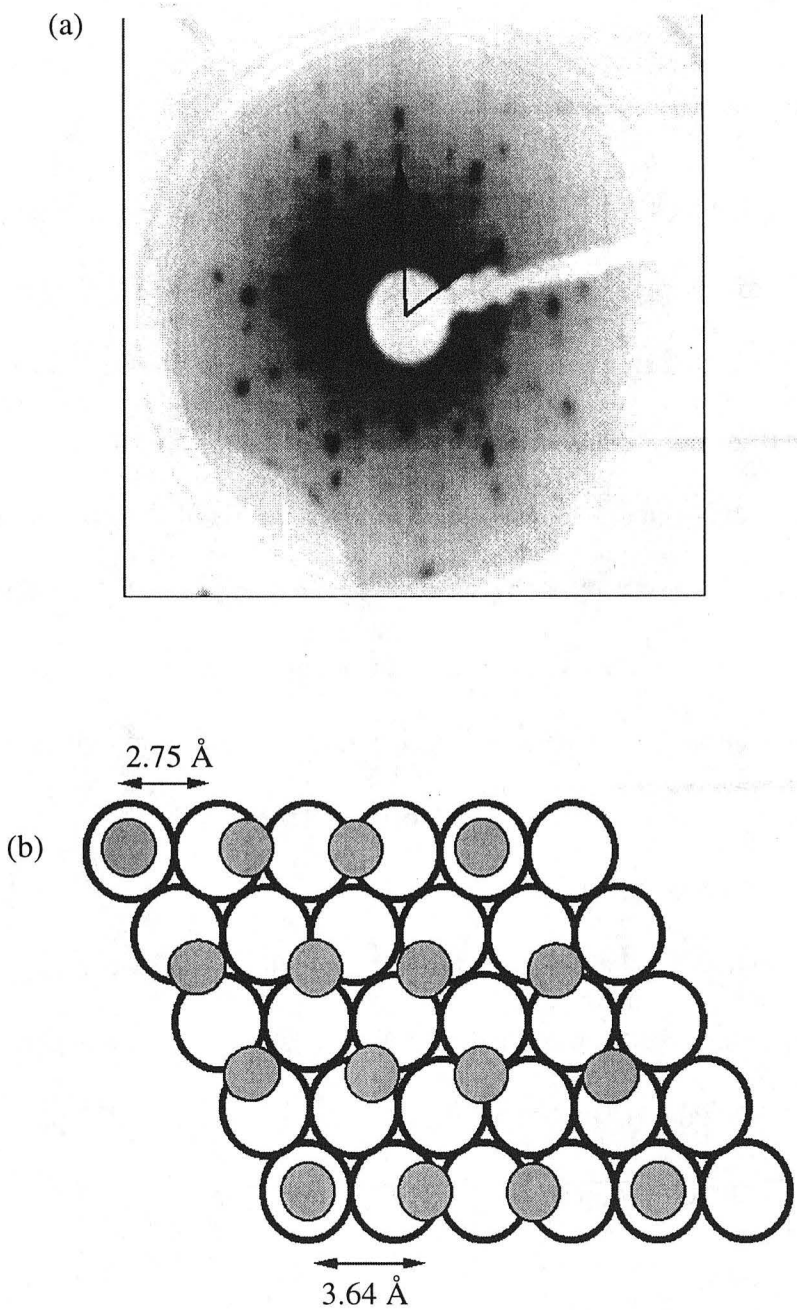

Fig. 7.4. (a) Pd(111)-(4 x 4)-$MgCl_2$ LEED pattern obtained by the deposition of ≈ 1ML $MgCl_2$, as measured by AES. LEED pattern were recorded at an electron beam energy of 130eV and a sample temperature of ≈120K. (b) Schematic representation of the structure corresponding to the (4 x 4) LEED pattern seen from the top. The Pd(111) surface atoms and first layer Cl^- ion are represented by hollow and gray circles respectively. Note that both the Pd-Pd and Cl-Cl unit cell dimensions are also shown.

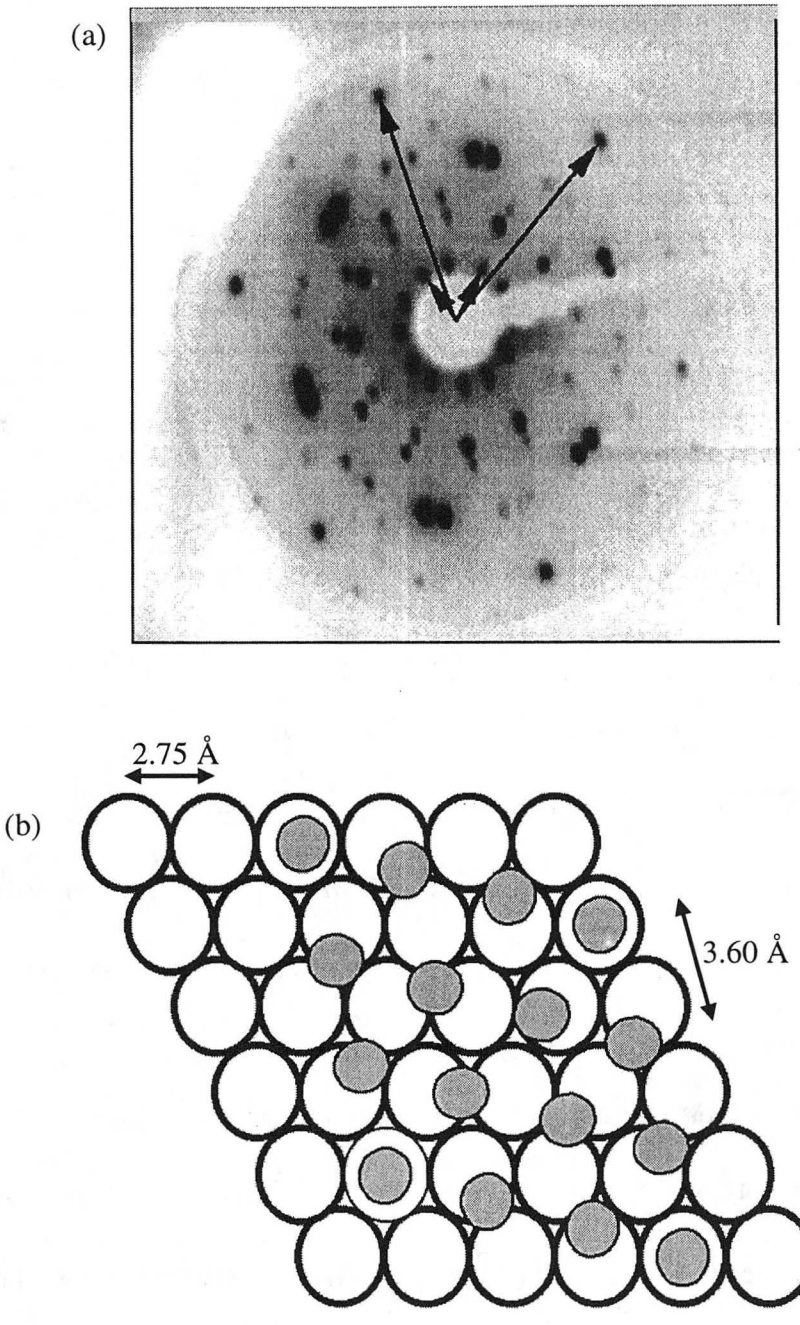

Fig. 7.5. (a)Pd(111)-($\sqrt{13}$ x $\sqrt{13}$) R13.9°-$MgCl_2$ LEED pattern obtained at 1ML $MgCl_2$, as measured by AES, recorded at an incident electron energy of 49eV with a sample temperature of ≈120K. The unit cell vectors corresponding to the overlayer (short arrows) and the substrate (long arrows) are drawn on the pattern. (b) Structure schematic corresponding to the Pd(111)-($\sqrt{13}$ x $\sqrt{13}$) R13.9°-$MgCl_2$ LEED pattern showing the Pd(111) surface atoms (hollow circles) along with the first layer Cl^- ions (gray filled circles). Note the lattice compression needed in $MgCl_2$ to attain the ($\sqrt{13}$ x $\sqrt{13}$) R13.9° lattice.

In these cases, the thickness of the $MgCl_2$ overlayer was estimated by monitoring the attenuation of the Pd peak at 333 eV upon deposition $\left(\frac{Pd_{MgCl_2}}{Pd_{Clean}}\right)$ from the equation, [40-42]

$$\frac{Pd_{MgCl_2}}{Pd_{Clean}} = Exp\left(\frac{-d}{\lambda_{Pd}}\right) \qquad (7.2)$$

where d represents the overlayer thickness and λ_{Pd} the mean free path associated with secondary electron production from Pd, both expressed in Ångstroms [74].

Two distinct LEED patterns are observed for $MgCl_2$ coverages ≈ 1 monolayer (ML). This coverage assignment is based upon the similarity of the measured AES with that shown in Fig.7.2(b). Fig. 7.4(a) shows a (4×4) LEED pattern observed at this coverage, recorded with an incident electron energy of 130 eV. Upon flashing the surface to ≈1000 K, the ordered overlayer desorbs intact leaving the Pd(111) surface. Pd peak attenuation measurements based on equation (2) indicate that this layer is 5-6 Å thick.

At approximately the same monolayer $MgCl_2$ coverage, another LEED pattern, shown in Fig. 7.5, is also observed, recorded at (a) 49 eV. This pattern can be identified as a Pd(111)-$\left(\sqrt{13}\times\sqrt{13}\right)$ R 13.9°-$MgCl_2$ structure comprised of two separate domains [76]. It should also be noted that it is this pattern, rather than the (4×4) pattern (Fig. 7.4(a)), which is observed after multilayer desorption from a >1ML film, initially deposited at room temperature.

7.4.3 Quantitative LEED Data Collection

The multilayer $MgCl_2$ thin film grown on Pd(111) exhibits a (1×1) hexagonal LEED pattern with threefold symmetry (Fig. 7.6(a)). With respect to the Pd(111) unit cell, there is a contraction, in reciprocal space, of the overlayer surface mesh by a ratio ($Pd:MgCl_2$) of $\approx$0.75 which is in good correspondence to the ratio between the bulk x-ray determined lattice constants of $MgCl_2$, 3.64 Å, and the Pd(111) unit cell, 2.75 Å.

The thickness of the film which yielded the experimental data was calculated to be 12 Å as measured by AES signal attenuation of the Pd 330 eV peak. Based on the adlayer thickness coupled with the penetration depth of elastically scattered electrons, a contribution to the LEED intensity data from the underlying Pd over the energy range employed (62-260 eV) is not expected, consistent with our experimental observation of no substrate spots present in the overlayer pattern. However, the influence of the underlying Pd(111) is responsible for the ordered overlayer growth, evidenced by the surface mesh vectors of the adlayer lying parallel to the Pd(111) unit cell vectors.

Data collection followed a standard procedure [32] with the exception of a lower beam current (0.36 μA), so as to minimize electron beam damage of the overlayer. LEED data were collected at normal incidence with a crystal temperature of $\approx$115 K over a range of 62-260 eV in 2 eV increments; I-V curves, shown in Figure 7.7, were obtained from these images with an I-V curve extraction program.

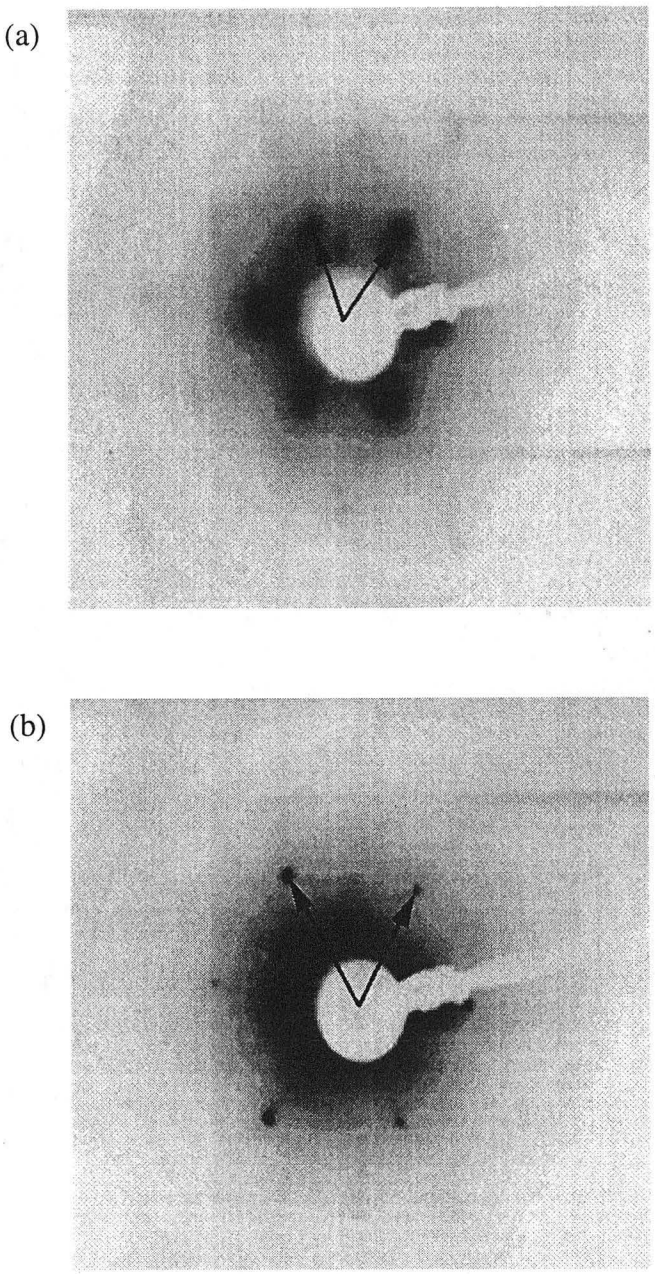

Fig. 7.6. (1 x 1) LEED patterns for (a) a 12 Å $MgCl_2$(0001) multilayer grown Pd(111) and (b) the underlying Pd(111) surface after thermal desorption of the $MgCl_2$ overlayer recorded at the same position as (a). Both LEED patterns were recorded at an electron beam energy of 100eV and a sample temperature of ≈120K. The arrows drawn on (a) and (b) represent the unit cell vectors for the MgCl2 overlayer and Pd(111) substrate, respectively.

As a check for degradation of the film over the course of data collection, data sets were taken while both increasing the energy from 62-260 eV and decreasing the energy from 260-62 eV. It was found that peak positions deviated less than 2 eV between sets, thus providing quantitative evidence that no measurable change to the film occurred during the time scale of data acquisition. All beam intensities were normalized to account for beam current fluctuations over the incident electron energy range. Symmetrically equivalent beams were averaged, thus giving seven symmetry inequivalent beams with a total range of 658 eV to be compared with theory. The quality of the theoretical fit to the data was measured by the Pendry R-factor (R_P) [29].

7.5 LEED THEORY

The LEED calculations were performed with the Barbieri/Van Hove symmetrized automated tensor LEED (TLEED) package [6,7,62,9]. Each Cl-Mg-Cl trilayer of the $MgCl_2$ structure was defined as a composite layer, and multiple scattering was treated exactly within each trilayer by the Beeby inversion scheme [2]. Scattering between pairs of trilayers was modeled with the renormalized forward scattering approximation.

For structural refinement, the tensor LEED approximation in combination with the Powell optimization scheme was applied. For all optimized structures, the

final structure was defined as a new reference structure and the calculation was repeated.

Using a maximum angular momentum value of 8, a set of neutral atom phase shifts was generated with the Barbieri/Van Hove phase shift package. The decision to disregard ionic phase shifts was based on previous work with iron oxides [13] which indicated that they introduced no significant changes in either the final structure or the R-factor.

7.6 DESCRIPTION OF STRUCTURAL NOTATION

The lamellar structure of $MgCl_2$ allows for a simple notation for the description of the models tested. Bulk $MgCl_2$ can adopt two ordered crystalline forms: α-$MgCl_2$ with the $CdCl_2$ crystal structure and the thermodynamically less stable β-$MgCl_2$ which adopts the CdI_2 structure [77,90]. In α-$MgCl_2$, the Cl anions pack in a face centered cubic arrangement with the Mg cations arranged in octahedral interstices such that each cation is surrounded by six anions. The β-form is based on the hexagonal close packing (hcp) of the anions with the cations placed in octahedral interstices. Viewing $MgCl_2$ perpendicular to the basal plane, the positions of the ions can be described for α-$MgCl_2$ as AbC BcA CaB... and for β-$MgCl_2$ as AbC AbC..., where the letters are indicative of the three possible lateral positions in an ABC ABC... type stacking, illustrated in Figure 7.8(a). The leftmost

letter indicates the surface layer, and the uppercase and lowercase letters represent the Cl and the Mg ions, respectively.

7.7 STRUCTURAL ANALYSIS

All trial structures were derived from the basal planes of α-$MgCl_2$ and β-$MgCl_2$. Because discrete diffraction spots with no significant degree of rotational disorder were observed, no initial structures based on δ-$MgCl_2$, the rotationally disordered form of the hcp structure, were tried [89].

The first trial structure was α-$MgCl_2$ with a Cl terminated full trilayer, AbC BcA CaB AbC... . The TLEED calculation took advantage of the full symmetry, a three fold axis with a mirror plane, with the only structural parameters being the first three interlayer spacings, Cl-Mg, Mg-Cl and Cl-Cl, as well as the muffin-tin zero. The lateral spacing of the atoms was held constant at its bulk value. The justification for leaving the lateral coordinates unchanged came from the determination of the surface lattice constant of the monolayer Pd(111)- (4×4)-$MgCl_2$ pattern [72]. In this monolayer pattern, the unit cell vectors are oriented parallel to the substrate's, and the substrate-adsorbate 4:3 coincidence lattice can be seen in the diffraction data as the (4×4) pattern. This is the same unit cell as the one found in the multilayer structure.

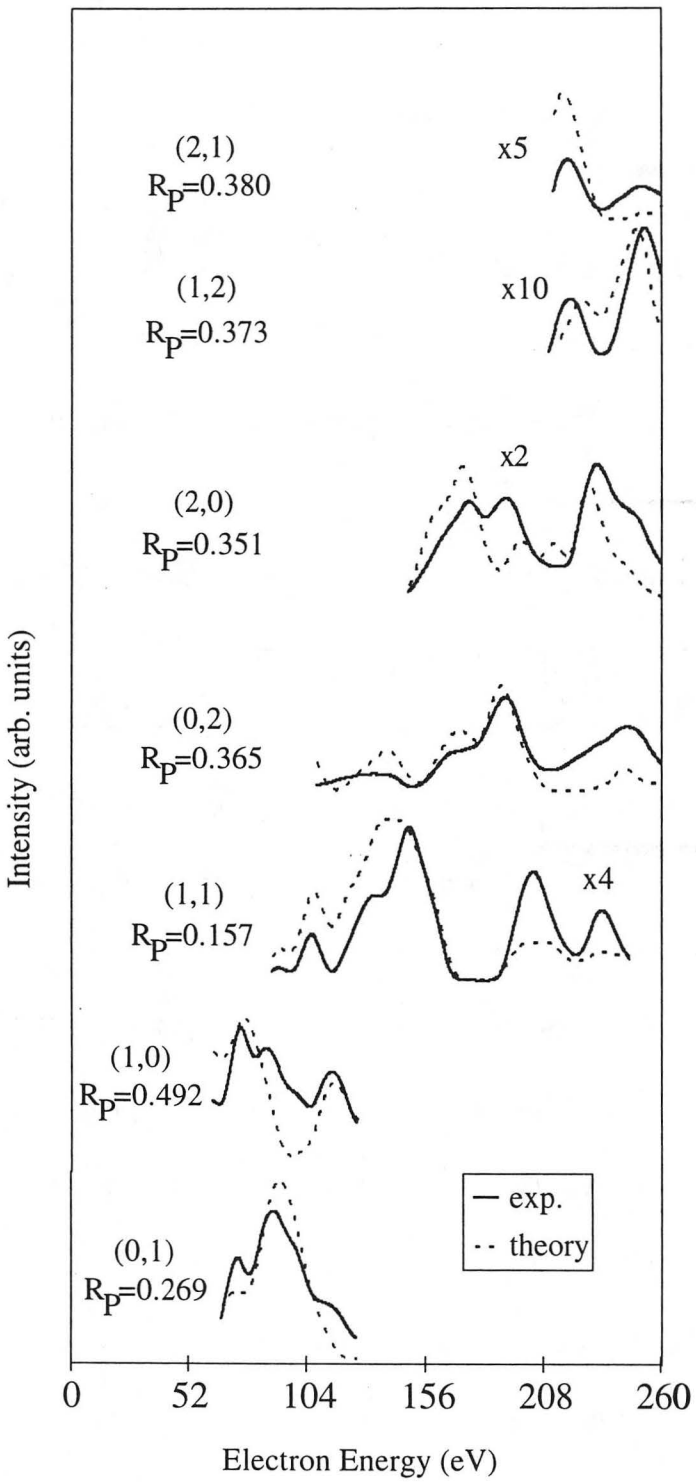

Fig 7.7. Comparison of the theoretical (dashed lines) and experimental (solid lines) I-V curves for the fully optimized Cl terminated full trilayer α-$MgCl_2$ structure solution. All beams used in the calculations are represented here along with their indices and individual R_P.

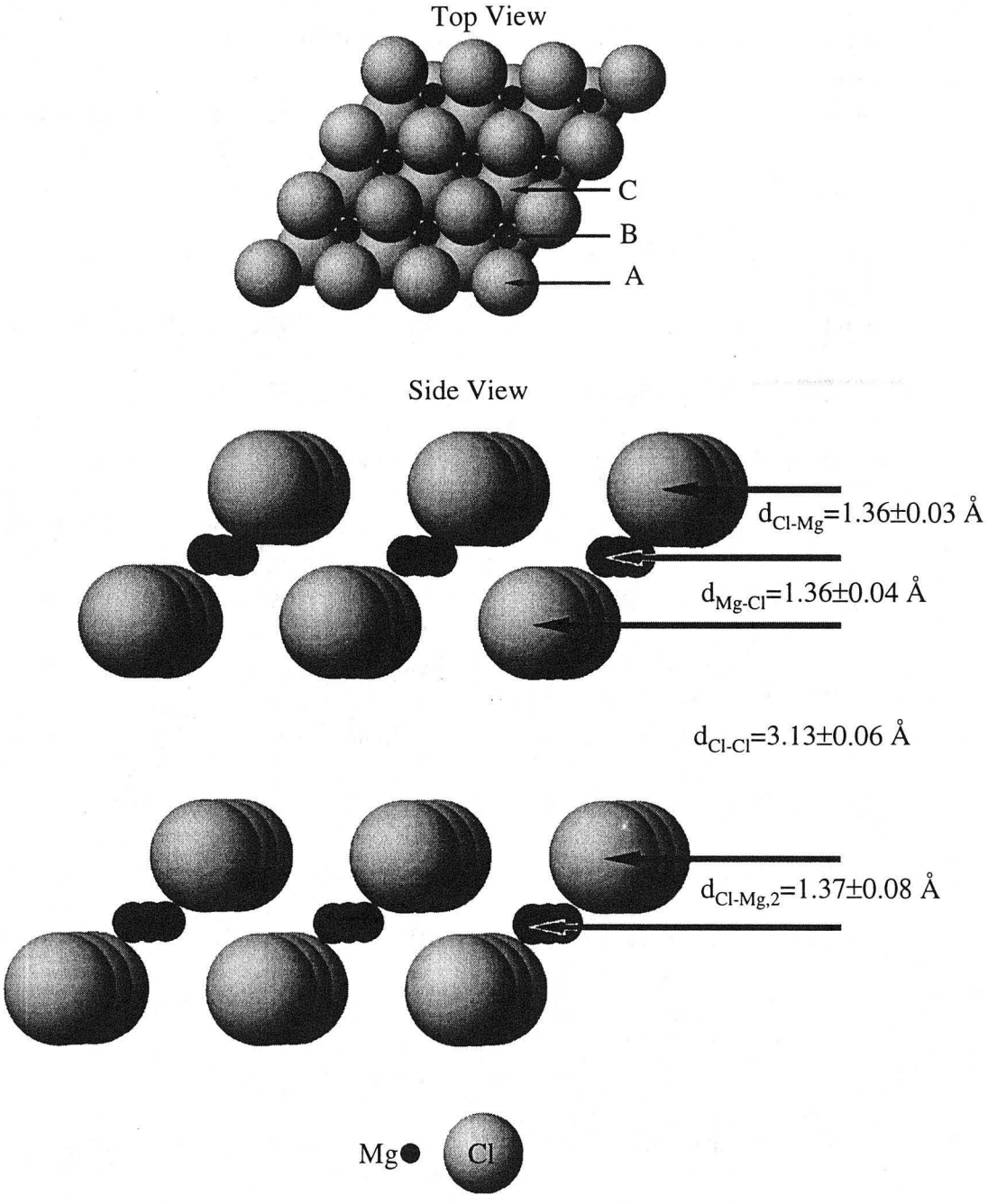

Fig. 7.8. (a) Top view of the α-$MgCl_2$ (0001) surface with the ionic radii reduced by 15%. (b) Side view of the α-$MgCl_2$ (0001) surface (the surface termination is on top). Interlayer spacings in the refined surface region are provided. Their bulk values are $d_{Mg\text{-}Cl,bulk}=d_{Cl\text{-}Mg,bulk}$=1.33 Å and $d_{Cl\text{-}Cl,bulk}$=3.22 Å. The ionic radii have been reduced by 50%.

But with the multilayer film being so thick as to remove any contribution from the underlying substrate, the diffraction pattern is simplified to a (1×1). The value of the lattice constant of the (4×4) pattern, assuming an unrelaxed Pd surface, shows a 0.03 Å expansion relative to the bulk $MgCl_2$ unit cell. This difference represents an estimate of the value for the error bars of the multilayer structure's lateral coordinates, a less than 1% change from the bulk value. The lowest R_P for this Cl terminated full layer, using the above procedure, was 0.332. Additional optimization of this model included the interlayer spacing refinement of the first Cl-Mg interlayer spacing in the second trilayer, which was previously held at its bulk position. The Debye temperature (Θ_{Cl}=306 K; Θ_{Mg}=446 K) of the surface layer was varied, to allow for surface softening, with no appreciable effect on the R_P. Figure 7.7 provides a comparison of the theoretical I-V curves which resulted from this last stage of refinement to the experimental curves. The final structure with an R_P of 0.317, illustrated in Figure 7.8, only experienced small deviations from the bulk in the refined interlayer spacings: $d_{Cl\text{-}Mg}$=1.36±0.03 Å, $d_{Mg\text{-}Cl}$=1.36±0.04 Å, $d_{Cl\text{-}Mg,2}$=1.37±0.08 Å versus 1.33 Å in the bulk; $d_{Cl\text{-}Cl}$ =3.13±0.06 Å versus 3.22 Å in the bulk.

To insure that a unique solution has been found, similar calculations were performed with the other possible terminations of the α-$MgCl_2$ basal plane. The Mg terminated α-$MgCl_2$ model, bC BcA..., refined to an R_P=0.513. In this model, the interlayer spacing between the outermost Mg layer and the underlying Cl layer, the

distance between the first pair of Cl's, the first Cl-Mg interlayer spacing in the first full trilayer and the muffin-tin zero were the only variables being refined. The refined structure differed from the initial one by a contraction of the Cl-Cl interlayer spacing by 0.07 Å with the Mg-Cl distances staying constant, thus giving a chemically reasonable structure, albeit with a significantly larger R_P. In evaluating the other termination of the α-form, a single layer of Cl on top of a full trilayer of $MgCl_2$, C BcA..., the single layer of Cl was defined as a simple layer while the underlying trilayer was defined as a composite layer. Parameters varied were: 1) the interlayer spacing between the surface Cl layer and the next Cl layer 2) both Mg-Cl interlayer spacings in the first full trilayer and 3) the muffin-tin zero. This model gave a R_P=0.629, with the Cl-Cl interlayer spacing increasing by 0.41 Å and the second Mg-Cl interlayer spacing reduced by 0.36 Å causing the Mg cation to overlap the underlying Cl ionic radii, an obviously chemically unreasonable structure. The first Cl-Mg interlayer spacing was reduced by 0.05 Å.

Calculations were performed on models based on the β-form with the same terminations used on the previously discussed α-structures. Each calculation used the same parameters and layer definitions as explained in the α-$MgCl_2$ refinements. The full trilayer Cl terminated model, AbC AbC..., refined to an R_P=0.489 where the Cl-Mg interlayer spacings differed from the bulk by a 0.03 Å expansion, and the Cl-Cl spacing was decreased by 0.24 Å. The Mg terminated model, bC AbC..., gave an R_P=0.622. The Mg terminated structure showed an increase of 0.10 Å in the first

Mg-Cl interlayer spacing with the second Mg-Cl spacing increasing by 0.03 Å and a decrease of 0.15 Å in the intertrilayer Cl-Cl separation. The single layer Cl structure, C AbC..., yielded an R_P=0.592, in which all the shifts from the reference structure were confined to expansions on the order of 0.05 Å.

Region[a]	Chemical Identity	Atom Number	Site Occupation	$X \pm \varepsilon_X$[b] (Å)	$Y \pm \varepsilon_Y$[b] (Å)	$D_Z \pm \varepsilon_Z$[c,d] (Å)
interface	Cl	1	1	2.0958	0	0
interface	Mg	2	1	0	0	1.36±0.03
interface	Cl	3	1	-2.0958	0	1.36±0.04
interface	Cl	4	1	0	0	3.13±0.06
interface	Mg	5	1	-2.0958	0	1.37±0.08
interface	Cl	6	1	2.0958	0	1.33
bulk	Cl	7	1	-2.0958	0	3.22
bulk	Mg	8	1	2.0958	0	1.33
bulk	Cl	9	1	0	0	1.33
bulk	Cl	10	1	2.0958	0	3.22
bulk	Mg	11	1	0	0	1.33
bulk	Cl	12	1	-2.0958	0	1.33
bulk	Cl	13	1	0	0	3.22
bulk	Mg	14	1	-2.0958	0	1.33
bulk	Cl	15	1	2.0958	0	1.33

[a]The interface region refers to the atoms at the vacuum-solid interface that were allowed to be refined in the calculation.
[b]Absolute lateral positions of the atoms are given in two-dimensional Cartesian coordinates.
[c]The provided error bars quantify the theoretical uncertainties of the refined parameters. The absence of error bars indicates that the value was not refined in the calculation, but held constant at its bulk value
[d]The perpendicular lattice positions are defined relative to the previous atom's position. The first atom listed represents the surface termination, and a positive D_Z value indicates a displacement towards the bulk.

Table 7.1. Full description of the refined α-$MgCl_2$ structure..

7.8 THIN FILM GROWTH DISCUSSION

A detailed picture of the growth of $MgCl_2$ thin films on Pd(111) can be surmised from the qualitative analysis of the LEED, Auger and TPD data in conjunction with the surface structural analysis.

Because of our limited ability in controlling the $MgCl_2$ source to extremely small fluxes, the examination of the thin film's morphology will proceed from a top-down approach starting with thick multilayer films and then synthesizing monolayer structures via desorption. In addition to creating monolayer structure, the use of an elevated surface temperature can control the thickness of the multilayer due to the fact that at an elevated temperature (≈640 K) there is a measurable difference between the sticking probability in monolayer and multilayer states allowing for the initial population of a full monolayer before subsequent multilayer formation.

The additional stability of the monolayer phase is evidenced by both the higher temperature TPD feature seen in Fig. 7.3 and the production of a $\left(\sqrt{13}\times\sqrt{13}\right)$ R 13.9° LEED pattern after flashing a $MgCl_2$ multilayer to ≈570 K and then lowering the surface temperature to 300 K.

The (4×4) surface structure shown in Fig. 7.4(a) at ≈1ML, indicates that the $MgCl_2$ overlayer forms a coincidence lattice with the Pd(111) surface. Given that:

$$a_{Pd} = 2.75 \text{ Å and } a_{MgCl_2} = 3.64 \text{ Å}$$

in either α or β phases the structure shown in Fig. 7.4(b) is consistent with the fact that,

$$4 \cdot a_{Pd} = 3 \cdot a_{MgCl_2} \qquad (7.3)$$

to within 0.7%, thus leading to an overlayer coincidence at every fourth Pd atom. The additional diffraction beams are the result of multiple scattering events, since now the effective scattering lattice is linear combination of the adsorbate and substrate lattices. Furthermore, from the LEED pattern, the unit cell of the overlayer lies parallel to that of the hexagonal Pd(111) surface. It should be noted that in this and all subsequent LEED patterns the exact position of the overlayer with respect to the surface atoms has been chosen arbitrarily in the absence of detailed I-V analysis. The proposed structure is also consistent with the estimated overlayer thickness of ≈ 6 Å which is in good qualitative agreement with that of the $MgCl_2$ unit cell (≈5.9 Å) [78].

AES results indicate that the $\left(\sqrt{13} \times \sqrt{13}\right)$ R 13.9° full monolayer structure has a similar overall $MgCl_2$ coverage to that of the (4 x 4) structure. This result leads us to propose the structure shown in Fig. 7.5(b), which can be derived by a 13.9° rotation of the (4 x 4) structure with a contraction of 0.36 Å in the $MgCl_2$ unit cell. Based on the relative sizes of the unit cells shown in Figs. 7.4(b) and 7.5(b), the following coverage relation can be derived:

$$[MgCl_2]_{(4 \times 4)} \approx 0.8 \cdot [MgCl_2]_{(\sqrt{13} \times \sqrt{13})R13.9°} \qquad (7.4)$$

which explains the observed similarity in the relative $MgCl_2$ coverages. The idea that the monolayer structure corresponding to the Pd(111)- $\left(\sqrt{13}\times\sqrt{13}\right)$ R 13.9° - $MgCl_2$ pattern is more densely packed than the (4×4) structure is also supported by recent experiments of $MgCl_2$ deposition on Pt(111) [79] whose results will be fully discussed in chapter eight. Briefly, on Pt(111) an identical set of $MgCl_2$ thin film LEED patterns to those found on Pd(111) are observed. In this case, careful annealing of the Pt(111)- $\left(\sqrt{13}\times\sqrt{13}\right)$ R 13.9° -$MgCl_2$ pattern, at a temperature sufficient to induce $MgCl_2$ desorption, is found to produce the Pt(111)- (4×4) - $MgCl_2$ pattern, indicating that the $\left(\sqrt{13}\times\sqrt{13}\right)$ R 13.9° structure is more dense than that associated with the (4×4) LEED pattern.

Further $MgCl_2$ deposition, as judged by AES, results in a simple (1×1) LEED pattern. Based upon a comparison of the relative size of the unit cell to that of the underlying Pd(111) surface, this corresponds to a hexagonal unit cell with a lattice parameter of ≈3.67 Å. This is consistent with an $MgCl_2$ film (a_{MgCl_2} =3.64 Å) whose structure is identical to that of the (4×4) [78]. The simplification in the LEED pattern results from the increase in film thickness. This removes any contribution from the underlying surface lattice because of the extreme surface sensitivity of LEED coupled with the considerable thickness of each individual $MgCl_2$ layer (≈5.9 Å) [80,90].

The observation of ordered commensurate LEED patterns in contrast to incommensurate overlayers provides structural evidence for the presence of significant substrate-adsorbate interactions leading to a preferred registry. The growth characteristics of this system are consistent with layer-by-layer rather than 3-dimensional island growth. This is readily explained on the basis of the strong ionic bonding parallel to the surface plane and the much weaker dispersive forces between adjacent $MgCl_2$ layers along the surface normal. Experimental evidence of a layer-by-layer growth, or at least the formation of macroscopic islands, is seen in the comparison of the adsorbed multilayer film LEED spot profiles to those of the clean substrate. Fig. 7.6 aids in performing this comparison. It can be seen that there is not a significant difference between the size of the $MgCl_2$ LEED beams and that of the clean surface. This qualitative analysis leads to the conclusion that the domain size in the $MgCl_2$ film is on the order of the Pd(111) domain size. Additional evidence of the creation of large domain structure in the adsorbed films is seen in the TPD spectra when viewed as a function of coverage. There was no change, on the order of the instrumentational limits, in the on-set temperature of desorption as there was in NaCl. This independence of the desorption characteristics from surface coverage is indicative of near infinite size domain [34].

Moving from the monolayer structure to that of the multilayer structure, the morphology of the interface layer with respect to the Pd substrate is in question. LEED observations do not provide the needed information due to the fact that the low energy electrons have a limited sampling depth. At 250 eV (which corresponds

to a sampling depth of approximately 8 Å), the highest energy used in the $MgCl_2$ multilayer investigation, diffraction intensity contributions from the substrate were absent, as a result we can not confirm the maintenance of the $\left(\sqrt{13}\times\sqrt{13}\right)$ R 13.9° structure at the adsorbate-substrate interface.

Assuming the $\left(\sqrt{13}\times\sqrt{13}\right)$ R 13.9° structure is maintained at the interface, the LEED data show that the multilayer structure is not an extension of the $\left(\sqrt{13}\times\sqrt{13}\right)$ R 13.9° template. The absence of a 13.9° rotation of the overlayer unit cell vectors with respect to those of the substrate's and the absence of the compressed lateral spacing of the $\left(\sqrt{13}\times\sqrt{13}\right)$ R 13.9° structure in the multilayer confirm this conclusion. With this information, one possible explanation which includes the interface $\left(\sqrt{13}\times\sqrt{13}\right)$ R 13.9° structure assumption is that subsequent layers adopt the bulk $MgCl_2$ structure, since the strain of having the $\left(\sqrt{13}\times\sqrt{13}\right)$ R 13.9° geometry can only be overcome at the Pd-$MgCl_2$ interface due to the significant adsorbate-substrate interaction. The subsequent layers do not experience this interaction directly, thus shifting back to the bulk lattice configuration.

An alternate explanation is that as mentioned before the second layer is not expected to experience any significant interaction with the Pd(111) surface, thus this layer reverts to that of the crystalline unit cell, as shown in Fig. 7.4(b) [78-80]. The strength of the interlayer Cl-Cl interactions appears to be greater than the energetic difference between the $\left(\sqrt{13}\times\sqrt{13}\right)$ R 13.9° and (4×4) structures. This causes the

monolayer structure to be lifted and replaced by the (4×4) structure (Fig. 7.4(b)), thus allowing interlayer interactions and packing to be maximized according to the bulk $MgCl_2$ structure. This explains why the multilayer lattice vector remains parallel to that of the surface, because in this ordered multilayer phase, the underlying template is the (4×4) structure.

The identical overlayer patterns observed for films of 12 and 24 Å thicknesses clearly indicates that once the bulk unit cell is established in the film that this growth mode extends beyond the second monolayer.

7.9 CONCLUSIONS:

The structure of $MgCl_2$ overlayers, at both monolayer and multilayer (thin film) coverages, grown on Pd(111) illustrates the interplay between adsorbate-substrate and adsorbate-adsorbate interactions. The existence of significant adsorbate-substrate interactions at low coverages (< 1ML) are evidenced by AES and TPD measurements which indicate the presence of a distinct monolayer phase. LEED studies coupled with AES indicate that at slightly less than monolayer coverages the presence of adsorbate-substrate interactions coupled with a coincident lattice match between Pd(111) and $MgCl_2$ results in the formation of a Pd(111)-(4×4)-$MgCl_2$ surface structure. Upon further addition of $MgCl_2$, the strength of the interaction between the Pd surface and the $MgCl_2$ overlayer is sufficient to

induce a lattice compression in the ionic solid in order to maximize the surface coverage forming a Pd(111)- $\left(\sqrt{13}\times\sqrt{13}\right)$ R 13.9°-$MgCl_2$ surface structure. Moving to multilayer coverages, the bulk $MgCl_2$ structure is recovered. This can be attributed to the greater strength of interlayer interactions between adjacent $MgCl_2$ layers compared to those between the surface and first monolayer.

Dynamical LEED I-V analysis of a $MgCl_2$ multilayer film on Pd(111) has identified the surface as the Cl terminated full trilayer (0001) face of α-$MgCl_2$, with very small relaxations in the interlayer spacing relative to the bulk (a maximum 3% expansion of the Mg-Cl interlayer distances and a 2.8% contraction of the Cl-Cl interlayer distance). These effects are reasonable on the basis of the layered structure of $MgCl_2$, since within the full trilayer Cl-terminated surface, the high degree of ionic bonding remains intact as the cleavage plane occurs between adjacent Van der Waals bound Cl layers. Since only the relatively weak Van der Waals interaction is removed, the surface is not expected to experience any large relaxations at the vacuum-solid interface. This is supported by the surface structure work performed on transition metal dichalcogenides where, like $MgCl_2$, the Van der Waals bonding between trilayers is interrupted at the surface termination. While the deviations from the bulk for the α-$MgCl_2$ structure are larger than the 1.0% interlayer spacing contractions found in the $NbSe_2$ system, the shifts for $MgCl_2$ are comparable to the relaxations seen in the MoS_2 surface, a S-Mo interlayer spacing contraction of 4.7% and a S-S contraction of 3.0% [81]. In addition, expansions of

the interlayer spacings, as seen in $MgCl_2$, are not unusual in the transition metal dichalcogenides; for example the $TiSe_2$ surface has an intratrilayer expansion of 3.0% coupled with an intertrilayer spacing contraction of 1.0% [82].

Chapter 8

$MgCl_2$ Monolayers and Multilayers Adsorbed on Various Transition Metals

8.1 INTRODUCTION

The appearance of a significant adsorbate-substrate interaction in the $MgCl_2$/Pd(111) system, described in chapter seven, was unexpected. This interaction between the ionic bonded $MgCl_2$ and the metallic Pd presents some fundamental questions about the bonding present at the interface. The influence of the metal on the electronic structure of the insulating adsorbate is also a mystery [14]. Such questions are answered for metal-semiconductor heteroepitaxy, since there is a considerable technological need for this information in the computer chip industry. Metal-insulator and semiconductor-insulator heteroepitaxy has become important in response to the development of three dimensional electronic circuits, but there are few studies documenting these systems.

Chapter eight, based on reference 79, reports the results of a systematic study of $MgCl_2$ adsorbed on various transition metals. The goal of this work is to determine the substrate's role in influencing the observed adsorbate-substrate interaction.

8.2 EXPERIMENTAL

Using the same experimental method described in chapter three, sufficiently thin films could be reproducibly generated on all of these transition metal surfaces that served as the basis for this study. On each surface, the same basic procedure was applied. First, the desorption characteristics were measured and then a multilayer structure was synthesized by holding the temperature of the transition metal crystal at a point corresponding to the on-set of multilayer desorption. Once the multilayer LEED pattern was observed, the annealing temperature was slowly increased using thermal desorption of the $MgCl_2$ as a means to probe the structure of the underlying monolayer.

8.3 RESULTS

8.3.1 Temperature Programmed Desorption (TPD)

Fig. 8.1(a) and (b) show the desorption characteristics of thin (<100 Å) magnesium chloride films, produced from the evaporation source, adsorbed on Pt(111) with the surface at room temperature. Film thicknesses for multilayer coverages were estimated by observing that the substrate spots were absent from the LEED patterns in the energy range of 50-250 eV, indicating an overlayer thickness of >20 Å.

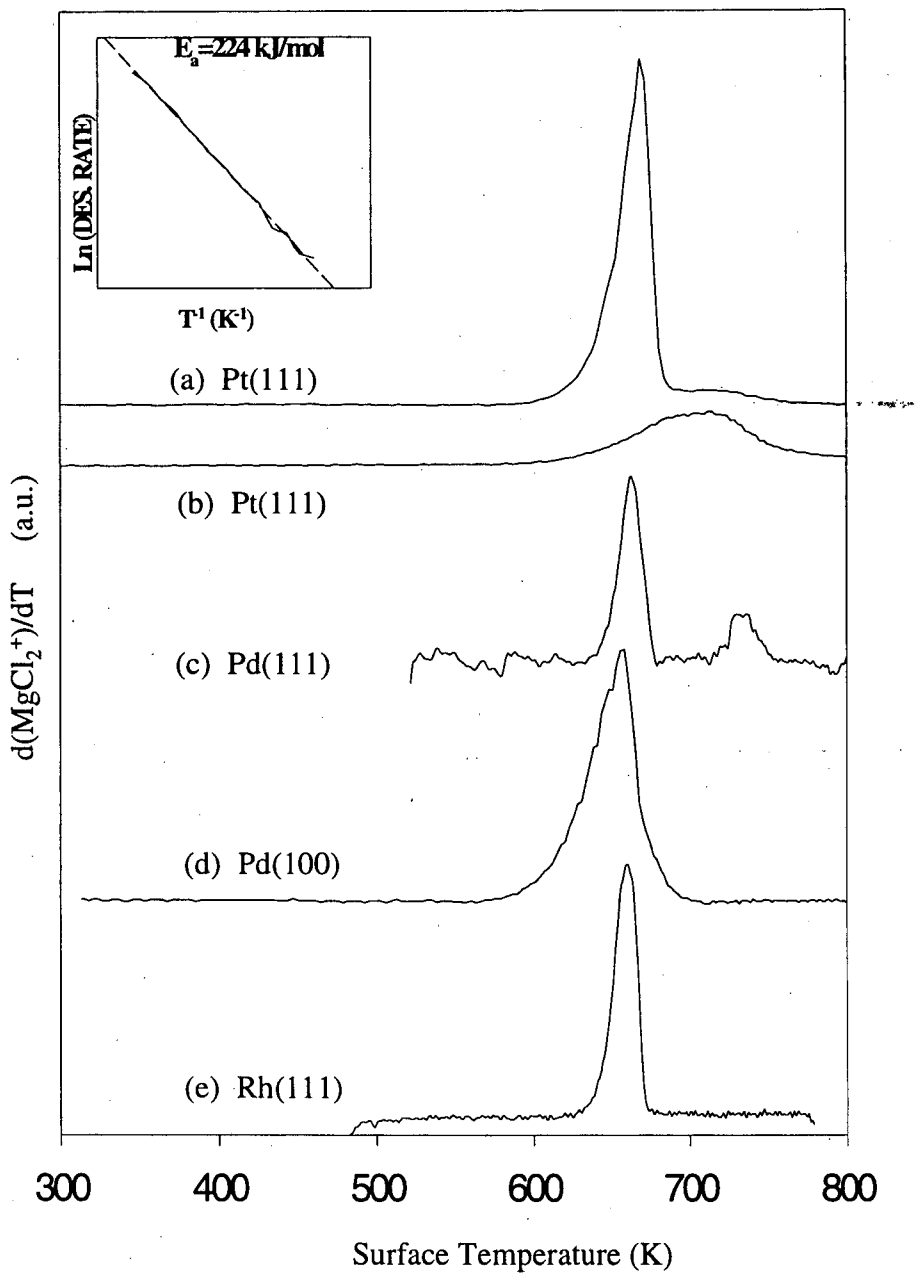

Fig. 8.1. Temperature Programmed Desorption profiles of $MgCl_2$ adsorbed on (a) Pt(111) at multilayer and (b) monolayer coverages, , (c) Pd(111), (d) Pd(100) and (e) Rh(111). The heating rate was calculated to be approximately 5 Ks^{-1}. Also shown in insert (top left) are the results of a leading edge analysis carried out on the lower temperature feature seen in (a) which yields an activation energy for desorption of 224 kJ/mol, assuming zero order kinetics.

The desorption profile monitored at m/e= 95-97, encompassing the $Mg^{35}Cl_2^+$ and $Mg^{35/37}Cl_2^+$ parent peaks, displays two distinct desorption features. The lower temperature peak, Fig. 8.1(a), exhibiting an exponential rise in the initial desorption rate with a sharp falling edge is characteristic of multilayer desorption. A leading-edge analysis (shown in the insert), assuming zero-order kinetics yields an activation energy for desorption of 224 kJ/mol. This result compares favorably with the heat of sublimation of bulk magnesium chloride, 238 kJ/mol [61]. The higher temperature feature, more clearly seen at lower $MgCl_2$ coverages (see Fig. 8.1(b)) and also evident on Pd(111) (Fig. 8.1(c)), displays first order kinetics with a characteristic asymmetric peak profile. However, compared to the TPD of $MgCl_2$ adsorbed on Pd(111), shown in Fig. 8.1(c), this higher temperature peak on Pt(111) exhibits a desorption temperature approximately 30 K lower. A measure of the relative stabilization of the monolayer states can be obtained by applying first order kinetics described in chapter three to both monolayer and multilayer states. Application of the Redhead equation using a pre-exponential of 10^{13} s and a heating rate of 5 K s^{-1} leads to the result that the monolayer states on Pd(111) and Pt(111) are stabilized above the monolayer by 17 and 8 kJ mol^{-1}, respectively [33].

Fig. 8.1(d) and (e) illustrate the TPD profiles obtained for similar $MgCl_2$ thin films grown on Pd(100) and Rh(111). A qualitatively similar profile was also

obtained for Pt(100)-hex. All of these TPD profiles exhibit a single peak consistent with zero order multilayer desorption analogous to the lower temperature peak observed on Pt(111) and Pd(111).

8.3.2 Auger Electron Spectroscopy (AES)

Fig. 8.2 shows AES of $MgCl_2$ thin films grown on Pd(111) at ≈600 K, corresponding to a temperature near the on-set of desorption of the multilayer (Fig. 8.1(a)). All of the spectral features observed can be identified with Pd, Mg and Cl AES transitions.

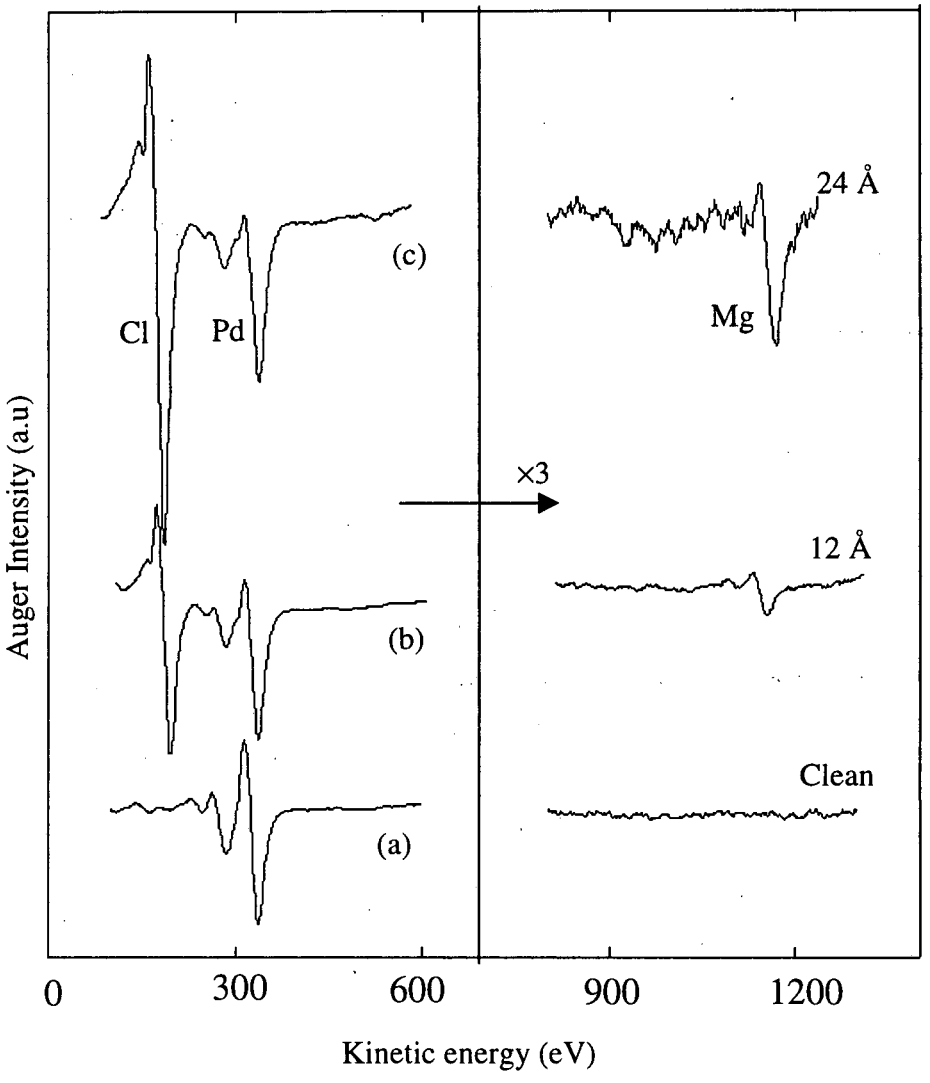

Fig. 8.2. Auger Electron Spectroscopy of (a) Clean Pd(111) and (b), (c) $MgCl_2$ ultra-thin films grown on Pd(111) shown as a function of increasing film thickness. Film thicknesses were calculated based on the signal attenuation of the Pd 333 eV signal upon $MgCl_2$ deposition. These spectra were taken using an emission current of 2 mA and a 3 keV primary energy.

From the attenuation of the Pd AES feature at 333 eV, the overlayer thicknesses in Fig. 8.2(b) and (c) were calculated to be 12 Å and 24 Å, respectively. AES measurements on Pd(111) indicate that, for the monolayer LEED patterns observed, the overlayer thickness was determined to be ≈6 Å in good qualitative agreement with the $MgCl_2$ unit cell dimension [72,78]. Based on the Cl-Mg-Cl trilayer thickness (≈ 5.9 Å) in conjunction with unit cell dimensions (Fig. 8.2 - insert) these results, in which no growth mechanism assumption is needed, suggest that growth occurs in a layer-by-layer fashion, consistent with the layered nature of bulk $MgCl_2$ [78]. This same growth mode has been seen for the growth of $MgCl_2$ thin films on Au, thus Fig. 8.2(b) and (c) correspond to two and four Cl-Mg-Cl layers respectively [75].

AES measurements also indicated that after $MgCl_2$ desorption, completed by 750 K, the surface was free from any signal associated with either Cl or Mg. Since Cl is known to be stable on these transition metal surfaces up until >750 K, the lack of any AES signal attributable to Cl indicates that vapor phase deposition of $MgCl_2$ does not lead to any measurable (<1%) dissociative adsorption on the surfaces used in the present study [83].

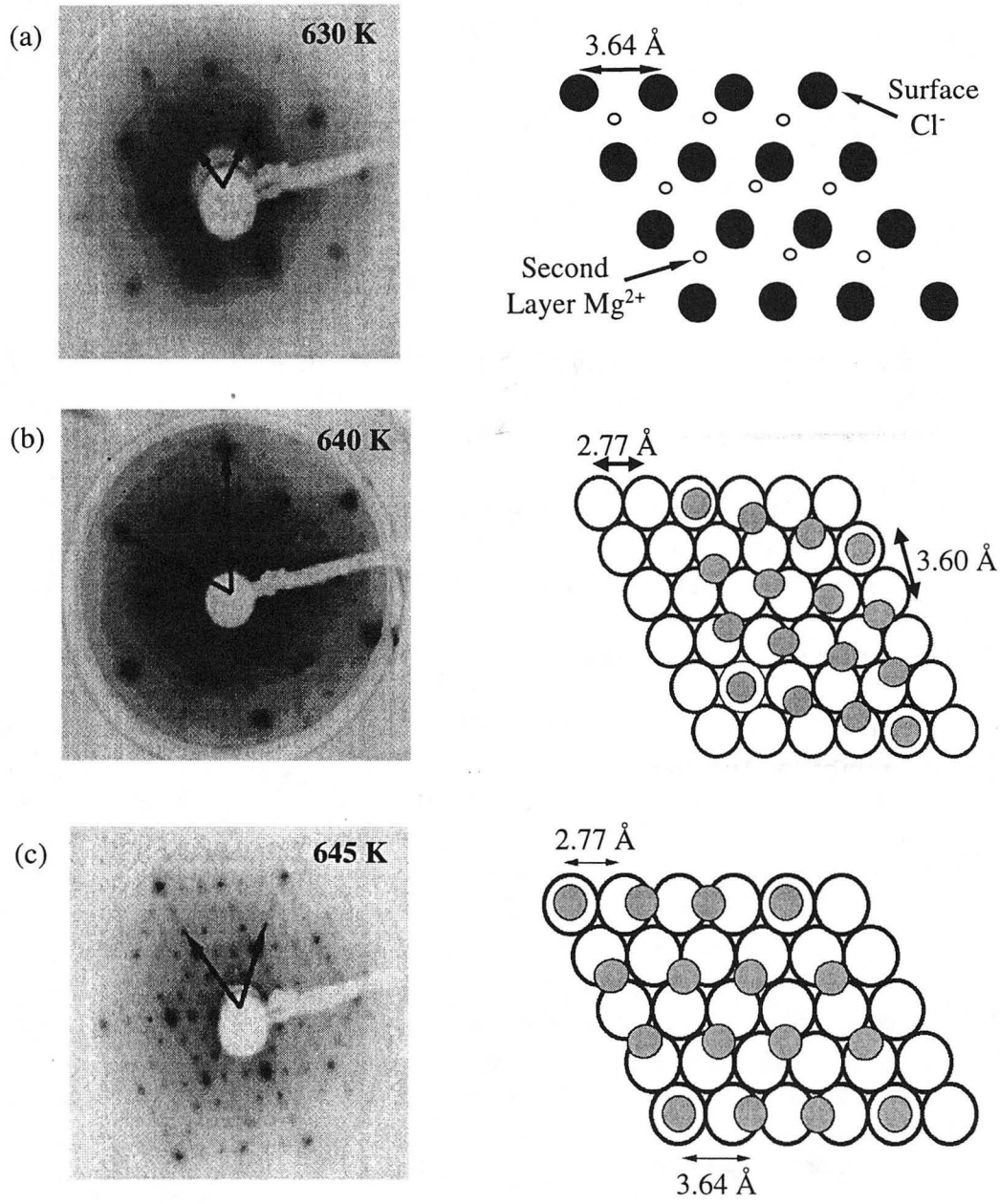

Fig. 8.3. LEED patterns and associated real space schematics for $MgCl_2$ grown on Pt(111) at multilayer and monolayer coverages. (a) Hexagonal multilayer pattern recorded at an incident energy of 105eV and corresponding bulk $MgCl_2$. Note that in the real space structure only the basal plane Cl^- and the second layer Mg^{2+} are shown for clarity. (b) Monolayer ($\sqrt{13}$ x $\sqrt{13}$) R13.9° LEED pattern recorded at an incident energy of 45 eV along with the real space structure showing the $MgCl_2$ unit cell compression and 13.9° rotation between the $MgCl_2$ and Pt(111) unit cells.(c) (4 x 4) LEED pattern recorded at an incident energy of 105eV and associated real space structure showing the $MgCl_2$ unit cell. Note that in (b) and (c) only the basal plane Cl^- (filled circles), reduced in size for clarity, along with the Pt(111) surface atoms (hollow circles) are shown.

8.3.3 LEED Observations

8.3.3.1 Pt(111)/Pd(111)

Fig. 8.3 (a)-(c) show various LEED images, corresponding to multilayer (a) and monolayer (b) and (c) coverages, along with their real space structures and annealing temperature for the case of $MgCl_2$ on Pt(111). The definition of a monolayer is defined as any structure which consists of a single Cl-Mg-Cl trilayer. The existence of a monolayer structure was determined by LEED in the form of a diffraction pattern complicated by multiple diffraction events and by the determination of film thickness by AES signal attenuation of the substrate peaks. At a Pt(111) temperature of 630 K, exposure to the $MgCl_2$ source for 30 minutes leads to the production of a hexagonal multilayer LEED pattern shown in Fig. 8.3(a), where the overlayer unit cell vectors are oriented parallel to those of the underlying substrate (cf. Fig. 8.3(a) and Fig. 8.3(c)). Due to the finite sampling depth of the elastically scattered electrons, the overlayer thickness is sufficient to remove any contribution to the LEED pattern from the underlying Pt(111). By exploiting the inverse relationship between the radial positions of the diffraction spots to the length of the real space unit cell vectors, the multilayer unit cell dimension was determined to be in the range of 3.6-3.7 Å. A qualitative I-V curve comparison of this overlayer structure to the multilayer structure described

in chapter seven revealed that the overlayer is the (0001) face of α-$MgCl_2$. Upon flashing to a temperature of 635 K, the multilayer pattern is replaced by a $\left(\sqrt{13}\times\sqrt{13}\right)$ R 13.9° monolayer pattern, shown in Fig. 8.3(b) [76]. In this structure, the $MgCl_2$ unit cell angles are preserved in their bulk values, but the lattice constant of the surface unit cell has been decreased to 3.34 Å versus 3.64 Å in the bulk. The complicated LEED pattern is a consequence of the rotation of the monolayer unit cell by 13.9° with respect to the underlying Pt(111) substrate (Fig. 8.3(b)) and a resulting symmetrically equivalent domain. Additional annealing of the Pt(111) to 645 K for 1 min produces a well-defined (4×4) pattern, shown in Fig. 8.3(c), which corresponds to a single trilayer (Cl-Mg-Cl) of the $MgCl_2$ bulk unit cell in which the unit cell lies parallel to that of the underlying substrate. The unit cell is the same as seen in the multilayer structure, but multiple scattering events from the substrate-adsorbate 4:3 coincidence lattice produces the (4×4) pattern. This proposed structure also correlates with the fact that the $\left(\sqrt{13}\times\sqrt{13}\right)$ R 13.9° structure involves a $MgCl_2$ lattice compression causing it to be observed at a lower surface temperature, associated with a higher $MgCl_2$ coverage, compared to the (4×4) structure. Upon annealing the surface to >770 K, $MgCl_2$ desorption is complete and the hexagonal LEED pattern of the clean Pt(111) substrate is recovered.

8.3.3.2 Pt(100)-hex

In order to minimize the total free energy, the clean Pt(100) undergoes a surface reconstruction in UHV to produce a quasi-hexagonal overlayer [1]. As a result of the different symmetry present at the surface compared to that in the bulk, this reconstruction gives rise to a complicated $\begin{pmatrix} 14 & 1 \\ -1 & 5 \end{pmatrix}$ LEED pattern. This hexagonal surface has a unit cell dimension identical to that of Pt(111), although He scattering studies indicate that the surface is considerably more corrugated than its Pt(111) counterpart [84].

Deposition of $MgCl_2$ on this surface, at a temperature on the edge of the multilayer desorption peak (≈600 K), yields the pattern shown in Fig. 8.4(a). Analysis of the position of the radial diffraction beams associated with the overlayer with respect to the underlying Pt(100)-hex surface indicates a unit cell dimension of between 3.6-3.7 Å, consistent with the size of the $MgCl_2$ unit cell. The LEED image shown in Fig. 8.4(a) can be decomposed into a ring of diffuse intensity, associated with rotationally disordered film growth superimposed on a symmetric 24-spot pattern.

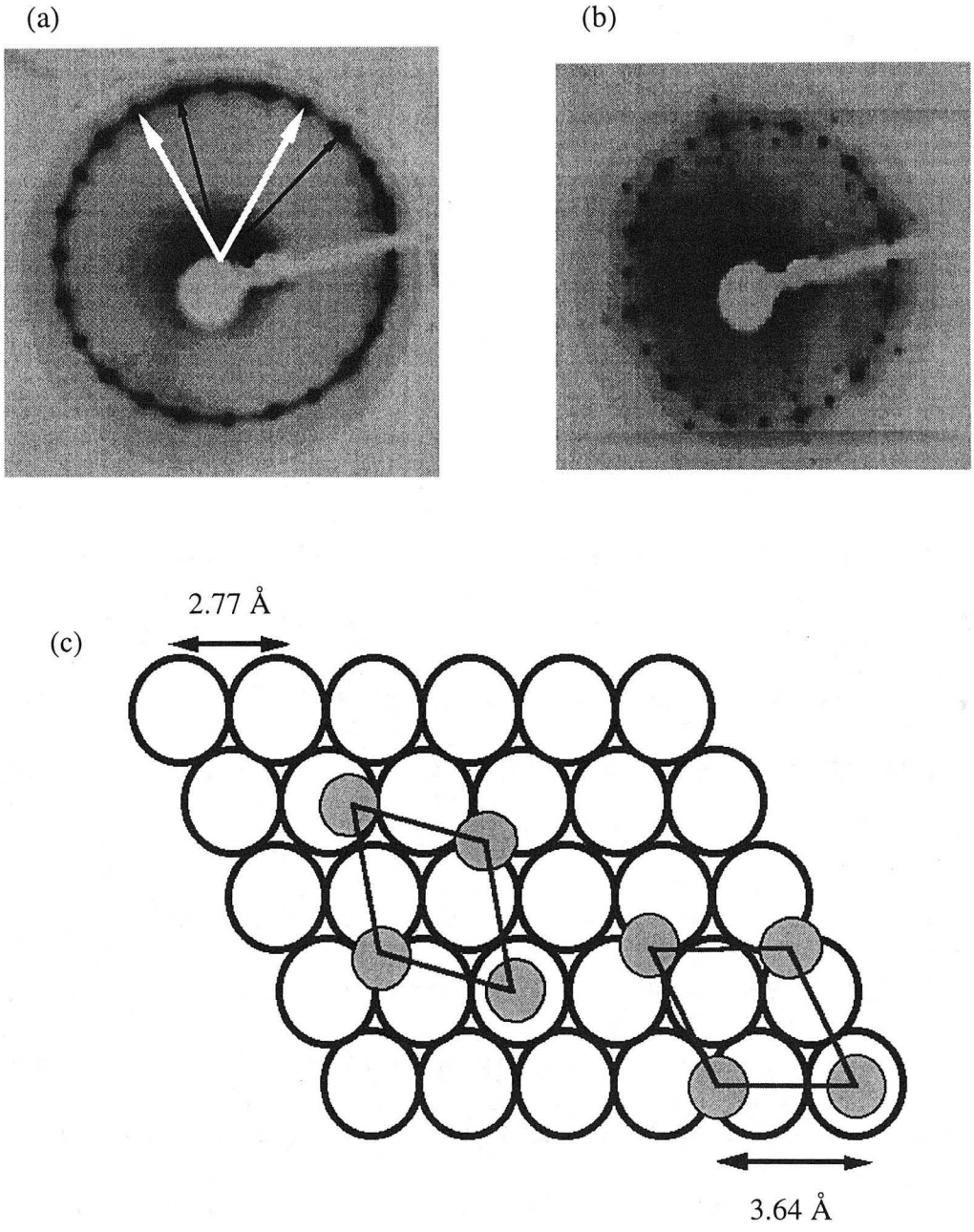

Fig. 8.4. LEED patterns of $MgCl_2$ grown on Pt(100)-hex (a) Multilayer structure recorded at an incident energy of 30eV, showing the two symmetrically inequivalent $MgCl_2$ reciprocal space lattices. (b) Single layer of $MgCl_2$ showing the presence of the underlying reconstructed surface reconstruction recorded at an incident energy of 38eV. (c) represent possible real space structural schematic of $MgCl_2$ illustrating the reciprocal lattices seen in (a). Note that only the basal plane Cl^- (filled circles), reduced in size for clarity, along with the Pt(100)-hex surface atoms (hollow circles) are shown.

Fig. 8.4(b) shows the LEED pattern recorded after annealing to 630K. By means of $MgCl_2$ thermal desorption, this process generates a LEED pattern which is a superposition of the reconstructed Pt(100) and multilayer pattern. Fig. 8.4(b) also indicates that the 24-spot pattern can in fact be deconvoluted into a superposition of two independent 12-spot patterns. The underlying substrate LEED pattern is the $\begin{pmatrix} 14 & 1 \\ -1 & 5 \end{pmatrix}$, characteristic of the reconstructed Pt(100) surface. Fig. 8.4(b) enables the relative orientation of the $MgCl_2$ unit cells associated with the different domains to be identified with respect to the Pt surface mesh. The results of this analysis are shown schematically in Fig. 8.4 (c), in which two distinct symmetry inequivalent domains of $MgCl_2$ occur, each associated with a hexagonal LEED pattern, both parallel to and intersecting the principal axis of the surface lattice. Such a result is not expected if the reconstruction is lifted in Pt(100) leaving a one domain square surface, since on Pd(100), to be discussed later, which has the same symmetry as unreconstructed Pt(100) and a similar lattice constant, only one symmetry inequivalent domain was observed. Based on their relative spot intensity (Fig. 8.4(b)), each $MgCl_2$ surface domain appears to be roughly equally populated. Each separate domain has a symmetrically equivalent set of diffraction spots rotated by 90°, associated with the presence of two rotationally distinct, but isoenergetic domains caused by the Pt(100) surface reconstruction. Thus, these two distinct $MgCl_2$ domains (Fig. 8.4(b) and

(c)),which give rise to a separate hexagonal LEED pattern, coupled with the two underlying Pt(100)-hex surface domains yields the observed 24-spot LEED pattern.

8.3.3.3 Pd(100)

Unlike Pt(100), Pd(100) does not undergo any UHV surface reconstruction, consequently the square lattice associated with the face centered cubic array of surface atoms is maintained at the surface [85]. In addition, the Pd-Pd nearest neighbor distance (2.78 Å) is the same as the (111) analogue. The LEED pattern associated with the clean surface and multilayer $MgCl_2$ grown at a temperature of 620 K, are shown in Figs. 8.5 (a) and (c), respectively. The LEED image shown in Fig. 8.5 (c) and the corresponding less than a multilayer pattern shown in Fig. 8.5(b) can be deconvoluted into a relatively weak diffuse ring, associated with rotationally disordered $MgCl_2$, superimposed on a distinct 12-spot diffraction pattern. Radial analysis of the overlayer confirms a real space dimension (3.6-3.7 Å) consistent with the $MgCl_2$ unit cell dimension. Two domains of $MgCl_2$ growth are necessary in describing the multilayer and monolayer diffraction pattern shown in Fig. 8.5(c) and 8.5(b) respectively. These two domains are symmetrically equivalent and exist as the result of the geometric mismatch between the hexagonal multilayer and the square surface of Pt(100) (Fig. 8.6(b)). Subsequent annealing of this multilayer structure to ≈630K produces the monolayer shown in Fig. 8.5(b).

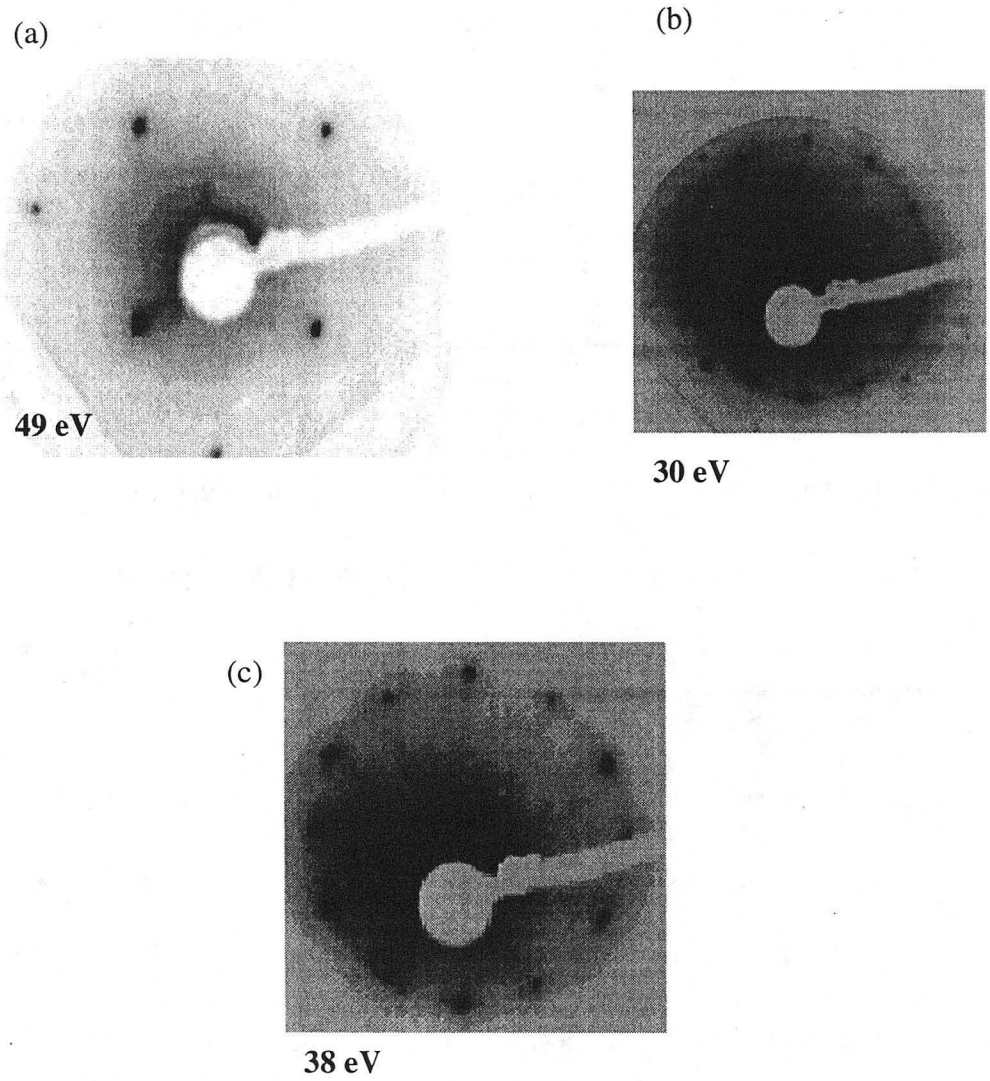

Fig. 8.5. (a) LEED pattern associated with clean Pd(100) recorded at 49 eV. (b) and (c) LEED patterns from monolayer and multilayer $MgCl_2$ recorded at 30 eV and 38 eV showing the presence of both ordered and rotationally disordered domains.

(a)

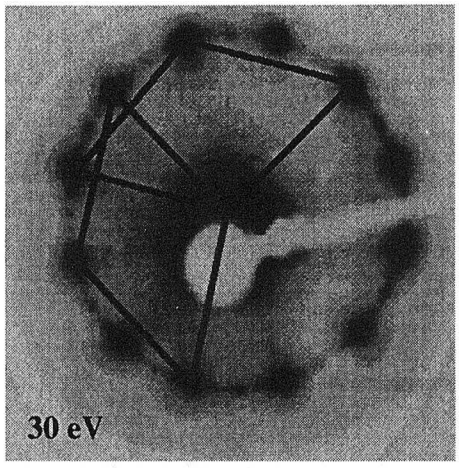

(b)

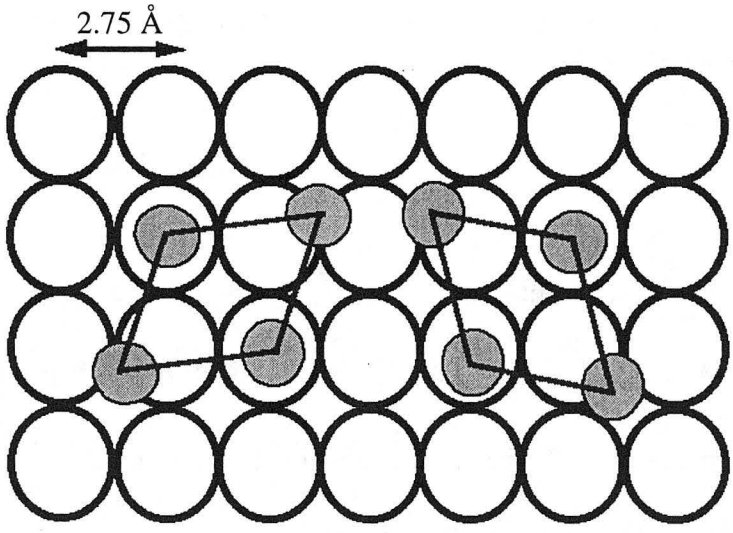

Fig. 8.6. (a) LEED pattern of the $MgCl_2$ multilayer on Pd(100) with the two symmetry equivalent unit cells indicated (b) Real space structural schematic associated the multilayer pattern in (a). Note that only the basal plane Cl^- (filled circles), reduced in size for clarity, along with the Pd(100) surface atoms (hollow circles) are shown.

This represents the same structure observed for the multilayer but now corresponding to only a single $MgCl_2$ layer thickness.

8.3.3.4 Rh(111)

The growth of $MgCl_2$ on Rh(111) produced two distinctly different multilayer structures under identical deposition conditions whose LEED images are shown in Fig. 8.7(a)-(b). Both structures were generated in separate experiments by depositing $MgCl_2$ at a substrate temperature of ≈600 K. For reference, the clean Rh(111) diffraction pattern is also shown in Fig. 8.7(c). Analysis of the radial position associated with the multilayer intensity reveals that in both Fig. 8.7(a) and (b):

$$a_{MgCl_2} \approx \frac{4}{3} \cdot a_{Rh(111)}$$

(where a is the unit cell dimension) consistent with the relative size of the respective unit cells (a_{MgCl_2} = 3.64 Å and $a_{Rh(111)}$ = 2.69 Å) [86]. For the ordered multilayer shown in Fig. 8.7(b), a comparison with the clean Rh(111) (Fig. 8.7(c)) shows that, unlike the situation observed on Pt(111) and Pd(111), the hexagonal (1×1) multilayer on Rh(111) grows with its unit cell vectors rotated 45° with respect to those of the underlying Rh(111) surface unit cell (Fig. 8.7(d)).

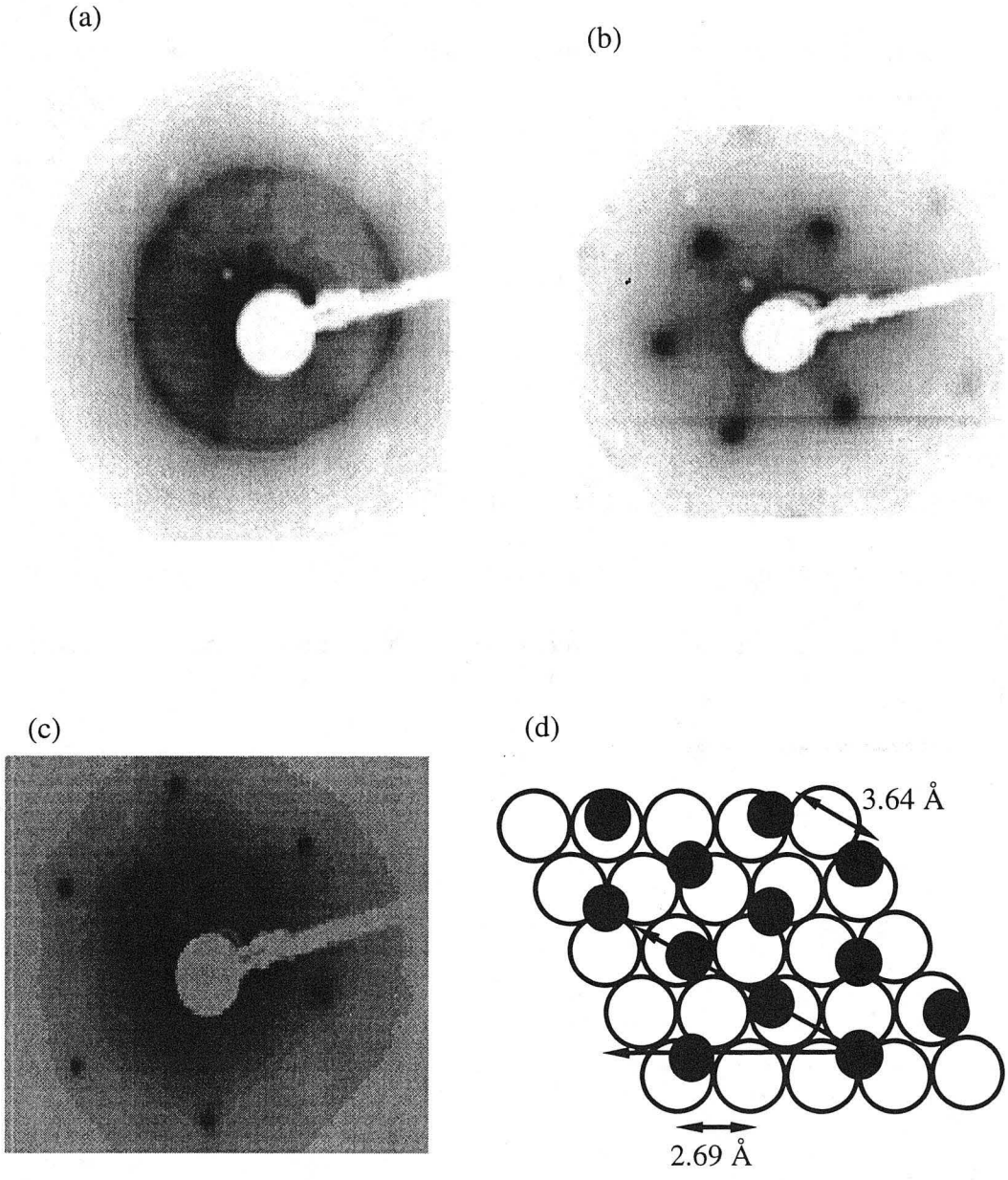

Fig. 8.7. LEED patterns of (a) rotationally disordered $MgCl_2$ multilayer on Rh(111) recorded at an incident energy of 38 eV with the radial distance determined to be between 3.6-3.7Å, corresponding to the unit cell of $MgCl_2$ (b) Hexagonally ordered $MgCl_2$ multilayer recorded at an incident energy of 73 eV and (c) clean Rh(111) recorded at an incident energy of 71 eV. The $MgCl_2$ unit cell orientation can be seen to bisect that of the surface mesh. (d) Possible real space structure corresponding to (b) in which only the basal plane Cl^- (filled circles), reduced in size for clarity, along with the Rh(111) surface atoms (hollow circles) are shown.

The ring-like LEED pattern shown in Fig. 8.7(a), characteristic of rotationally disordered multilayer $MgCl_2$ growth, was also observed upon deposition of multilayer $MgCl_2$ on Rh(111). Despite the production of an ordered multilayer on Rh(111) upon annealing this structure, the only change in the LEED images shown in Fig. 8.7(b) and (a) is a decrease in the $MgCl_2$ spot intensity and a resulting rise in the Rh(111) hexagonal spot profile as the adsorbate is thermally desorbed.

Table 8.1 summarizes the effect of surface structure on the relative monolayer stabilization energy of $MgCl_2$, with respect to the multilayer, along with the LEED structures observed at both multilayer and monolayer coverages.

Surface	Monolayer Stabilization (kJ mol^{-1})	Multilayer Structure(s)	Monolayer Structure(s)
Pt(111)	8	(1 x 1) ordered hexagonal structure	(4 x4) ($\sqrt{13}$ x $\sqrt{13}$) R13.9°
Pt(100)-hex	0	Significant rotational disorder and two ordered domains	Significant rotational disorder and two ordered domains
Pd(111)	17	(1 x 1) ordered hexagonal structure	(4 x 4) ($\sqrt{13}$ x $\sqrt{13}$) R13.9°
Pd(100)	0	Some rotational disorder and two symmetrically equivalent domains	Some rotational disorder and two symmetrically equivalent domains
Rh(111)	0	(1 x 1) ordered hexagonal and complete rotationally disordered structures	(1 x 1) ordered hexagonal and complete rotationally disordered structures

Table 8.1. Summary of the LEED and TPD observations for the adsorption of $MgCl_2$ on the various substrates..

8.4 DISCUSSION

The results presented in Section (III) clearly point to the significant role of the transition metal surfaces in controlling $MgCl_2$ growth at both monolayer and multilayer coverages (See Table 8.1). In order to understand the substrate role, it

is useful to examine the $MgCl_2$ unit cell in context with the various transition metal surfaces. For the adsorbate, $MgCl_2$, the unit cell is orthorhombic with a 60° angle between the unit cell vectors whose length is 3.64 Å.

Experimental observations have indicated a strong correlation between the degree of the adsorbate-substrate lattice match (including unit cell vector geometry and magnitude) and the strength of the adsorbate-substrate interaction as measured by TPD.

Both Pd(111) and Pt(111) surfaces present a hexagonal close packed array of atoms with an angle between the unit cell vectors of 60° to the adsorbate (see Fig. 8.3(c)). Comparing the unit cell dimensions of the substrate and adsorbate:

$$a_{Pt(111)} = 2.78 \text{ Å}, \; a_{Pd(111)} = 2.75 \text{ Å and } \; a_{MgCl_2} = 3.64 \text{ Å}$$

It can be seen that there exists a coincidence lattice match between the substrates and the $MgCl_2$ such that

$$4 \cdot a_{Pt(111)/Pd(111)} = 3 \cdot a_{MgCl_2}$$

with only a lattice mismatch of <1.6% on either surface. Fig. 8.3(c) illustrates a real space schematic corresponding to the (4×4) LEED pattern for the case of Pt(111), although it should be noted that this figure is for illustrative purposes only. At slightly higher monolayer coverages (≈25%), the $\left(\sqrt{13}\times\sqrt{13}\right)$ R 13.9° structure is observed. The $MgCl_2$ unit cell vectors are rotated by 13.9° with respect to those of the underlying Pt(111) or Pd(111) substrate, Fig. 8.3(b), and a significant contraction of ≈0.3 Å in the $MgCl_2$ unit cell dimension is associated

with this monolayer structure. Such a significant modification to the overlayer has not to our knowledge been observed previously in the heteroepitaxy of alkali earth halides and demonstrates a considerable adsorbate-substrate interaction.

It appears that the significant adsorbate-substrate interactions between the Pt(111) or Pd(111) surfaces and the $MgCl_2$ monolayer are responsible for both the compression of the $MgCl_2$ unit cells in the case of the $\left(\sqrt{13}\times\sqrt{13}\right)$ R 13.9° monolayer LEED structures. The $MgCl_2$ unit cell, at least for monolayer coverages, appears to exhibit a degree of "flexibility" in the presence of sufficient interaction with the underlying surface atoms. Fig. 8.3(b) shows the real space orientation of the $\left(\sqrt{13}\times\sqrt{13}\right)$ R 13.9° structure, again this diagram is for illustration purposes only. The most significant effect of this interaction is the unit cell contraction in the $\left(\sqrt{13}\times\sqrt{13}\right)$ R 13.9° which implies a significant degree of charge transfer between the basal plane Cl^- and the surface Pd or Pt atoms, to reduce the $MgCl_2$ unit cell dimension. However, this compression allows the monolayer surface coverage of $MgCl_2$ in the $\left(\sqrt{13}\times\sqrt{13}\right)$ R 13.9° structure to extend above that predicted from the bulk unit cell dimension, as a result increasing the density of the monolayer adsorbate-substrate interactions. The existence of these interactions on both surfaces is also evidenced by the TPD data which reveal the presence of distinct monolayer desorption peaks displaced to higher temperatures than the multilayer desorption feature. Since the multilayer desorption peak provides a measure of the cohesive forces within the $MgCl_2$

lattice itself, the presence of higher temperature states is a reflection of the stabilization of the $MgCl_2$ at monolayer coverages through interactions with the underlying surface atoms. This hypothesis was confirmed on both Pt(111) and Pd(111) by carrying out $MgCl_2$ deposition at 650 K, a temperature corresponding to a point where there is total multilayer desorption, but before monolayer desorption occurs. At this temperature, the $\left(\sqrt{13}\times\sqrt{13}\right)$ R 13.9° structure is generated directly with prolonged exposure in production of a multilayer (1×1) pattern.

At multilayer coverages, analysis of the (1×1) LEED pattern reveals that the $MgCl_2$ unit cell dimension reverts back to the ionic solid with the crystallographic orientation remaining parallel to the Pd(111) or Pt(111) substrate, see Fig. 8.3(a). Since no additional information has been found in determining if the monolayer structure below the multilayer $MgCl_2$ film is the (4×4) or the $\left(\sqrt{13}\times\sqrt{13}\right)$ R 13.9°, the same conclusions about this subject discussed in chapter seven are relevant for the $MgCl_2$ on Pt(111) case.

On Pt(100), the two dimensional surface overview is identical to that of the Pt(111) analogue with a hexagonal surface unit cell and a 2.78 Å Pt-Pt nearest neighbor distance, but with a surface corrugation of 0.6 Å. However, Table 8.1 shows that compared to Pt(111) and Pd(111), the adsorbate-substrate interaction of monolayer $MgCl_2$ on Pt(100) is diminished to a magnitude that renders any monolayer feature indistinguishable from the multilayer desorption peak. The

reduction in the strength of these interactions is clearly seen in the monolayer and multilayer growth characteristics. Multilayer and monolayer $MgCl_2$ LEED patterns on Pt(100)-hex, shown in Fig. 8.4(a) and (b), exhibit ring patterns associated with rotational disordered $MgCl_2$. Such a structure indicates that on this surface, in contrast to Pt(111) and Pd(111), the energetic preference for a specific $MgCl_2$ unit cell orientation with respect to the underlying surface mesh, indicative of the adsorbate-substrate interaction strength, is far less pronounced. However, a degree of interaction between $MgCl_2$ and Pt(100)-hex is retained as evidenced by the existence of two ordered $MgCl_2$ domains, whose unit cell lattice vectors are shown as (a) and (b) in Fig. 8.4(a). The reduction in adsorbate-substrate interaction strength is also consistent with the lack of any commensurate monolayer LEED patterns corresponding to changes in the $MgCl_2$ unit cell. This is particularly striking in the case of the real space structure shown in Fig. 8.4(c) in which the $MgCl_2$ unit cell is oriented parallel to the Pt(100)-hex unit cell vectors analogous to the monolayer structure on Pt(111). In contrast to growth on Pt(111), despite the identical two dimensional surface overview on both Pt(111) and Pt(100)-hex, there is no evidence for the production of a commensurate (4×4) or the $\left(\sqrt{13}\times\sqrt{13}\right)$ R 13.9° monolayer structure on Pt(100)-hex. These data clearly indicate that the adsorbate-substrate interaction is strongly influenced by the surface corrugation and/or the underlying second layer (100) Pt atoms.

On Pd(100), TPD measurements shown in Fig. 8.1 indicate that, like Pt(100)-hex, the strength of any adsorbate-substrate interaction is significantly reduced compared to Pt(111) and Pd(111) surfaces. This is seen in the multilayer and monolayer structures by the existence of rotational disorder. However, in a similar fashion to Pt(100)-hex, the presence of a preferred $MgCl_2$ unit cell domain on the Pd(100) surface manifested in the ordered diffraction spots indicates a measure of adsorbate-substrate interaction. When compared to results obtained on Pt(111) and Pd(111), the identical monolayer and multilayer $MgCl_2$ structures, Fig. 8.5(a) and (b), obtained on Pd(100) is also consistent with the reduction in the monolayer adsorbate-substrate interaction strength.

The results presented suggest that the factors responsible for ordered/disordered $MgCl_2$ growth on Rh(111) are different compared to the other transition metal surfaces studied. Although the TPD measurements (Fig. 8.1) do not indicate any significant monolayer adsorbate-substrate interaction, $MgCl_2$ deposition under similar temperature conditions to those used on the other transition metal surfaces is observed to produce a fully ordered (1×1) multilayer $MgCl_2$ structure. However, the corresponding monolayer structure does not exhibit any commensurate surface structures, such as the (4×4) seen on Pt(111) and Pd(111), which have been associated with modifications in the $MgCl_2$ unit cell induced by significant monolayer adsorbate-substrate interactions. Furthermore, it is the presence of a commensurate monolayer patterns on Pt and

Pd surfaces that appear to be the necessary template for subsequent ordered multilayer $MgCl_2$ growth. Furthermore, the hexagonal (1×1) multilayer (Fig. 8.7(b)) structure grows in such a way that its lattice vectors are rotated by 45° with respect to those of the underlying Rh(111) surface in contrast to what is seen on Pd(111) and Pt(111) and despite the fact there is no approximate lattice match between adsorbate and substrate for this orientation. In addition, separate experiments produced a rotationally disordered structure (Fig. 8.7(a)), associated with a lack of energetic preference for any specific orientation, and by analogy to Pt(100)-hex and Pd(100), weaker monolayer adsorbate-substrate interactions. It remains unclear as to why $MgCl_2$ multilayers exhibiting characteristics of both rotational disorder and ordered domains were not simultaneously observed in a single deposition. Indeed, it appears that the factors responsible for ordered multilayer and monolayer $MgCl_2$ growth may be intrinsically different on Rh(111) compared to the other transition metal surfaces employed in this study, possibly as the result of a greater sensitivity to the exact crystal temperature during growth.

In terms of the explicit substrate role, significant adsorbate-substrate interactions exist on all of the surfaces studied, as evidenced by a degree of $MgCl_2$ ordering in each case. The data presented in this study clearly point to the fact that it is the magnitude of these substrate dependent interactions, which are directly correlated with the degree of ordering at both monolayer and multilayer $MgCl_2$ coverages. For the Pt and Pd surfaces studied, an initial condition for obtaining ordered structures appears to be that where the crystallography of the

surface mesh and the surface topography match that of the hexagonal $MgCl_2$ unit cell the greatest adsorbate-substrate interactions exist, therefore providing the best template for ordered growth. The topographical requirement is illustrated by the difference in the $MgCl_2$ multilayer structures obtained on Pt(111) and Pt(100)-hex, where Pt(111) exhibits a greater adsorbate-substrate interaction strength, thus generating ordered $MgCl_2$ monolayer and multilayer structures. The importance of matching the crystallography between adsorbate and substrate is seen in the comparison of the $MgCl_2$ structures grown on Pt(111) and Pt(100) (Figs. 8.3(a) and 8.7(c)). Experimentally, the lower monolayer adsorbate-substrate interaction strength on Pd(100) , shown in Fig. 8.1 by the lack of a distinct monolayer state, manifests itself as an increase of rotational disorder in the multilayer LEED patterns produced on Pt(100).

The influence of geometry is better illustrated by the identical LEED patterns obtained on Pt(111) and Pd(111), with their similarity in surface symmetry and unit cell dimension, despite significant differences in their chemical properties. Overall, the results presented point to the fact that a careful consideration of the relative crystallography and unit cell dimension between the adsorbate and the substrate can be important in controlling ordered epitaxial growth of a thin film based on the strength of adsorbate-substrate interactions at monolayer coverages. However, the structural data obtained on Rh(111) imply that chemical identity can be important in determining the factors responsible for ordered monolayer and multilayer growth. On all of the surfaces studied, TPD

experiments are seen to serve as a useful diagnostic for both determining the optimum multilayer growth conditions and the existence of sufficiently strong adsorbate-substrate interactions manifested in distinct monolayer states which are correlated with subsequent ordered multilayer growth.

8.5 CONCLUSIONS

The monolayer and multilayer structure of $MgCl_2$ on a variety of transition metal single crystal surfaces (Pd(111) and (100), Pt(111) and (100)-hex and Rh(111)) has been studied using LEED and TPD. The substrate geometry has been found to be important in controlling the growth characteristics of $MgCl_2$ at both monolayer and multilayer coverages, as seen in the strength of the adsorbate-substrate interaction at monolayer coverages. The magnitude of these interactions, which are found to depend on the geometrical matching between adsorbate and substrate unit cells, determine the degree of ordering at the monolayer which acts as a template for multilayer and/or thin film growth. On Pt(111) and Pd(111), significant adsorbate interactions are observed, thus producing distinct monolayer states as evidenced by TPD. As a direct result of this interaction strength, identical, reproducibly well ordered LEED structures at both monolayer and multilayer coverages were observed on both surfaces. On both Pd(100) and Pt(100)-hex, the adsorbate-substrate interactions were reduced

compared to Pt(111) and Pd(111) surfaces. Consequently, $MgCl_2$ growth on Pt(100)-hex and Pd(100) exhibited more complex multilayer and monolayer LEED patterns associated with various degrees of ordered and rotationally disordered $MgCl_2$ domains. Experiments on Rh(111) indicate that the factors responsible for ordered $MgCl_2$ growth on this surface differ from those observed on Pt and Pd single crystals.

Bibliography

[1] M. A Van Hove, R. J. Kostner, P. C. Stair, J. P. Biberian, L. L. Kesmodel, I. Bartos and G. A. Somorjai, *Surf. Sci.* **103** (1981) 189.

[2] M. A. Van Hove, W. H. Weinberg and C.-M. Chan, *Low-Energy Electron Diffraction* Springer, Berlin, 1986.

[3] G. A. Somorjai, *Chemistry in Two Dimensions: Surfaces* Cornell University Press, Ithaca, 1981.

[4] H. A. Yoon, N. Materer, M. Salmeron, M. A. Van Hove and G. A. Somorjai, *Surf. Sci.* **376** (1997) 254.

[5] M. A. Van Hove and S. Y. Tong, *Surface Crystallography by LEED: Theory, Computation and Structural Results* Springer-Verlag, Berlin, 1979.

[6] M. A. Van Hove, W. Moritz, H. Over, P. J. Rous, A. Wander, A. Barbieri, N. Materer, U. Starke, D. Jentz, J. M. Powers, G. Held and G. A. Somorjai, *Surf. Sci.* **287/288** (1993) 432.

[7] M. A. Van Hove, W. Moritz, H. Over, P. J. Rous, A. Wander, A. Barbieri, N. Materer, U. Starke and G. A. Somorjai, *Surf. Sci. Rep.* **19** (1993) 191.

[8] P. J. Rous, M. A. Van Hove and G. A. Somorjai, *Surf. Sci.* **226** (1990) 15.

[9] P. J. Rous, *Prog. Surf. Sci.* **39** (1992) 3.

[10] D. F. Ogletree and G. A. Somorjai, *Rev. Sci. Instrum.* **57** (1986) 3014.

[11] D. F. Ogletree, G. S. Blackman, R. Q. Hwang, U. Starke, G. A. Somorjai and J. E. Katz, *Rev. Sci. Instrum.* **63** (1991) 104.

[12] P. R. Watson, M. A. Van Hove and K. Hermann, *Atlas of Surface Structures: Volume 1A* U. S. Secretary of Commerce (1994).

[13] A. Barbieri, W. Weiss, M. A. Van Hove and G. A. Somorjai, *Surf. Sci.* **302** (1994) 259.

[14] D. Rieger, F. J. Himpsel, U. O. Karlsson, F. R. McFeely, J. F. Moror and J. A. Yarmoff, *Phys. Rev. B* **34** (1986) 7295.

[15] Th. Gog, G. C. Follis and S. M. Durbin, *Appl. Surf. Sci.* **81** (1994) 485.

[16] H. C. Allen, J. M. Laux, R. Vogt, B. J. Finlayson-Pitts and J. C. Hemminger, *J. Phys. Chem.* **100** (1996) 6371.

[17] J. M. Laux, J. C. Hemminger and B. J. Finlayson-Pitts, *Geophys. Res. Lett.* **21** (1994) 1623.

[18] L. W. Bruch, A. Glebov, J. P. Toennies and H. Weiss, *J. Chem. Phys.* **103** (1995) 5109.

[19] D. P. Taylor, W. P. Hess and M. I. McCarthy, *J. Chem. Phys. B* **101** (1997) 7455.

[20] F. F. Fenter, F. Caloz and M. J. Rossi, *J. Phys. Chem.* **100** (1996) 1008.

[21] C. J. Davisson and L. H. Germer, *Phys. Rev.* **30** (1927) 705.

[22] R. A. Alberty and R. J. Silbey, *Physical Chemistry* John Wiley & Sons, 1st ed., 1992.

[23] D. P. Woodruff and T. A. Delchar, *Modern Techniques of Surface Science* Cambridge University Press, 2nd ed., 1994.

[24] G. Ertl and J. Kuppers, *Low Energy Electrons and Surface Chemistry* VCH, 2nd ed., 1985.

[25] N. W. Ashcroft and N. D. Mermin, *Solid State Physics*, Saunders College Publishing, Fort Worth, TX, 1976.

[26] Omicron Associates, *Instruction Manual: Spectraleed Optics and Electron Gun Ver 2.9* 1990.

[27] D. W. Jentz, Ph.D. thesis, UC Berkeley, 1992.

[28] J. B. Pendry, *Low-Energy Electron Diffraction* London: Academic Press, 1974.

[29] J. B. Pendry, *J. Phys. C* **13** (1980) 937.

[30] P. J. Rous and J. B. Pendry, *Phys. Rev. Lett.* **57** (1986) 2951.

[31] J. F. O'Hanlon, *A. User's Guide to Vacuum Technology* John Wiley & Sons, 1989.

[32] J. M. Powers, A. Wander, P. J. Rous, M. A. Van Hove and G. A. Somorjai, *Phys. Rev. B* **44** (1991) 11159.

[33] P. A. Redhead, *Vacuum* **12** (1962) 203.

[34] R. I. Masel, *Principles of Adsorption and Reactions on Solid Surfaces* John Wiley & Sons (1996).

[35] W. Heppler, *Crystal Preparation at LBL: 1976-1986* LBL.

[36] N. F. Ramsey, *Molecular Beams* Clarendon Press, Oxford (1963).

[37] G. M. Rothberg, M. Eisenstadt and P. Kusch, *J. Chem. Phys.* **30** (1959) 517.

[38] R. C. Miller and P. Kusch, *J. Chem. Phys.* **25** (1956) 860.

[39] J. Berkowitz and W. A. Chupka, *J. Chem. Phys.* **29** (1958) 653.

[40] T. E. Gallon, *Surf. Sci.* **17** (1969) 486.

[41] D. C. Jackson, T. E. Gallon and A. Chambers, *Surf. Sci.* **36** (1973) 381.

[42] M. P. Seah, *Surf. Sci.* **32** (1972) 703.

[43] I. Marklund and S. Andersson, *Surf. Sci.* **5** (1966) 197.

[44] G. E. Laramore and A. C. Switendick, *Phys. Rev. B* **7** (1973) 3615.

[45] H. Tokutaka, M. Prutton, I. G. Higginbotham and T. E. Galloy, *Surf. Sci.* **21** (1970) 233.

[46] E. J. W. Verwey, *Rec. Trav. Chim.* **65** (1946) 521.

[47] G. C. Benson and T. A. Claxton, *J. Chem. Phys.* **8** (1968) 1356.

[48] M. R. Welton-Cook and W. Berndt, *J. Phys C* **15** (1982) 5691.

[49] D. Ferry, J. Suzanne, V. Panella, A. Barbieri, M. A. Van Hove and J.-P. Bibérian, *J. Vac. Sci. Technol. A* **16** (1998) 2261.

[50] D. L. Blanchard, D. L. Lessor, J. P. LaFemina, D. R. Baer, W. K. Ford and T. Guo, *J. Vac. Sci. Technol. A* **9** (1991) 1814.

[51] T. Gotoh, S. Murakami, K. Kinosita and Y. Murata, *J. Phys. Soc. Jap.* **50** (1981) 2063.

[52] M. R. Welton-Cook and M. Prutton, *Surf. Sci.* **74** (1978) 276.

[53] P. S. P. Wei, *Surf. Sci.* **24** (1971) 219.

[54] W. G. Durrer, M. Portillo, P. Wang and D. P. Russell, *App. Surf. Sci.* **81** (1994) 215.

[55] Q. Dou, D. W. Lynch and A. J. Bevolo, *Surf. Sci.* **219** (1989) L623.

[56] H. Tokutaka, M. Prutton, I. G. Higginbotham and T. E. Gallon, *Surf. Sci.* **21** (1970) 233.

[57] R. D. Ramsier and J. T. Yates, Jr., *Surf. Sci. Rep.* **12** (1991) 1.

[58] J. G. Roberts, S. Hoffer, M. A. Van Hove and G. A. Somorjai, *Surf. Sci.* **437** (1999) 75.

[59] S. Fölsch, U. Barjenbruch and M. Henzler, *Thin Solid Films* **172** (1984) 123.

[60] D. F. Ogletree, M. A. Van Hove and G. A. Somorjai, *Surf. Sci.* **173** (1986) 351.

[61] L. B. Pankratz, *Thermodynamic Properties of Halides*, Unites States Department of the Interior, Bureau of Mines, Washington, D.C., 1984.

[62] http://electron.lbl.gov/software/

[63] S. C. Abrahams and J. L. Bernstein, *Acta Cryst.* **18** (1965) 926.

[64] A. Kelly and G. W. Groves, *Crystallography and Crystal Defects*, Addison-Wesley, Reading, MA, 1970.

[65] E. G. McRae and C. W. Caldwell, Jr., *Surf. Sci.* **2** (1964) 509.

[66] N. Garcia, *Phys. Rev. Lett.* **37** (1976) 912.

[67] A. P. Mills, Jr. and W. S. Crane, *Phys. Rev. B* **31** (1985) 3988.

[68] A. F. Ievin'sh, M. Straumanin and K. Karlson, *Zeit. fuer Physik. Chem. Abteil. B: Chem. Der Element. Aufau der Mater.* **40** (1938) 146.

[69] J. J. A. Dusseault and C. C. Hsu, *J. Macromolec. Sci.-Rev. Macromol. Chem. Phys.* **33** (1993) 103.

[70] U. Giannini, G. Giuchi and E. Albizzati, *Recent Advances in Mechanistic and Synthetic Aspects of Polymerization* **215** (1987) 473.

[71] J. G. Roberts; M. Gierer; D. H. Fairbrother; M. A. Van Hove.; G. A. Somorjai; *Surf. Sci.* **399** (1998) 123.

[72] D. H. Fairbrother, J. G. Roberts, S. Rizzi and G. A. Somorjai, *Langmuir* **13** (1997) 2090.

[73] *ESCA Operator's Reference Manual.* ESCA Version 4.0 and Multi-Technique Version 2.0, Perkin-Elmer Corporation, Physical Electronics Division, Eden Prairie, MN 55344, 1998.

[74] J. C. Riviere, *Surface Analytical Techniques* ; Oxford University Press: Oxford, 1990.

[75] E. Magni and G. A. Somorjai, *Appl. Surf. Sci.* **1995**, 89, 187.

[76] A. T. Hubbard, *Surface Imaging and Visualization* ; CRC Press: New York, 1995.

[77] L. Pauling and J. L. Hoard, *Z. Kristallog.* **74** (1930) 546.

[78] A. Ferrari; A. Braibanti; G. Bigliardi, *Acta. Cryst.* **1963**, *16*, 846.

[79] D. H. Fairbrother, J. G. Roberts, G. A. Somorjai, *Surf. Sci.*, **399** (1998) 109.

[80] I. W. Bassi, F. Polato, J. C. Calcaterra; J. C. Bart, *Zeitschr. fur Kristallog.* **1982**, *159*, 297.

[81] B. J. Mrstik, R. Kaplan, T. L. Reinecke, M. A. Van Hove and S. Y. Tong, *Phys. Rev., B* **15** (1977) 897.

[82] M. Kasch, E. Pehlke, W. Schattke, T. Kurberg, H. P. Barnscheidt, R. Manze and M. Skibowski, *Surf. Sci.*, **214** (1989) 436.

[83] W. Erley, *Surf. Sci.* **94** (1980) 281.

[84] X.C. Guo, A. Hopkinson, J. M. Bradley and D. A. King, *Surf. Sci.* **275** (1992) 263.

[85] J. Quinn, Y. S. Li, D. Tian, H. Li, F. Jona and P. M. Marcus, *Phys. Rev. B* **42** (1990) 11348.

[86] M. A. Van Hove and R. J. Koestner, *Detn. Surf. Struc.by LEED* Plenum (1984).

[87] The $Mg^{37/37}Cl_2^+$ isotope (amu 98) is expected to only be ≈11% as intense as the $^{35/35}MgCl_2^+$ isotope (amu 94). Consequently it cannot be resolved above the background noise (see Fig. 7.1).

[88] A. Martorana, A. Marigo, L. Toniolo and R. Zannetti, *Zietsch. fur Kristall.* **176** (1986) 1.

[89] G. Giunchi and G. Allegra, *J. Appl. Cryst.* **17** (1984) 172.

[90] D. E. Partin and M. O'Keeffe, *J. Solid State Chem.* **95** (1991) 176.

Ernest Orlando Lawrence Berkeley National Laboratory
One Cyclotron Road | Berkeley, California 94720

Prepared for the U.S. Department of Energy under Contract No. DE-AC03-76SF00098